Hydrodynamique,
Capillarité &
Changement de Phase

THOMAS SÉON

Sorbonne Université
Institut ∂'Alembert

Mémoire présenté pour l'obtention de
l'Habilitation à Diriger des Recherches

Par

Thomas Séon
Chargé de Recherche

Hydrodynamique, Capillarité & Changement de Phase

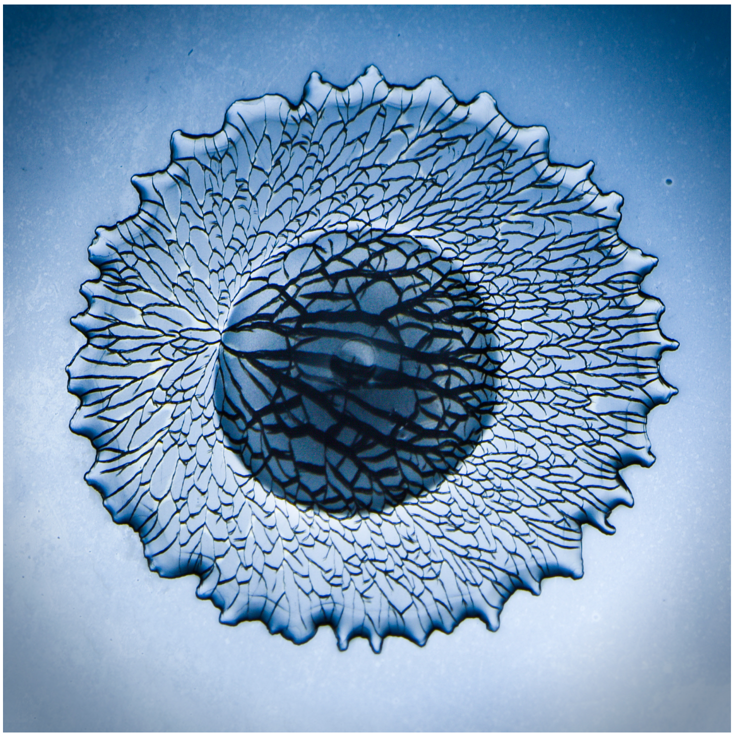

Soutenue le mercredi 5 mai 2021 devant le jury composé de :

Daniel BONN	Rapporteur
Élisabeth CHARLAIX	Examinatrice
Laurent DUCHEMIN	Examinateur
Jean-Pierre HULIN	Examinateur
Pierre-Yves LAGRÉE	Examinateur
Philippe MARMOTTANT	Rapporteur
Olivier POULIQUEN	Rapporteur

Contents

Itinéraire de Recherche 1

Au cours de ma thèse au laboratoire FAST sous la direction de Jean-Pierre Hulin (voir la présentation succincte de mon CV dans la marge), et de mon séjour post-doctoral au département de Mathématique de l'Université de Colombie Britannique (UBC, Vancouver, Canada), je me suis beaucoup intéressé à des problèmes d'écoulement et de mélange induits par gravité entre deux fluides miscibles de densités différentes. Ce type d'écoulement stratifié fait intervenir de nombreux phénomènes tels que des instabilités gravitationnelles, dites de Rayleigh-Taylor, ou de cisaillement, dites de Kelvin-Hemholtz, qui déstabilisent l'interface et mélangent les deux fluides. Ensuite, le post-doctorat que j'ai effectué au département de Physique de l'Université du Chili m'a permis d'ouvrir mon champ de compétence hydrodynamique vers d'autres domaines de la physique non-linéaire, où cette fois la surface libre et la notion de tension de surface sont cruciales. Cette étude s'est focalisée sur les instabilités de Faraday et les solitons non-propagatifs qui peuvent exister dans cette configuration. À mon retour du Canada, j'ai travaillé trois mois à l'IRPHE (Marseille), dans le cadre d'un court séjour doctoral visant à construire, instrumenter et tester une expérience de résonateur de Helmholtz dans une cavité rotor-stator sous pression en gaz SF6. Cette étude s'inscrit au sein d'un projet confidentiel SNECMA de modélisation expérimentale de turbopompe cryogenic.

Curriculum vitæ, les principales étapes :
2003-2006 : Thèse au FAST (Orsay)
2006-2007 : Postdoc à Santiago (Chili)
2008-2009 : Postdoc à Vancouver (Canada)
2010-2012 : Postdoc ∂'Alembert (Paris)
Depuis 2012 : CR à ∂'Alembert (Paris)

Depuis le début de mon post-doctorat à l'Institut Jean Le Rond ∂'Alembert, en octobre 2010, suivi de mon recrutement au CNRS en octobre 2012, mes activités de recherche se sont principalement orientées vers des problèmes de dynamique des fluides multiphasiques non miscibles, mettant en jeu tour à tour surface libre, bulle, jet et goutte. J'ai notamment travaillé sur la dynamique de jets générés lors de la relaxation de bulles centimétriques ou de cavités creusées à la surface d'un liquide. Je me suis aussi beaucoup intéressé à l'éclatement de bulles millimétriques à la surface de l'eau, de l'effondrement capillaire de la cavité jusqu'au détachement des gouttes de jet. Depuis quelques années, j'ai développé de nouvelles activités autour du couplage entre hydrodynamique et changement de phase. J'ai ainsi travaillé sur l'évaporation de ces gouttes de jet et sur la solidification d'une goutte d'eau ou d'un rivulet s'écoulant sur un substrat très froid ([-100°C, 0°C]). Ces systèmes sont abordés à l'aide d'expériences modèles, appuyées lorsque c'est possible de théories simples et de lois d'échelle ayant pour objectif de faire émerger l'essence des mécanismes physiques en jeu. Enfin, les thèmes que j'aborde sont au centre des activités du groupe Fluides Complexes et Instabilités Hydrodynamiques (FCIH) de l'Institut ∂'Alembert dont l'intérêt pour les problèmes où s'entremêlent hydrodynamique et interface se manifeste depuis sa création.

Dans ce premier chapitre, je reprends succinctement cet itinéraire. Je commence par une présentation rapide du travail que j'ai effectué en thèse et pendant mon post-doctorat au Canada autour des courants de gravité, puis je décrirai les activités de recherche majeures que j'ai développées à l'Institut ∂'Alembert, en en présentant les résultats les plus importants. Je poursuivrai avec une discussion autour des perpectives de recherche. Je finirai ce chapitre général en évoquant les grandes lignes d'un ouvrage sur les lois d'échelle, fruit de trois ans de travail, qui a été publié en octobre 2018 aux éditions Odile Jacob. Les deux chapitres suivants détailleront les deux principaux sujets que j'ai traités depuis mon recrutement : la physique de l'effervescence (Chapter 2) et la solidification d'impact de goutte (Chapter 3).

1.1 Courants de gravité

Présentation du problème

Nous nous sommes intéressés dans ce travail au mélange spontané sous l'effet de la gravité de deux fluides de densités différentes, initialement séparés sous forme de deux couches superposées, mises dans une configuration instable de contraste de densité, dans une géométrie confinée telle qu'un tube vertical ou incliné (Figure 1.1). Ce type de problème se rencontre fréquemment en océanographie, en hydrologie ou encore en génie pétrolier ou chimique.

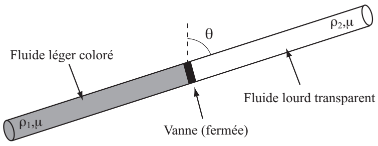

Figure 1.1: Dispositif expérimental. La vanne est ouverte au début de l'expérience (t=0). ρ_1 et ρ_2 sont les densités respectives des deux fluides et μ leur viscosité commune. θ est l'angle que fait le tube avec la verticale.

Résultats

Les études expérimentales abordées dans ce travail ont porté sur deux phénomènes physiques macroscopiques étroitement reliés :

- La dynamique du front de déplacement.
- Le mélange en aval du front, et tout particulièrement l'évolution du profil de concentration moyenne.

Dynamique de front Notre étude expérimentale de la vitesse du front d'interpénétration des fluides V_f, en fonction de l'angle d'inclinaison θ par rapport à la verticale, a fait apparaître trois régimes : lorsque le tube est proche de l'horizontale (Figure 1.2, $\theta = 85°$), on observe un contre écoulement quasi-parallèle sans mélange entre les fluides. La composante de la gravité transverse à l'axe du tube impose en effet une stratification suffisamment forte pour bloquer le développement des instabilités de cisaillement à l'interface qui induiraient un mélange transverse des fluides. La valeur de V_f peut être évaluée par les mêmes lois que celles qui régissent les écoulements de Poiseuille. Le "moteur" de l'écoulement dans cette configuration est, en effet, la composante longitudinale $g\cos\theta$ de la gravité.

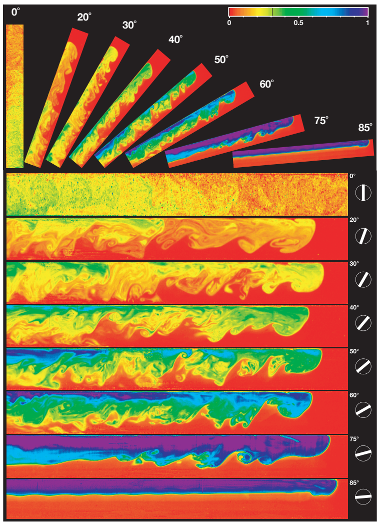

Figure 1.2: Images de la fraction locale de fluide léger montant dans le fluide lourd obtenues à différents angles d'inclinaison et pour les mêmes valeurs des paramètres de contrôle que pour le graphe (a) (champ des images : 20 × 300 mm). Le code de couleurs pour la fraction normalisée est montré en haut à droite de la figure. Les images du dessus montrent l'inclinaison réelle du tube.

Pour des angles θ intermédiaires (Figure 1.2, $\theta = 60 - 75°$), le mélange reste modéré mais l'écoulement est dominé par les effets inertiels. La vitesse du front V_f reflète un équilibre entre la pression de Bernoulli et la pression hydrostatique près de celui-ci. Dans ce régime inertiel, V_f ne varie pas avec θ, elle s'exprime simplement : $V_f \sim \sqrt{\frac{\Delta\rho}{2\rho} g d}$ avec $\Delta\rho$ le contraste de densité entre les fluides et d le diamètre du tube. C'est la vitesse que satisfait la majorité des courants de gravité, avec un nombre de Froude constant. Dans ce second régime, le mélange produit par les instabilités de Kelvin-Helmholtz est encore faible car amorti par l'effet de ségrégation de la gravité transverse [1–3].

Enfin, pour un tube plus proche de la verticale (Figure 1.2, $\theta \leq 50°$), nous observons un régime inertiel différent pour lequel V_f augmente avec θ. L'effet de stratification associé à la composante transverse de la gravité est ici beaucoup moins fort et les instabilités interfaciales mélangent les deux fluides sur toute

[1] Séon et al. (2005), *Physics of fluids*, "Buoyancy driven miscible front dynamics in tilted tubes".
[2] Seon et al. (2007), *Physics of Fluids*, "Front dynamics and macroscopic diffusion in buoyant mixing in a tilted tube".
[3] Séon et al. (2007), *Physics of Fluids*, "Transient buoyancy-driven front dynamics in nearly horizontal tubes".

la section du tube. Des mesures directes de la concentration locale par une technique de fluorescence induite par laser (LIF) ont montré que dans ces régimes inertiels la vitesse V_f est déterminée par le contraste de densité local $\delta\rho$ au niveau du front et non par la différence $\Delta\rho$ entre les densités des fluides de départ ($V_f \propto (\delta\rho)^{0.5}$) [4, 5]. Avec l'augmentation de l'angle d'inclinaison θ, la ségrégation est plus forte et le mélange moins efficace : $\delta\rho$ et la vitesse V_f du front vont donc augmenter. Nous pouvons observer les résultats de ces mesures sur la Figure 1.2 et notamment nous retrouvons que le contraste de densité au front $\delta\rho$ augmente jusqu'à environ 60° pour ensuite rester constant et égal à sa valeur maximum : $\Delta\rho$, la différence entre les densités des fluides de départ. L'intensité du mélange transverse dans la section du tube a donc un rôle clé sur la dynamique du front.

[4] Séon et al. (2006), *Physics of Fluids*, "From turbulent mixing to gravity currents in tilted tubes".
[5] Seon et al. (2006), *Physics of Fluids*, "Laser-induced fluorescence measurements of buoyancy driven mixing in tilted tubes".

Mélange en aval du front : diffusion macroscopique Ce mélange transverse influence également fortement le profil de concentration moyennne relative des deux fluides le long du tube. Dans les tubes verticaux et faiblement inclinés, la variation de cette concentration vérifie une équation de diffusion macroscopique. Les variations du coefficient de diffusion correspondant ont été analysées en fonction des paramètres de contrôle de l'écoulement [2, 6].

[6] Seon et al. (2004), *Physics of fluids*, "Buoyant mixing of miscible fluids in tilted tubes".
[2] Seon et al. (2007), *Physics of Fluids*, "Front dynamics and macroscopic diffusion in buoyant mixing in a tilted tube".

Influence d'un écoulement moyen

Nous nous sommes ensuite intéressés à l'influence d'un écoulement moyen sur l'écoulement induit par gravité que nous venons de décrire. Ici nous nous restreignons aux configurations proches de l'horizontale. Le dispositif expérimental est donc comparable à celui décrit plus haut (Figure 1.1), la principale différence résidant dans la possibilité d'avoir un gradient de pression longitudinal dans le tube, créant un écoulement moyen vers le bas. Ceci est réalisé en reliant le haut du tube à un réservoir placé en hauteur pour l'alimenter par gravité en fluide lourd, et le bas du tube à l'évacuation. Ce travail a conjugué étude expérimentale et analytique [7–10].

Par une étude de l'évolution de la vitesse de front V_f du fluide lourd descendant, poussé par l'écoulement moyen, nous avons notamment pu mettre en évidence une transition d'un écoulement inertiel à un écoulement laminaire lorsque la vitesse de l'écoulement moyen V_0 augmente [8]. Cette stabilisation de l'écoulement est *a priori* contre-intuitive, car en augmentant le gradient de pression, plus d'énergie est injectée dans le système et la vitesse V_f est plus forte. Cependant, l'écoulement moyen est un écoulement de Poiseuille, intrinsèquement parallèle et stable pour les nombres de Reynolds que nous considérons. Il a donc tendance à "paralléliser" les lignes de courants de l'écoulement instable induit par gravité et donc, par approximation de lubrification, à le stabiliser.

[7] Taghavi et al. (2009), *Journal of fluid mechanics*, "Buoyancy-dominated displacement flows in near-horizontal channels: the viscous limit".
[8] Taghavi et al. (2010), *Physics of Fluids*, "Influence of an imposed flow on the stability of a gravity current in a near horizontal duct".
[9] Taghavi et al. (2011), *Physics of Fluids*, "Stationary residual layers in buoyant Newtonian displacement flows".
[10] Taghavi et al. (2012), *Journal of fluid mechanics*, "Miscible displacement flows in near-horizontal ducts at low Atwood number".

Nous avons aussi caractérisé en détail la transition entre un régime de contre écoulement et un régime de déplacement où tout le fluide léger serait emporté avec l'écoulement [9]. Dans ce régime particulier de transition, le courant de gravité de fluide léger monte, parcourt une distance dépendant des paramètres de contrôle, puis s'arrête ! Un équilibre parfait entre les forces de gravité et les forces du gradient de pression est alors atteint, et la couche de fluide léger reste donc globalement immobile. Nous avons montré que, malgré le caractère globalement stationnaire de la couche de fluide, l'interface a une vitesse positive et qu'il existe un mouvement de recirculation à l'intérieur de cette couche. Notons que cette situation est en pratique désastreuse pour les industriels qui souhaitent déplacer un fluide léger avec un fluide lourd, comme c'est le cas lors du forage d'un puits de pétrole par exemple.

1.2 Projections liquides

Les premiers travaux que j'ai développés en arrivant à l'Institut ∂'Alembert furent autour des projections liquides générées par la relaxation de bulles centimétriques (voir Figure 1.3) [11, 12]. Cette étude initia tout un pan de la recherche que je mène encore aujourd'hui. C'est cette trajectoire que je décris dans cette section.

[11] Séon et al. (2011), *Phys. Fluids*, "Jets in viscous bubbles".
[12] Séon et al. (2012), *Phys. Rev. Lett.* "Large bubble rupture sparks fast liquid jet".

Relaxation de cavité et jet

Lorsqu'une bulle d'air suffisamment grande (plusieurs centimètres) et suffisamment étirée verticalement, se détache de son injecteur, ou d'une autre bulle, un jet particulièrement violent peut apparaître en son sein (Figure 1.3). Celui-ci part du bas de la bulle et rattrape son sommet en quelques milli-secondes. Sous certaines conditions ce jet peut ensuite transpercer le haut de la bulle, la surface libre et créer de fortes projections liquides en surface. Ces bulles particulières et les jets qui résultent de leur retour à l'équilibre apparaissent dans un grand nombre d'applications géophysiques ou industrielles, incluant par exemple l'industrie métallurgique ou verrière.


Figure 1.3: Séquence d'images montrant le développement d'un jet dans une bulle étirée alors qu'elle tente de retourner à un état d'équilibre. L'intervalle de temps entre les images est de 6 ms, la hauteur de la bulle juste après détachement est de 4.2 cm et la vitesse de jet 2.69 m.s^{-1}.

Apres avoir travaillé sur la relaxation de ces bulles, nous avons démontré que nous pouvions générer des jets comparables grâce à une expérience modèle, où une surface libre est déformée par un jet d'air impulsif (Figure 1.4). Tous ces jets résultant de l'effondrement d'une cavité présentent des caractéristiques robustes sur une large gamme de paramètres [12]. Cette expérience analogue permet de créer des jets plus propres et plus simples à étudier, elle nous a ainsi permis d'aller beaucoup plus loin dans la caractérisation expérimentale et dans l'étude théorique de ces jets. En effet, en menant une campagne d'expériences utilisant des fluides de différentes viscosités, tensions de surface et densités, nous avons pu montrer que la forme de ces jets présente un caractère auto-similaire et que la vitesse de la tête du jet (V_{jet}) dépend uniquement des paramètres du liquide et de la géométrie de la cavité initiale, et est indépendant des détails du processus d'effondrement [13]. La relation que nous avons déterminée s'exprime dimensionnellement de la manière suivante :

[13] Ghabache et al. (2014), *J. Fluid Mech.* "Liquid jet eruption from hollow relaxation".

$$V_{\text{jet}} = \alpha\sqrt{gH}\frac{H}{L} - \beta\frac{\nu}{L}$$

avec H et L respectivement la hauteur et la largeur de la cavité, g la gravité, ν la viscosité cinématique du liquide et α et β deux constantes déterminées expérimentalement. Cette relation est donc composée de deux termes. Le premier traduit la focalisation du liquide qui s'engouffre dans le jet, et est issu de l'équilibre entre énergie potentielle de gravité disponible et inertie du jet. Le second terme traduit la perte d'énergie par dissipation visqueuse lors de la création de la tête du jet. Le premier terme révèle une dépendance de la vitesse de jet avec la profondeur H et le diamètre maximum L de la cavité initiale, et la vitesse varie avec la profondeur de la cavité H à la puissance 3/2. Nous avons ensuite mis en évidence, grâce à un modèle simple, que cette dépendance en $H^{3/2}$, résultant d'un mécanisme de focalisation des lignes de courant, est inscrite dans la forme de jet mesurée expérimentalement : $r_{\text{jet}}(z,t) \propto \sqrt{t}/z$ avec r_{jet} le rayon du jet à l'altitude z et au temps t.

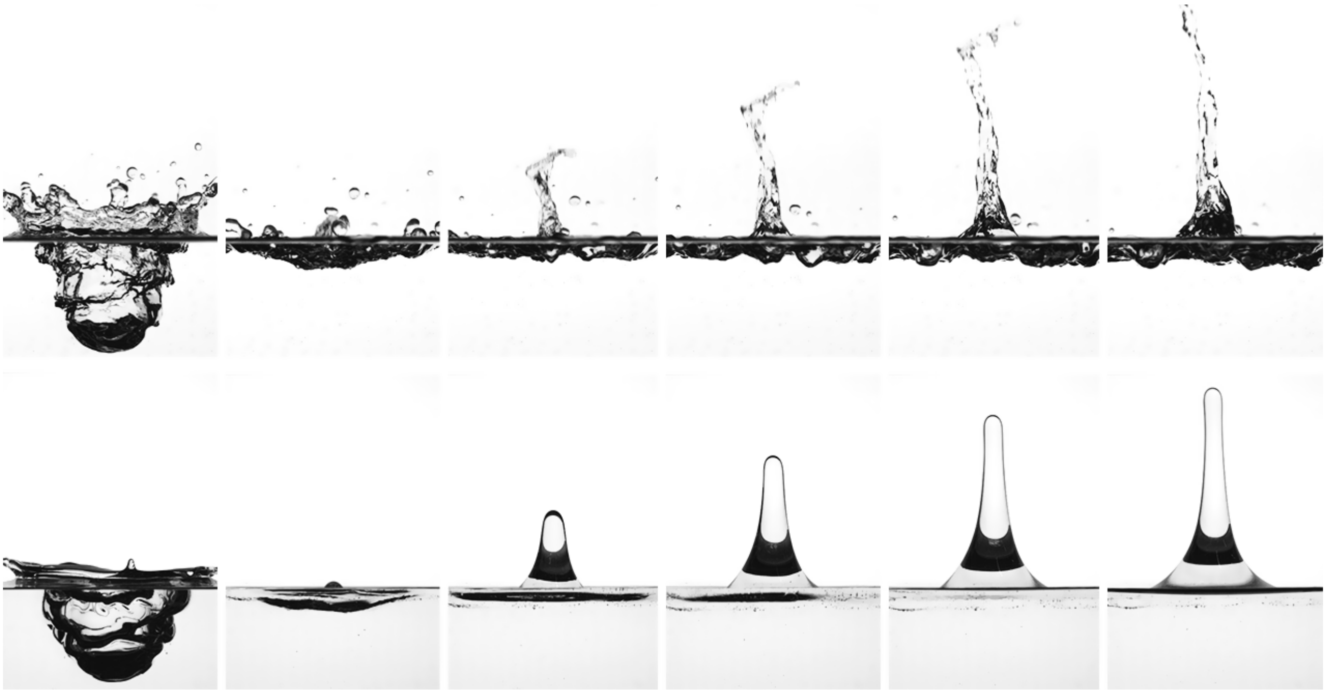

Figure 1.4: Séquences d'images de la relaxation de cavités centimétriques à une surface libre pour deux fluides différents : l'eau en haut (viscosité $\mu = 1$ m.Pa.s) et un mélange eau-glycérol de viscosité $\mu = 833$ m.Pa.s en bas. Chaque séquence commence avec une image de la cavité à sa profondeur maximale H sur le point de relaxer. À partir de l'image suivante, le jet est créé et se développe. Pour la séquence du haut, le temps entre les deux premières images est $\Delta t_{1-2} = 36$ ms et il y a ensuite $\Delta t = 7.5$ ms entre chaque image. La profondeur maximale de la cavité est $H = 4.6$ cm, sa largeur est $L = 6.3$ cm et la vitesse du jet est $v_{\text{jet}} = 3.59$ m.s^{-1}. Pour la séquence du bas dans le liquide visqueux : $\Delta t_{1-2} = 60$ ms, $\Delta t = 27.5$ ms, $H = 6$ cm, $L = 10$ cm et $v_{\text{jet}} = 1.85$ m.s^{-1}.

Apres ce travail sur la physique des jets produits par relaxation gravitaire, la question de leur pendant capillaire semblait encore non résolue, et c'est ainsi que je me suis intéressé au jet produit par relaxation d'une cavité capillaire : une bulle.

Éclatement de bulles et production de gouttes

Contexte

Lorsqu'une vague déferle à la surface de l'océan, elle piège un paquet d'air qui se disloque à cause des mouvements turbulents sous la surface et remonte sous forme d'une multitude de bulles de tailles différentes (Figure 1.5). Une fois à la surface, le film qui sépare chaque bulle de l'atmosphère draine, se rompt puis se désintègre en une myriade de gouttelettes appelée *gouttes de film.* Ce processus laisse alors une cavité ouverte à la surface de l'océan qui, en se comblant, va donner naissance à un jet de liquide montant verticalement, similaire à celui qui fait suite à l'impact d'une goutte dans un liquide. Ce jet finit par se briser et projette ainsi d'autres gouttelettes, appelées cette fois *gouttes de jet.* Les 10^{18} à 10^{20} bulles qui éclatent chaque seconde à la surface des océans génèrent de cette manière la majeure partie des embruns, ou aérosols marins, présents au-dessus des mers et des océans. Ces gouttelettes transportent des gaz dissous, des sels minéraux, des surfactants et d'autres matières biologiques dans l'atmosphère. En s'évaporant, ces gouttelettes participent également fortement aux transferts de masse et de chaleur entre l'océan et les couches basses de l'atmosphère, jouant ainsi un rôle déterminant dans les couplages globaux entre l'océan et l'atmosphère et la régulation climatique qui en résulte.

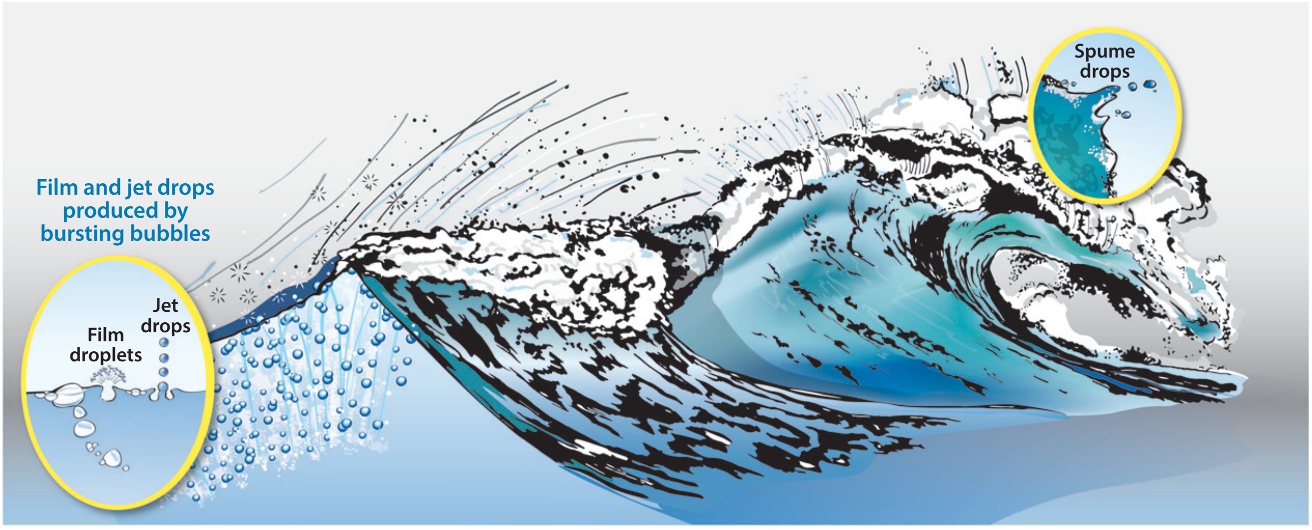

Figure 1.5: Production d'aérosols à la surface de l'océan : par l'éclatement de petites bulles (gouttes de film et gouttes de jet) et par la fragmentation du liquide à la crête des vagues (gouttes d'écume). Illustration : Véron (2015) [14]

Le même phénomène de production d'aérosols par éclatement de bulles se produit à la surface d'un verre de champagne. Les gouttes ainsi formées s'évaporent, comme au-dessus de l'océan, et dans ce cas vont jouer un rôle important dans la diffusion des arômes. La quantification et le contrôle de ce phénomène représentent un atout important pour les producteurs champenois. Nous en reparlerons plus loin dans de ce manuscrit.

[14] Veron (2015), *Annual Review of Fluid Mechanics*, "Ocean Spray".

Notre objectif est de quantifier ce processus dans son ensemble. Nous souhaitons être capables de prédire la quantité d'eau évaporée pour une distribution de taille de bulles données[1] . Pour ce faire, il y a une succession de processus à modéliser : le mûrissement des bulles en surface qui va modifier leur distribution, le déchirement du film et la production de gouttes de film, la génération du jet et sa déstabilisation en gouttes de jet et finalement l'évaporation de toutes ces gouttes produites. Jusqu'à maintenant, nous nous sommes focalisés sur le processus de relaxation des bulles une fois débarrassé de leur film, sur la génération du jet, des gouttes de jets produites, et sur leur évaporation. C'est donc nos contributions sur la compréhension de ces phénomènes que je vais décrire dans ce manuscrit. Je présente ici succinctement les principaux résultats de cette étude, qui fera l'objet d'une description plus détaillée au chapitre suivant (Chapter 2).

[1] Cette distribution commence à être connue lorsqu'elle est générée par le déferlement d'une vague [15, 16].

[15] Deane et al. (2002), *Nature*, "Scale dependence of bubble creation mechanisms in breaking waves".
[16] Deike et al. (2016), *Journal of Fluid Mechanics*, "Air entrainment and bubble statistics in breaking waves".

Relaxation de bulle et dynamique de jet

Nous avons commencé cette étude en nous intéressant aux ingrédients physiques à l'origine du jet capillaire issu de l'éclatement d'une petite bulle à la surface libre d'un liquide. En étudiant l'éclatement de la bulle dans des liquides de différentes viscosités, tensions de surface et densités, nous avons pu identifier une loi d'échelle pour la vitesse du jet et démêler le rôle des différents ingrédients pertinents que sont : la forme de la bulle, les ondes capillaires émises durant l'effondrement de la bulle, la gravité et les propriétés du liquide [17]. Nous avons notamment mis en évidence un comportement surprenant où l'augmentation de la viscosité produit des jets plus rapides et des gouttes plus petites. Cet effet de la viscosité s'observe parfaitement sur la Figure 1.6 : les gouttes produites lors de l'éclatement d'une bulle à la surface de l'eau (a) sont

Notons que deux doctorants ont travaillé sur ce sujet :
2012-2015 : E. Ghabache (thèse expérimentale)
2017-2020 : A. Berny (thèse numérique)

[17] Ghabache et al. (2014), *Physics of Fluids*, "On the physics of fizziness: How bubble bursting controls droplets ejection".

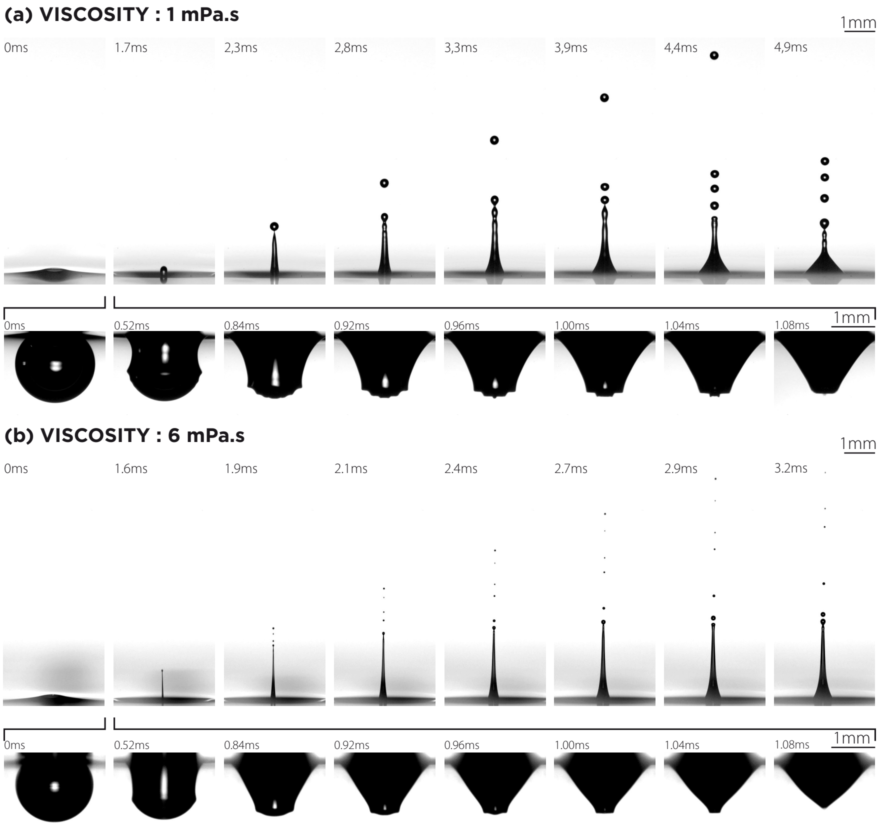

Figure 1.6: Séquences d'images de deux jets typiques faisant suite à l'éclatement d'une bulle à la surface de (a) l'eau et (b) d'un mélange eau-glycérol six fois plus visqueux que l'eau. Dans chaque cas, la séquence du haut montre l'événement d'éclatement de bulle au-dessus de la surface libre de l'eau, alors que la séquence du bas présente l'effondrement de la cavité donnant naissance au jet, grâce à une vue de sous la surface libre. La séquence du bas à lieu entre les deux premières images de la séquence du haut. Les temps sont montrés sur les images avec la même origine. Les rayons de bulles sont : (a) $R_b = 884\ \mu$m (b) $R_b = 915\ \mu$m.

nettement plus grosses que celles produites lors de l'éclatement d'une bulle à la surface d'un liquide six fois plus visqueux (b). Nous avons démontré que les ondes capillaires parcourant la cavité et qui sont à l'origine du jet (séquences du bas des Figure 1.6 (a) & (b)), évoluent toujours pour former finalement une petite cavité s'effondrant au bas de la bulle en suivant un comportement auto-similaire. Cependant, certaines de ces ondes sont également responsables de la destruction de cet effondrement auto-similaire et empêchent donc le système de s'approcher de sa limite singulière. Augmenter la viscosité du liquide a alors pour conséquence d'amortir ces ondes capillaires destructrices, permettant ainsi à l'effondrement auto-similaire de se rapprocher de sa limite singulière et donc de produire des jets plus rapides et plus fins.

Plus récemment, cette étude expérimentale a été complétée numériquement [18] en explorant des zones de l'espace des phases inaccessibles expérimentalement. Les simulations numériques sont réalisées en résolvant les équations de Navier-Stokes incompressibles, à deux phases et axi-symétriques, avec tension de surface, en utilisant le logiciel libre *Gerris*. Cette étude est réalisée en collaboration avec S. Popinet de l'Institut ∂'Alembert et L. Deike de l'Université de Princeton aux États-Unis. La Figure 1.7 présente deux simulations typiques: (a) présente une dynamique proche de ce qu'il se passe dans l'eau (Figure 1.6 (a)) et (b) dans un liquide plus visqueux (Figure 1.6 (b))). Apres avoir réalisé une validation complète de la méthode numérique en comparant ces résultats aux données expérimentales, l'extension aux paramètres de contrôle inaccessibles expérimentalement nous a permis de proposer une loi universelle pour la dépendance de la vitesse de la première goutte produite lors de l'éclatement d'une bulle, en fonction de tous les paramètres de contrôle, et valable sur toute la gamme de ces paramètres.

[18] Deike et al. (2018), *Physical Review Fluids*, "Dynamics of jets produced by bursting bubbles".

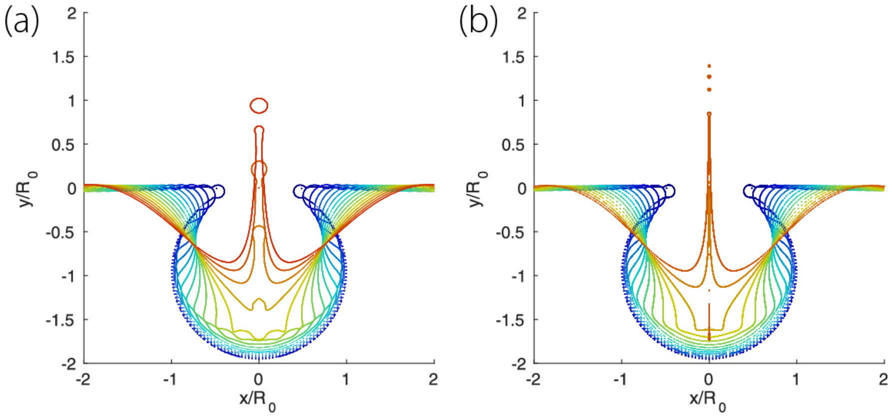

Figure 1.7: Évolution en temps du profil de la cavité, montrant l'effondrement de la cavité et la formation du jet pour trois viscosités (μ) et la même taille de bulle (R = 270 μm). (a) $\mu = 1.4$ mPa.s : de nombreuses ondes capillaires se propagent vers le bas de la cavité, créant un jet qui va se rompre en plusieurs gouttes. (b) $\mu = 4.4$ mPa.s, l'effondrement s'effectue via la propagation d'une seule onde capillaire qui se focalise au bas de la cavité, donnant naissance à un jet rapide et fin, qui forme des gouttes bien plus petites que dans le cas précédent.

Détachement des gouttes de jet

Après cette étude sur la dynamique des jets et de la premiere goutte, nous avons souhaité caractériser la taille des gouttes éjectées lors de l'éclatement des bulles. Par souci de simplicité, nous nous sommes ici aussi concentrés sur la taille de la première goutte éjectée. Nous avons tout d'abord établi une premiere loi d'échelle permettant la détermination du rayon de la première goutte en fonction du rayon de la bulle mère et des propriétés du liquide (viscosité, tension de surface et densité) [19]. Puis, dans le but de découpler les effets de l'effondrement de la cavité et de la dynamique du jet dans le détachement de la goutte, nous avons proposé une seconde loi d'échelle permettant d'avoir la taille de la goutte en fonction uniquement de paramètres issus de la dynamique du jet : vitesse de jet et paramètre du liquide. En particulier, la taille de la bulle n'intervient plus. Ceci nous permet de démêler les rôles complexes de la viscosité, de la gravité et de la tension de surface dans la sélection de la taille de goutte. Nous montrons ainsi que le détachement est non-visqueux et qu'il est issu de la compétition entre l'inertie initiale donnée au jet et le duo capillarité-gravité qui tire sur la tête du jet.

[19] Ghabache et al. (2016), *Phys. Rev. Fluids*, "Size of the top jet drop produced by bubble bursting".

À ce stade nous avions de quoi prédire la taille et la vitesse des premières gouttes éjectées, mais il manquait la caractérisation des gouttes suivantes. Pour ce faire, nous avons repris le code numérique introduit précédemment et nous l'avons adapté au logiciel libre *Basilisk*[2] . Puis nous avons validé ses résultats, notamment grâce aux nouveaux résultats expérimentaux sur la taille de la premiere goutte. Enfin, nous avons fait une étude systématique où nous mesurons la taille et la vitesse de toutes les gouttes éjectées, quels que soient les paramètres de contrôle (taille de la bulle et paramètres du liquide) [20]. Grâce à cette immense base de données, nous pouvons maintenant prédire la distribution de tailles de gouttes peuplant un aérosol généré par éclatement de bulle, simplement en connaissant la distribution de tailles de bulles et les propriétés du liquide. C'est un résultat crucial, d'autant plus que, comme nous le disions en introduction, les distributions de tailles de bulles sont de mieux en mieux connues dans l'océan [15, 16] et qu'elles sont aujourd'hui contrôlables dans un verre de champagne [21].

2. Comme *Gerris*, son prédécesseur, *Basilisk* est développé par S. Popinet avec qui nous collaborons sur ce sujet numérique.

[20] Berny et al. (2020), *Physical Review Fluids*, "Role of all jet drops in mass transfer from bursting bubbles".

[21] Liger-Belair (2014), *The Journal of Physical Chemistry B*, "How many bubbles in your glass of bubbly?".

Évaporation des gouttes

Pour finir, nous avons écrit un modèle d'évaporation basé sur deux équations différentielles couplées : une qui donne la trajectoire de la goutte (principe fondamental de la dynamique) et l'autre qui donne la réduction du rayon de la goutte par évaporation (tirée de la loi de Fick). Ce modèle prend comme conditions initiales la taille et la vitesse de la goutte au moment de l'éjection. Après avoir validé ce modèle en comparant ses résultats aux trajectoires expérimentales [22], nous l'avons appliqué sur l'ensemble des gouttes pour connaître la quantité de masse évaporée de chacune des gouttes éjectées par éclatement de bulle, quelques soient la taille de la bulle et les paramètres du liquide [20]. Ainsi, nous avons démontré que toutes les gouttes produites lors d'un événement d'éclatement de bulle, et il peut y en avoir jusqu'à une vingtaine, jouent un role dans la quantité totale de masse d'eau évaporée. Enfin, sur la base de ces résultats, nous proposons une loi d'échelle prédisant la masse totale évaporée lors de l'éclatement d'une bulle en fonction de la taille de la bulle et des paramètres du liquide. Cette relation représente un pas important vers l'obtention d'un modèle physique des échanges d'eau entre l'océan et l'atmosphère.

[22] Ghabache et al. (2016), *Scientific Reports*, "Evaporation of droplets in a Champagne wine aerosol".

[20] Berny et al. (2020), *Physical Review Fluids*, "Role of all jet drops in mass transfer from bursting bubbles".

Application au champagne

En parallèle de ces études fondamentales sur la production et l'évaporation des gouttes de jet, je m'intéresse à l'éclatement des bulles à la surface du champagne, depuis plusieurs années maintenant, en collaboration avec Gérard Liger-Belair de l'Université de Reims. Dans le cadre de cette collaboration, nous avons commencé par rassembler les résultats connus autour des mécanismes physiques de l'effervescence, puis nous nous sommes intéressés à la forme du verre sur la taille des bulles [23, 24]. D'autre part, comme nous l'avons déjà évoqué, le spray formé par l'éclatement de toutes les bulles à la surface d'un verre de champagne participe à la diffusion des arômes de champagne. Grâce à des expériences modèles d'éclatement de bulle dans des solutions de champagne idéalisées (solutions hydro-alcooliques), la vitesse, le rayon et la hauteur maximum de la première goutte ont été caractérisés en fonction de la taille de la bulle mère et des propriétés du liquide (viscosité, tension de surface et densité) dans la gamme des vins de Champagne [22]. Ces expériences nous ont ainsi permis de montrer que les aérosols de champagne ne contenaient pas de gouttes de film, à la différence des aérosols marins, et que les solutions hydro-alcooliques rendaient parfaitement compte de la production d'aerosols dans le champagne. Ce dernier résultat suggérant que le rôle des surfactants présents dans le champagne est négligeable dans la production de gouttes. Enfin, en utilisant ces résultats expérimentaux et notre modèle d'évaporation, nous avons montré que les aérosols présents au-dessus d'un verre de champagne améliorent effectivement grandement, d'au moins un facteur 10, le transfert de liquide dans l'air par rapport à une surface de liquide plane. De plus, nous avons mis en évidence les rayons de bulle et les propriétés du champagne permettant d'optimiser l'évaporation de ces aérosols. Ces résultats ouvrent une voie évidente vers une optimisation de la diffusion des arômes de champagne et intéressent donc particulièrement les acteurs de cette industrie. Tous les résultats expérimentaux autour des éclatements de bulles ont été rassemblés, et re-contextualisés autour des applications au champagne, dans un article de revue paru en 2017 [25].

[23] Liger-Belair et al. (2012), *Bubble Science, Engineering & Technology*, "Collection of collapsing bubble driven phenomena found in champagne glasses".

[24] Liger-Belair et al. (2013), *Revue des œnologues et des techniques vitivinicoles et œnologicques : magazine trimestriel d'information professionnelle*, "La dégustation du champagne : Quelques éléments de réflexion sur l'impact de la forme du verre et de la taille des bulles".

[25] Séon et al. (2017), *The European Physical Journal Special Topics*, "Effervescence in champagne and sparkling wines: From bubble bursting to droplet evaporation".

Splash et impact de goutte

Dans la suite des travaux autour des projections liquides il n'est plus question de bulles mais toujours de jets, de gouttes et d'éclaboussures. En effet, lorsqu'une goutte impacte une surface, elle éclabousse. Lorsque cette surface est un solide, ces éclaboussures sont souvent appelées *splash*. Leur structure, leur dynamique et les mécanismes physiques qui en sont responsables sont encore sujet à débat et génèrent de nombreux travaux dans notre communauté [26]. Lorsque cette surface est un liquide, il existe deux types de projection liquide qui sont illustrées sur la séquence du haut de la Figure 1.8 : tout d'abord une éclaboussure en forme de corolle, qui se compare au splash sur solide tout en ayant des caractéristiques bien différentes, notamment parcequ'elle contient du liquide de la surface impactée ; puis, dans un deuxième temps, un jet vertical est généré par la relaxation de la cavité ainsi formée. Dans le cadre d'une étude en collaboration avec C. Josserand (LadHyX) et G.-J. Michon (∂'Alembert), nous avons tenté d'apporter un peu de lumière sur ces différentes sortes de projection liquide. Nous avons commencé par nous intéresser à la dynamique du jet lors de l'impact d'une goutte sur un liquide [27], puis nous avons étudié la structure de la corolle, sur liquide comme sur solide [28]. C'est ce travail que nous décrivons dans les deux paragraphes qui suivent.

[26] Josserand et al. (2016), *Annual Review of Fluid Mechanics*, "Drop impact on a solid surface".

[27] Michon et al. (2017), *Physical Review Fluids*, "Jet dynamics post drop impact on a deep pool".

[28] Marcotte et al. (2019), *Physical review letters*, "Ejecta, corolla, and splashes from drop impacts on viscous fluids".

Impact de goutte sur liquide

Comme nous venons de l'introduire, lorsqu'une goutte tombe sur un bain liquide, la surface libre est déformée puis revient à l'équilibre (Figure 1.8). Cette relaxation s'accompagne le plus souvent de l'émergence d'un jet, similaire à ceux présentés dans les sections précédentes. Nous avons ici mené une large campagne d'expériences visant à étudier l'évolution de la forme et de la vitesse de ce jet en fonction des paramètres de contrôle que sont la vitesse et la taille de la goutte à l'impact et les propriétés du liquide. Nous avons pu rassembler les différents comportements en deux régimes distincts : les *jets de cavité* et les *jets singuliers*, dont deux exemples typiques sont décrits en Figure 1.8. Dans les deux cas, les mécanismes à l'origine de la dynamique des jets sont différents. Dans le premier cas, c'est un effondrement singulier des ondes capillaires qui génère un jet rapide et fin, et dans l'autre, c'est une rétractation capillaire de la cavité qui est à l'origine des jets dont la vitesse est donc proportionnelle à la vitesse capillaire $\sqrt{\gamma/\rho D}$. Nous montrons que ces deux régimes peuvent aussi se décorréler et ainsi apparaître à des instants différents, donnant lieu à deux types de projections liquides issus du même événement de relaxation de cavité [27].

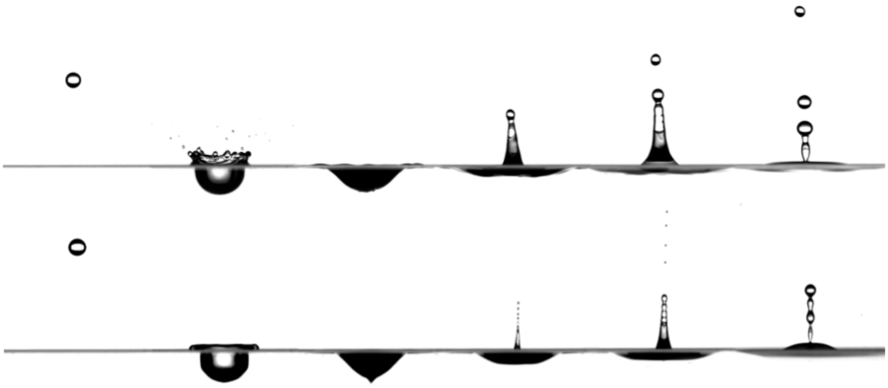

Figure 1.8: Séquences d'images d'impact de goutte sur une surface du même liquide et du jet qui en résulte. Les deux séquences sont réalisées dans l'eau et pour des tailles de goutte légèrement différentes. Nous observons que les jets ainsi générés sont complètement différents ; le premier, large et lent, est qualifié de *jet de cavité* tandis que le deuxième fin et rapide, est qualifié de *jet singulier*.

Impact de goutte, du liquide au solide

Dans un deuxième temps nous avons étudié la structure du splash lors de l'impact d'une goutte. Pour avoir une vision complète de la structure de cette corolle, nous cherchions à proposer une description commune à l'impact sur solide et sur liquide. Pour ce faire, l'expérience consiste à faire impacter une goutte de liquide sur un bain de liquide visqueux (mélange eau-glycérol), dont la viscosité varie de une à mille fois celle de la goutte. Le substrat varie ainsi continûment d'un liquide peu visqueux à un solide. Pour démêler les effets conjoints de l'air et du liquide, nous avons aussi fait varier la pression de l'air, et, pour être capable de mieux discerner la structure fine de l'éjecta, une étude numérique a été réalisée en parallèle avec le logiciel *Gerris*. De cette manière, nous avons montré que l'étalement de la corolle consiste en deux films liquides distincts : un film fin nourri par la goutte, et un second nourri par le substrat liquide. Ces films sont représentés respectivement en noir et en blanc sur la Figure 1.9. Lors de l'impact sur un liquide, ces deux films se rassemblent instantanément pour n'en former qu'un (séquence du haut de la Figure 1.9), puis, lorsque la viscosité du substrat augmente, ils se découplent complètement pour avoir des dynamiques de plus en plus indépendantes (séquences du milieu puis bas de la Figure 1.9). Cette structure en deux films distincts est cruciale pour comprendre la dynamique globale de la corolle [28].

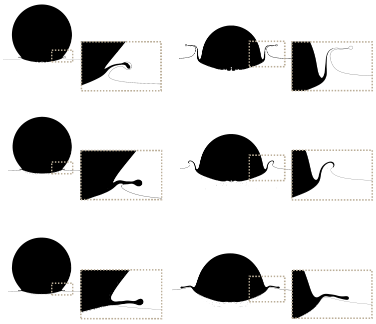

Figure 1.9: Trois séquences numériques réalisées pour un rapport de viscosité entre la goutte et le substrat de 5 (haut), 50 (milieu) et 200 (bas). Dans ces trois cas deux temps après l'impact sont représentés, avec agrandissement de l'interface goutte/substrat dans la zone du splash.

1.3 Solidification d'écoulements capillaires

Contexte

Deux doctorants ont travaillé sur ces sujets :
2016-2019 : V. Thiévenaz
2018-2021 : A. Monier (en cours)

Comment se forme une cascade de glace (Figure 1.10) ? En combien de temps croissent les stalactites de glace qui peuplent les grottes des régions froides ? Les structures de glace qui émergent naturellement dans des environnements froids adoptent bien souvent des formes surprenantes qui interrogent la curiosité scientifique. Au delà de cet aspect morphologique, les formations de glace (congélation de rivières, d'estuaires, aufeis) dans les zones froides de l'hémisphère peuvent être à l'origine de toute une variété de problèmes écologiques et socio-économiques importants [29].

Figure 1.10: Cascade de glace.

[29] Beltaos (2013), , "River ice formation".

Le 1^er juin 2009, l'Airbus A330-200 assurant le vol Air France 447 entre Rio et Paris s'abîme dans l'océan Atlantique, entraînant la mort des 228 personnes à bord. C'est l'accident le plus meurtrier de l'histoire d'Air France. L'accrétion de glace sur les sondes Pitot provoqua la perte momentanée des indications de vitesse, ce qui entraîna le décrochage de l'avion causant le *crash*. Cette catastrophe n'est pas isolée et l'accrétion de glace sur les avions (Figure 1.11), au sol ou en vol, est un problème qui coûte très cher à l'industrie aéronautique, et constitue donc un sujet de recherche prioritaire[3] . Le secteur aéronautique n'est pas le seul à tenter de combattre ce phénomène ; il touche aussi l'industrie éolienne, le secteur des travaux publics, *etc.*

Figure 1.11: Accrétion de glace sur une aile d'avion.

Comprendre les mécanismes de formation de glace revêt donc un intérêt environnemental et industriel majeur et constitue un défi fondamental passionnant pour la communauté scientifique. Pourtant, lorsque ces mécanismes sont couplés à des écoulements capillaires classiques (goutte, ruisselet, film), ils sont encore largement incompris. La présence de surfaces libres et de lignes de contact pose des problèmes particuliers. Ce constant est d'autant plus surprenant que les écoulements capillaires sont très courants, ils jouent notamment un rôle important dans tous les exemples cités précédemment. Interaction entre

---

[3] À ce titre nous avons pu bénéficier de plusieurs contrats avec la DGA.

front de solidification et surface libre, dynamique de mouillage et démouillage de l'eau sur la glace, structure de glace issue du confinement capillaire des couches limites thermiques, dynamique de solidification d'un film de savon sont quelques unes des questions ouvertes. Ces problèmes intrinsèquement multidisciplinaires, où se couplent hydrodynamique capillaire et transfert thermique, sont étudiés à l'aide d'expériences modèles, de lois d'échelle et, lorsque cela est possible, de modèles théoriques couplant les équations de Navier-Stokes et de transport de la chaleur. Ce projet de recherche à été initié il y a cinq ans au laboratoire en collaboration avec C. Josserand (LadHyX). Nous avons commencé par le couplage entre impact de goutte et solidification, puis nous nous sommes intéressés à la solidification de ruisselet. Ces études sont décrites succinctement dans la suite et la solidification de goutte constituera le cœur du troisième chapitre de ce manuscrit (Chapter 3).

Impact de goutte

Solidification d'une goutte d'eau

L'expérience considérée consiste à étudier l'impact d'une goutte sur un substrat très froid. Nous varions les paramètres d'impact (taille et vitesse de goutte) et la température du substrat, qui est comprise entre -100° et 0°C. Le substrat est aussi changé pour modifier les paramètres thermiques du substrat que sont la conductivité thermique (λ), la capacité calorifique (C_p) et la densité (ρ). Lorsque la goutte impacte le substrat froid, elle s'étale, commence à se solidifier, pour finalement adopter une forme surprenante qui dépend des paramètres de contrôle. Les deux principaux motifs sont présentés sur la Figure 1.12. À gauche, la goutte gelée a une forme d'œuf au plat et à droite celle d'un demi-anneau posé sur un disque de glace.

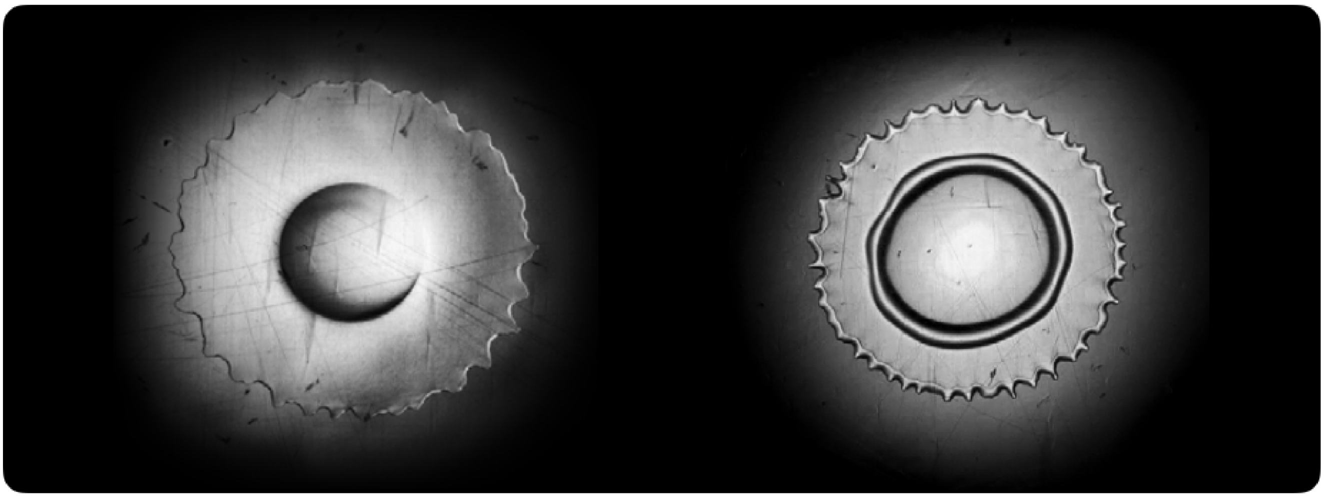

Figure 1.12: Deux formes différentes prises par une goutte d'eau qui s'est trouvée gelée après avoir impacté une surface très froide. À gauche, la goutte gelée prend la forme d'un œuf au plat ; à droite, celle d'un anneau posé sur un disque de glace.

Comprendre la physique sous-jacente à la solidification d'une goutte d'eau impactant un solide froid revient à être capable de comprendre finement ces formes si particulières. Nous avons donc commencé par établir un modèle théorique 1D de propagation de la chaleur, basé sur le problème de Stefan, qui nous permet de prédire la dynamique de propagation du front de solidification [30]. Nous avons ensuite caractérisé précisément la dynamique d'étalement en imagerie rapide et montré comment elle était affectée par le changement de

[30] Thiévenaz et al. (2019), *J. Fluid Mech.* "Solidification dynamics of an impacted drop".

phase [31]. Puis nous avons identifié les mécanismes pertinents de mouillage et démouillage de l'eau sur la glace [32]. Enfin, la mesure fine de la forme des gouttes gelées grâce à un profilomètre optique nous a permis, d'une part, de retrouver précisément le profil exact des gouttes gelées et, d'autre part, de montrer que leur forme résulte de l'interaction entre la propagation verticale du front de solidification, et la rétractation capillaire de la couche d'eau non-gelée sur la couche de glace formée à l'impact, les deux processus ayant des temps caractéristiques comparables [32]. Nous avons de cette manière démontré comment la dynamique d'une goutte qui se solidifie à l'impact est la conséquence de la compétition entre hydrodynamique capillaire et changement de phase.

[31] Thiévenaz et al. (2020), *Subm. to Europhys. Lett.* "Freezing-damped impact of a water drop".

[32] Thiévenaz et al. (2020), *Phys. Rev. Fluids*, "Retraction and freezing of a water film on ice".

Fractures

Nous venons de voir que lorsqu'une goutte impacte un substrat froid, elle s'étale, se fige, puis se solidifie. La goutte solide est alors, à 0°C, attachée au substrat. Si le substrat est plus froid, il va continuer à refroidir la goutte de glace, qui va donc se contracter, et, comme elle est contrainte de rester sur le substrat, elle va emmagasiner de l'énergie élastique qu'elle pourra alors relâcher en se fracturant, comme c'est le cas sur la Figure 1.13.

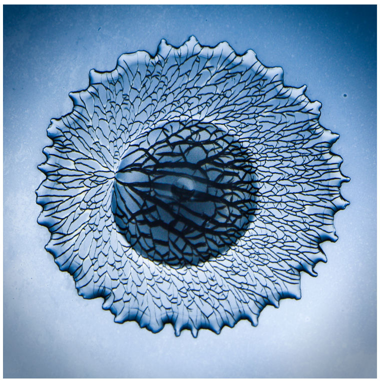

Figure 1.13: Fractures dans une goutte gelée.

Nous avons alors montré que ces fractures apparaissent sur la goutte gelée en dessous d'une certaine température du substrat, et que les motifs de fractures dépendent du choc thermique (Figure 1.14) [33]. À basse température, il n'y a donc pas de fracture, puis, pour des substrats plus froids, on observe ce que nous appelons un régime de *fragmentation 2D*, où toutes les fractures apparaissent sur un temps extrêmement court (quelques micro-secondes), depuis un point de nucléation qui varie d'une expérience à l'autre. Pour des substrats encore plus froids, les fractures apparaissent l'une après l'autre, hiérarchiquement, se raccordant les unes aux autres en formant des angles proches de 90°. Ce régime, mieux connu, est traditionnellement appelé régime de *fractures hiérarchiques*. Grâce à des arguments d'échelles, nous avons pu estimer assez précisément les températures de transition entre les régimes et le temps d'apparition des premières fractures. Enfin, nous avons réalisé un espace des phases montrant comment ces régimes peuvent être contrôlés par les paramètres d'impact.

[33] Ghabache et al. (2016), *Physical Review Letters*, "Frozen impacted drop: From fragmentation to hierarchical crack patterns".

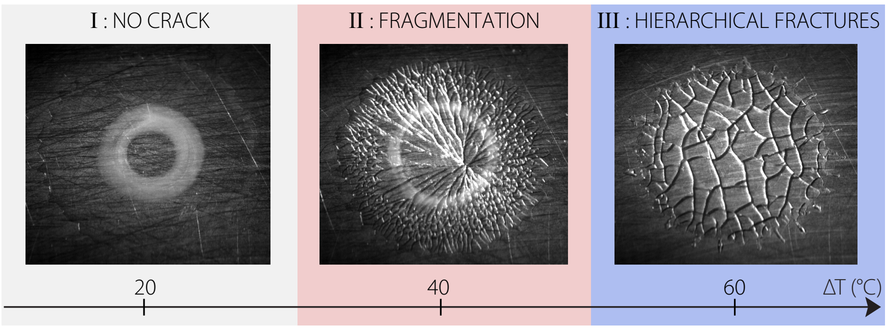

Figure 1.14: Frise présentant des images de goutte étalée et gelée, résultant de l'impact d'une goutte d'eau sur un substrat froid. La chute a eu lieu d'une hauteur de 36 cm. Les trois images correspondent à différentes températures de substrat, de gauche à droite : $T_s = -20.0°$, $-31.1°$, et $-59.6°$C, avec $\Delta T = -T_s$. En fonction de la température du substrat, la goutte gelée présente différents motifs de fracture.

Ruisselet

Le second écoulement capillaire dont nous avons étudié la solidification est l'écoulement d'un fin filet d'eau, aussi appelé ruisselet. Dans notre cas, c'est une petite rivière capillaire, rectiligne, d'environ un centimètre de large et quelques millimètres d'épaisseur, qui coule sur un substrat très froid. Dés

Axel Huerre est en post-doctorat sur ce sujet depuis septembre 2018.

le démarrage de l'expérience, une fine couche de glace commence à croître, sur laquelle l'eau continue de couler. La couche de glace continue alors à s'épaissir jusqu'au moment où elle s'arrête de croître. Le système a alors atteint un état stationnaire où un ruisselet d'eau coule sur un muret de glace statique. La structure de cette couche de glace a une forme étonnamment simple : son épaisseur croît linéairement avec la distance, comme on peut le voir qualitativement sur la Figure 1.15. Quelle est la dynamique de croissance de la glace ? Pourquoi atteint-elle une forme statique alors que le ruisselet continue de couler ? Peut-on expliquer la forme particulière de cette structure de glace ? Trois des questions importantes auxquelles nous avons essayé de répondre [34, 35].

[34] Monier et al. (2020), *Physical Review Fluids*, "Freezing a rivulet".
[35] Huerre et al. (2020), *Subm. to J. Fluid Mech.* "Solidification of a rivulet: shape and temperature fields".

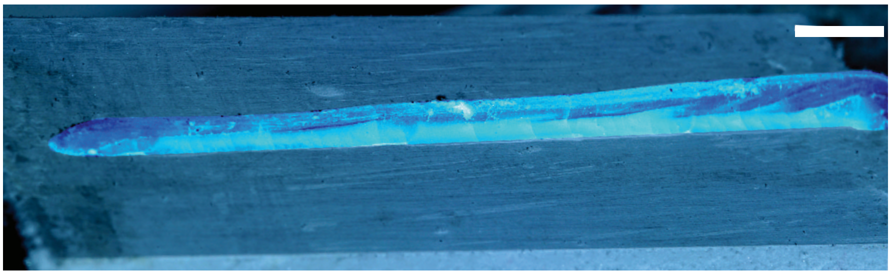

Figure 1.15: Photographie de la structure de glace laissée par la solidification d'un ruisselet après qu'on a arrêté l'écoulement et essuyé l'eau restante. Le ruisselet coulait de gauche à droite. La structure de glace croît avec la distance à l'injection d'eau (de gauche à droite). La barre d'échelle fait 1 cm.

Pour ce faire, nous avons réalisé des expériences en variant les différents paramètres de contrôle : température du substrat, de l'eau, et inclinaison de la pente. Nous les avons analysées à l'aide d'imagerie classique, rapide ou non, et d'imagerie thermique pour mesurer les champs de température. En parallèle, nous avons établi un modèle 2D, basé sur les équations d'advection-diffusion de la chaleur, qui nous permet de prédire la forme de la structure de la glace et les champs de température dans la glace et dans l'eau. Nous montrons que notre modèle capture parfaitement bien les résultats expérimentaux, ce qui nous permet de répondre aux questions cités précédemment. Aux premiers instants, lorsque l'eau commence à couler, une fine couche de glace, homogène sur toute la longueur du ruisselet, commence à croître. Sa dynamique de croissance obéit à une équation de diffusion, tout se passe comme si l'eau était immobile et à 0°C. Ensuite, une fois que la glace est assez épaisse, le flux de chaleur la traversant devient comparable au flux de chaleur apporté par l'eau, l'écoulement du ruisselet commence donc à s'inviter dans le processus et la température de l'eau ne peut plus être négligée. Une couche limite thermique s'est ici établie dans l'eau et a la particularité d'atteindre la surface libre très proche du début du ruisselet. En conséquence, la température de l'eau en surface n'est pas constante, nous montrons théoriquement et expérimentalement qu'elle diminue linéairement à mesure que le ruisselet progresse. C'est ce champ de température particulier dans l'eau, conséquence du confinement de la couche limite thermique par la surface du ruisselet, qui impose à la glace sa forme linéaire. Ajoutons pour finir que la glace s'arrête de croître lorsque le flux de chaleur dans la glace est égal à celui dans l'eau.

1.4 Perspectives

Apres avoir présenté la majorité de mes travaux de recherche ayant abouti à une publication, je vais maintenant introduire les activités que je prévois de développer dans les quelques années à venir. Ceux-ci poursuivent les deux principaux thèmes que j'ai développés depuis mon recrutement : effervescence et solidification capillaire.

Effervescence et applications aux aérosols marins

Nous souhaitons poursuivre les travaux que nous effectuons depuis 2012, dans le but de fournir une estimation, la plus précise possible, de la distribution en taille de gouttes générée par éclatement de bulles au-dessus des océans. Pour cela, nous continuerons notre travail à la fois numérique et expérimentale. Les simulations numériques seront réalisées en utilisant *Basilisk*, logiciel libre développé par S. Popinet. Expérimentalement, deux dispositifs principaux seront utilisés : celui que nous avons à l'Institut ∂'Alembert où une bulle unique peut être étudiée, et un autre, à l'Université de Princeton, dans le groupe de L. Deike, où une multitude de bulles de taille contrôlée peuvent être générées, et les gouttes produites peuvent être caractérisées.

Pour mener à bien notre objectif, trois problèmes principaux seront traités : l'étude conjointe numérique/expérimentale de la rétractation d'un film liquide, de son déchirement et de son atomisation en une multitude de gouttes de film ; l'étude du comportement collectif des bulles en surface qui fait évoluer la distribution de taille générée par le déferlement de vague ; enfin, la convolution des distributions en taille de bulles en surface avec la distribution en taille de gouttes produites par chaque bulle unique que nous aurons obtenue. Cette étude statistique sera comparée aux résultats des expériences réalisées à l'Université de Princeton. Nous décrivons maintenant succinctement ces trois projets.

Gouttes de film

Nous avons vu que lors de l'éclatement d'une bulle deux mécanismes sont à l'origine de la production de gouttelettes. Jusqu'à maintenant nous nous sommes intéressés au gouttes de jet, conséquences de l'effondrement de la cavité. Dans cette partie, nous nous intéresserons donc à ce qu'il se passe avant cet effondrement. En effet, quand une bulle atteint la surface, un film de liquide la sépare de l'atmosphère. Ce dernier se vide peu à peu et lorsqu'il devient assez fin, un mécanisme toujours mal connu conduit à la formation d'un trou. Le film va alors rapidement se rétracter en formant des doigts qui vont chacun produire des gouttelettes (Figure 1.16). Ces gouttes de film viennent donc s'ajouter aux gouttes de jet pour former une grande part des aérosols marins, comme nous l'avons présenté plus haut.

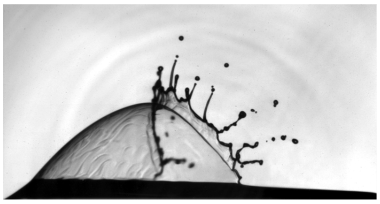
Figure 1.16: Gouttes de film produites lors de l'éclatement d'une bulle à la surface de l'eau. Image : Lhuissier et Villermaux (2012) [36].

Dans ce processus, les détails contrôlant la formation des doigts, leur fragmentation en gouttes, la distribution en taille et en vitesse de ces gouttes et la dépendance de ces distributions en fonction des paramètres de contrôles (taille des bulles, paramètres du liquide) sont peu ou pas connus. Le but de ce travail est d'apporter un maximum de réponses à ces questions. Pour ce faire, nous allons considérer un film plan, puis courbe, avant de passer à une bulle. Nous utiliserons principalement les simulations numériques avec le code Basilisk. Nous résoudrons ce problème en deux puis trois dimensions, et nous comparerons nos résultats aux quelques résultats expérimentaux récents qui existent sur ce sujet [36]. Nous réaliserons aussi des expériences, au moins pour les paramètres de contrôle conduisant aux expérience les plus favorables, sans doute des grosses bulles, avec un liquide légèrement visqueux. Comme pour les gouttes de jet, le premier objectif ici est de connaître la distribution en tailles de gouttes de film en fonction de la distribution en tailles de bulles. En octobre 2020, H. Vaziri commencera sa thèse sur ce sujet, il sera codirigé avec S. Popinet.

[36] Lhuissier et al. (2012), *Journal of Fluid Mechanics*, "Bursting bubble aerosols".

Effets collectifs

Grâce à l'étude sur les gouttes de jet et de film, nous pouvons corréler les gouttes produites aux bulles mères, par exemple générées lors du déferlement d'une vague. Mais nous rappelons qu'ici toutes les études ont été réalisées avec des bulles uniques, il nous manque donc tous les effets collectifs. Ils sont liés au fait que lorsque les bulles atteignent la surface, elles sont très proches les unes des autres (Figure 1.17), et donc elles s'influencent, interagissent, coalescent, bougent avant d'éclater.

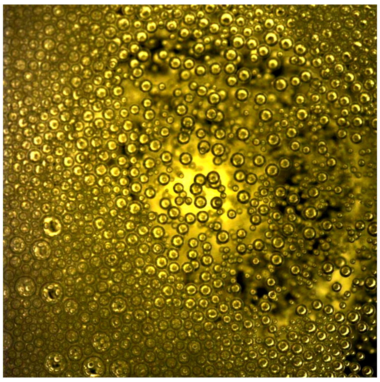
Figure 1.17: Surface d'un liquide couverte de bulles.

Ces effets collectifs jouent un rôle à deux niveaux : dans l'évolution de la distribution en taille des bulles et dans la modification des processus de génération de gouttes par rapport au cas de la bulle isolée. Dans un premier temps, nous étudierons expérimentalement l'évolution d'une population de bulles posée à une surface libre. Pour ce faire, nous générerons une distribution connue de tailles de bulles et nous la regarderons évoluer dans le temps. Dans un second temps, nous nous intéresserons à l'influence des bulles voisines sur les mécanismes de génération de gouttes et sur les distributions produites. Nous ferons ainsi éclater des bulles au sein d'un radeau et nous comparerons les caractéristiques des gouttes de jet et de film à celles connues dans cas de la bulle unique.

Échanges océan-atmosphère

À ce stade, nous serons en mesure de prédire les distributions de taille de gouttes produites par la remontée en surface d'une distribution connue de taille de bulles. Ces résultats seront comparés à ceux d'une expérience montée à l'Université de Princeton, dans le groupe de L. Deike, où il est possible d'injecter une population contrôlée de bulles et de mesurer les gouttes générées. Cette expérience est illustrée sur la Figure 1.18. Ces mesures devront être effectuées sur un grand nombre d'expériences pour pouvoir reconstruire proprement les distributions statistiques recherchées.

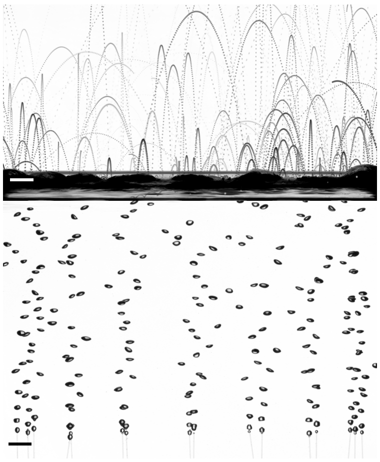
Figure 1.18: Bas : ascension de bulles millimétriques. Haut : trajectoires des gouttes de quelques centaines de microns, révélées par la superposition de 800 images enregistrées à 500Hz. Barres d'échelle : 1 cm. Images réalisées par B. Néel et L. Deike, à Princeton University.

Pour que cette étude soit complète il faudra enfin travailler sur les échanges liquide-gaz induits par ces aérosols. Nous avons déjà proposé un modèle d'évaporation qui fournit une prédiction de la masse d'eau transférée à l'air par les gouttes de jet. Les résultats de ce modèle devront être comparés aux résultats numériques, que nous pourrons obtenir une fois la transition de phase liquide-gaz ajoutée dans le code Basilisk. Ce type de simulation complète constitue un objectif à plus long terme de ce travail.

Les échanges entre l'océan et l'atmosphère jouent un rôle prépondérant dans le système climatique terrestre et il faut donc en avoir une bonne estimation si on veut pouvoir modéliser au mieux ce système complexe. Ces flux sont encore estimés en utilisant des relations empiriques, souvent mal contraintes par les mesures de terrain. Nous espérons améliorer nettement ces estimations grâce à cette approche ascendante qui part de l'événement local pour nourrir les résultats à grande échelle.

Solidification de systèmes complexes : films et gouttes

L'objectif de ce travail multidisciplinaire, que nous avons démarré il y a environ cinq ans, est l'étude de la formation de glace dans des systèmes hydrodynamiques capillaires tels que des gouttes en écoulement (impact, dévalement), des rivulets, des films liquides en ruissellement, des films de savon, des mousses, des milieux poreux... Ce travail est d'un intérêt fondamental pour la communauté scientifique car le couplage entre effets capillaires et solidification révèle des comportements que la connaissance actuelle n'expliquait pas, et il représente aussi un défi majeur dans l'industrie, notamment l'industrie aéronautique, où les solutions existantes pour empêcher l'accrétion de glace sur un avion sont coûteuses et peu efficaces.

Ce projet de recherche est vaste, jusqu'à maintenant nous avons étudié l'impact d'une goutte d'eau et l'écoulement d'un rivulet sur un substrat froid ([0, -100]°C). Dans la suite, nous allons nous pencher sur le couplage entre ruissellement et solidification d'un film liquide. La question fondamentale du mouillage de l'eau sur la glace traitée en profondeur. En parallèle, nous développerons une activité autour de la solidification de systèmes capillaires désordonnés comme les mousses liquides ou les milieux poreux imbibés.

Solidification de film ruisselant et de stalactites

Sur la Figure 1.19, un film d'eau ruisselant sur le plafond d'une grotte en Sibérie a formé des structures de glace bien particulières. Il semble qu'il y ait eu une déstabilisation du film qui a formé une succession de filets d'eau, qui eux-mêmes se sont déstabilisés pour former des stalactites. Ici, nous proposons d'étudier le problème de la formation de glace lors du ruissellement d'un film mince sur une surface froide. Dans un premier temps, le film d'eau ruissellera sur la face supérieure de la surface froide, puis sur la face inférieure comme sur la Figure 1.19.

Figure 1.19: Structures de glace formées par le ruissellement d'eau sur le plafond d'une grotte en Sibérie. Photo de V. Thiévenaz.

L'expérience modèle consistera à faire s'écouler des films minces, par gravité, en contact avec des plaques de métal qui seront refroidies à des températures pouvant atteindre -60°C. Le film pourra donc s'écouler sur la face supérieure ou inférieure de la plaque ; dans les deux cas, la dynamique de formation des structures de glace sera étudiée au cours du temps et la forme finale sera caractérisée. On s'attend à ce qu'elle présente des motifs périodiques particuliers, dus notamment au démouillage de l'eau sur la glace. L'étude ces motifs permettra de progresser sur la compréhension du couplage entre la dynamique capillaire de l'eau sur la glace et sa solidification. Lorsque le film s'écoule sur la face inférieure de la plaque, des stalactites se formeront et leur formation sera étudiée. L'influence de la température de l'air sera caractérisée par des expériences réalisées dans une chambre froide (-30°C). Simon Brient commence sa thèse de doctorat en octobre 2020 sur cette thématique.

Solidification de gouttes et de stalagmite

Les trois années de la thèse de V. Thiévenaz n'auront évidemment pas suffi à cerner tous les mécanismes liés à la solidification de goutte à l'impact. Je note dans les paragraphes qui suivent les deux principaux axes que nous souhaitons poursuivre.

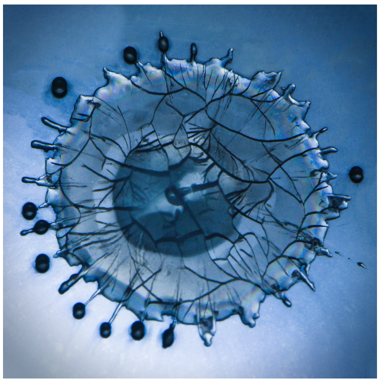

Figure 1.20: "Splash" d'une goutte induit par la solidification à l'impact.

Solidification de splash Nous avons montré, au cours de nos études précédentes, que la solidification à l'impact pouvait engendrer la déstabilisation de la ligne de contact lors de l'étalement de la goutte et ainsi être à l'origine de la génération d'éclaboussure (Figure 1.20). Ce phénomène nouveau, qui conjugue dynamique et solidification de la ligne de contact, constituera un axe de recherche.

Impacts multiple et stalagmite Une glacière naturelle est une grotte où la température reste négative tout au long de l'année. C'est une formidable scène pour l'émergence de structures de glace de toutes sortes. C'est là qu'on trouve notamment les stalagmites de glace du type de celles de la Figure 1.21, mais aussi des "bamboo-shaped" stalagmites qui exhibent une succession régulière de parties épaisses et fines [37]. Certaines stalagmites de glace dépassent les cinq mètres. La forme et l'aspect de ces structures dépend du débit du goute-à-goutte, de la température de l'eau, de l'air et du sol. Connaître ces dépendances permettrait donc de remonter aux valeurs passées de ces paramètres importants. Nous souhaitons reproduire en laboratoire ces structures de glace et, pour ce faire, nous réaliserons une expérience de goutte-à-goutte sur un substrat froid et dans une atmosphère froide. Ansi, nous pourrons étudier la dynamique de formation de ces structures, améliorer notre compréhension de leur forme et leur aspect, et connaître leur dépendance avec les paramètres de contrôle.

Figure 1.21: Stalagmite de glace.

[37] Persoiu et al. (2018), , "Ice caves".

Solidification de films de savon

Nous proposons d'explorer la solidification de films de savon dans plusieurs géométries : rectangle, disque, caténoïde ou sphère, dont un exemple est montré en Figure 1.22. Les objectifs sont multiples : d'une part connaître la dynamique de solidification dans ces films, ce qui aura pour conséquence de fournir une brique élémentaire de compréhension pour l'étude de la solidification des mousses que nous décrirons après ; d'autre part, évaluer l'effet du confinement et de la courbure sur la propagation d'un front de solidification dans un système modèle 2D. Dans un premier temps, les films de savons seront fixés sur des cadres en métal. Le refroidissement d'un des bords du cadre permettra de contrôler la nucléation de glace. Dans un second temps, l'atmosphère environnante sera refroidie de manière à induire une nucléation spontanée dans le système. Les films pourront être statiques ou en écoulement (films verticaux alimentés en liquide par le haut par exemple).

Figure 1.22: Photographie d'une bulle de savon qui gèle.

Solidification de milieux désordonnés

L'objectif de ce projet vise à mieux appréhender la solidification de systèmes multi-échelles désordonnés constitués de réseaux de canaux capillaires liquides inter-connectés. Pour ce faire, nous proposons de réaliser une étude expérimentale de la dynamique de gel dans deux milieux cellulaires modèles : les mousses liquides et les granulaires mouillés. Les mousses liquides sont un ensemble de bulles de gaz immergées dans une matrice liquide, et les milieux granulaires considérés consistent en un empilement de billes immergé dans un liquide. Les deux milieux sont donc des matériaux poreux, un liquide-gaz et l'autre liquide-solide, dont le diamètre des canaux varie de quelques dizaines de nanomètres au millimètre.

Tout d'abord, nous nous attacherons à l'étude de systèmes à deux dimensions : des mousses liquides (Figure 1.23), et des granulaires humides, confinés à l'échelle de la bulle unique, ou du grain, dans une cellule de Hele-Shaw. Ensuite, le changement de phase dans ces milieux désordonnés 3D sera caractérisé. Nous nous intéresserons à une colonne de mousse, ou de grains, que l'on refroidit par le bas, et nous nous demanderons comment le front de propagation progresse dans un tel système : est-il diffusif ? Si oui peut on prédire la valeur du coefficient de diffusion ?...

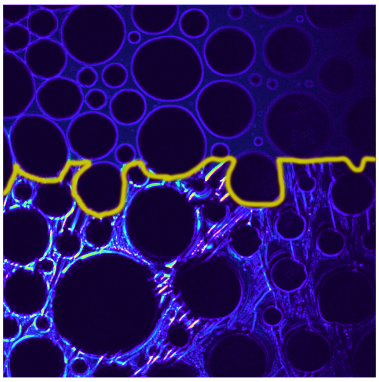

Figure 1.23: Image confocale du front de solidification (surligné en jaune) dans une mousse humide. Les grosses bulles font 50 μm. Expérience réalisée avec S. Deville.

Ce travail nous permettra d'atteindre différents objectifs ; certains de nature fondamentale, comme la caractérisation et la compréhension de la propagation d'un front de solidification dans ces milieux poreux. L'étude parallèle de la solidification de films de savon aidera à cette tâche. D'autres sont plus appliqués, comme par exemple l'amélioration de techniques de fabrication de mousses solides, ou la progression de notre connaissance des mécanismes en jeu lors du gel et du dégel des sols, un milieu poreux naturel. Ainsi, notre travail a vocation à aider la compréhension de certains comportements particuliers du pergélisol, comme par exemple les phénomènes d'effondrement, ou de gonflement (Figure 1.24), qui posent de graves problèmes de sécurité publique.


Figure 1.24: Un pingo est une colline de glace recouverte de terre. Ceux sur cette photo sont à proximité de Tuktoyaktuk dans les Territoires du Nord-Ouest au Canada.

1.5 Les lois d'échelle

Pour terminer, je voudrais présenter le livre dont la couverture est en Figure 1.25. Il n'est pas directement le fruit de mon travail de recherche mais plutôt un travail de synthèse et de vulgarisation, destiné à tous lecteurs intéressés par la science et à l'aise avec les outils mathématiques les plus élémentaires. Ce livre intitulé *Les Lois d'échelle: La Physique du petit et du grand*, est paru le 31 octobre 2018 aux éditions *Odile Jacob*. C'est donc un ouvrage pédagogique centré autour des lois d'échelle, il introduit l'analyse dimensionnelle et présente les notions de similitude, de nombre sans dimension, *etc.* Ces sujets sont traités au travers de nombreux exemples de la vie de tous les jours : la forme des arbres, celle d'une goutte d'eau, le métabolisme des mammifères, leur espérance de vie, la vitesse de marche, de vol, de nage des animaux, l'architecture navale, les avalanches... Les quelques paragraphes qui suivent en font une introduction un peu plus étayée en en reprenant l'avant propos.

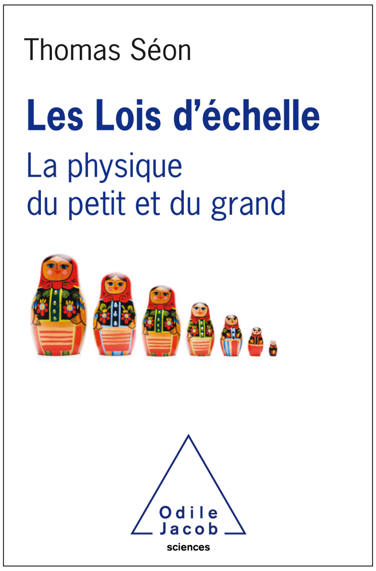
Thomas Séon

Les Lois d'échelle

La physique
du petit et du grand

Odile
Jacob
sciences

Figure 1.25: Couverture du livre *Les Lois d'échelle: La Physique du petit et du grand*, paru le 31 octobre 2018 aux éditions *Odile Jacob* (256 pages).

L'impressionnisme peut être vu comme une volonté de regarder l'essentiel sans s'encombrer des « détails ». Cette attitude, appliquée à la science, permet de décrire le monde qui nous entoure en en dégageant les mécanismes dominants. Il faut réduire un problème à son épure pour en avoir une description à la fois simple et générique et ainsi en extraire la physique sous-jacente. Car l'objectif n'est pas simplement de décrire mais avant tout de *comprendre* les phénomènes présentés. Cette démarche structure chacune des pages de ce livre.

Le moyen le plus simple de présenter une telle description est de l'écrire sous la forme d'une loi, au sens mathématique du terme, mais sans la complexité qui l'accompagne d'ordinaire. Avec un bagage mathématique réduit à son plus simple appareil, nous aboutirons à des lois de la nature tout à la fois simples et universelles. Ces relations, indépendantes de l'échelle considérée, sont appelées *lois d'échelle*. Comme elles sont par essence génériques, elles permettent d'apporter un peu d'unité dans l'extraordinaire diversité et complexité du monde qui nous entoure. Selon les cas, une loi pourra décrire tous les mammifères, de la musaraigne à la baleine, ou tout ce qui vole, du moustique à l'airbus, ou tout ce qui nage, tombe ou flotte.

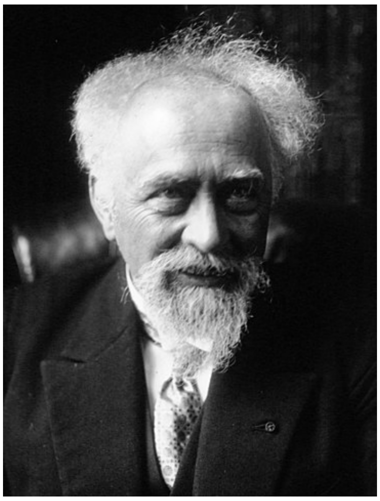
Figure 1.26: Jean Perrin (1870-1942) - Prix Nobel de physique 1926 : "La science consiste à découvrir des principes simples cachés par la complexité du réel."

Jean Perrin (Figure 1.26), prix Nobel de physique (1926) et fondateur du Centre national de la recherche scientifique (CNRS), disait que la science consiste à « découvrir des principes simples cachés par la complexité du réel ». C'est exactement ce que nous allons faire avec notre approche impressionniste : éclairer les ingrédients essentiels du système observé, découvrir les lois qui décrivent une réalité d'apparence complexe, et les interpréter pour en dégager toute la compréhension accessible. Par cette démarche, nous nous faisons l'écho de toute une école de pensée, une méthode scientifique dont un autre prix Nobel de physique (1991), Pierre-Gilles de Gennes (Figure 1.27), fut l'une des figures de proue les plus emblématiques.

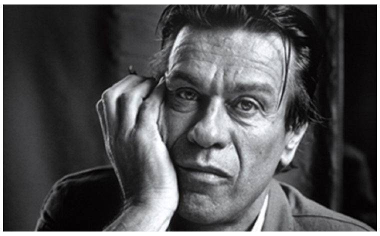

Figure 1.27: Pierre-Gilles de Gennes (1932-2007) - Prix Nobel de physique 1991 : "Il faut prendre du recul et faire une description impressionniste du monde."

Les lois d'échelle sont un formidable outil de vulgarisation. Elles apportent un formalisme simple mais extrêmement puissant, qui permet de discuter des mécanismes à l'origine d'une variété considérable de sujets, sans s'embarrasser de détails. Cet ouvrage s'adresse donc à une communauté d'amateurs de science au sens large, à travers des questions diverses, souvent fondamentales et *a priori* complexes : quelle est la forme d'un arbre ? Pourquoi a-t-il cette forme ? Comment la taille d'un animal influence-t-elle son apparence, sa consommation de nourriture ou son espérance de vie ? Comment marche un homme, vole un oiseau ou nage un poisson ? Comment estimer la puissance nécessaire à un sous-marin ou un navire ? Quel est le point commun entre une bulle et une tempête de sable ? Quelle est la forme d'une goutte ? Le lectorat un peu plus familier avec l'outil mathématique trouvera aussi deux interludes, et quelques encadrés, dans lesquels sera abordée la méthode permettant de déterminer ces lois d'échelle : *l'analyse dimensionnelle*. Les relations seront écrites en ne raisonnant que sur les dimensions de chaque grandeur : c'est élémentaire et extrêmement efficace.

Physics of Effervescence

2

2.1 Introduction

Sea spray refers to aerosol particles in the atmosphere that are formed directly from the ocean. These drops play a crucial role in the exchange between the ocean and atmosphere by evaporating and transporting water, heat, dissolved gases, salts, surfactants, and organic matter [38, 39]. Consequently, sea spray is directly responsible for a significant degree of the heat and moisture fluxes between the atmosphere and the ocean [40] affecting global climate patterns and tropical storm intensity [41]. Among the other main consequences of this aerosol there are a global emission of about 10^{12} to 10^{14} kg per year of sea salt in the atmosphere that serve as cloud condensation nuclei [14]. Sea spray also influences plant growth and species distribution in coastal ecosystems [42] and increases corrosion of building materials in coastal areas [43].

Sea spray is composed of small liquid droplets formed through two main pathways (Figure 2.1): the spume drops, produced from the tearing of breaking wave crests by strong winds [44] and the bursting bubbles drops [45, 46] produced after a breaking wave event has entrained air below the sea surface [15, 16, 47]. Indeed, after a bubble rises in ocean, it reaches the surface and the thin film which separates the bubble from the atmosphere, the bubble cap, drains and ruptures [14]. From then, two events in a row are producing droplets (Figure 2.2): first, the film shattering expels $O(10-100)$ of small *film drops* [36], and then the remaining unstable cavity collapses and shoots up a central jet, that becomes unstable and breaks up into several larger *jet drops* [48]. Most of film drops are less than 1 μm in radius while jet drops span in the range from 1 to 200 μm [14]. Sea spray is largely attributed to an estimated 10^{18} to 10^{20} bubbles that burst every second across the oceans [38].

Figure 2.1: Sea spray generated by breaking surface waves.

[38] Lewis et al. (2004), , "Sea Salt Aerosol Production. Mechanisms, Methods, Measurements, and Models".
[39] Leeuw et al. (2011), *Rev. Geophys.* "Production flux of sea spray aerosol".

[40] Andreas et al. (1995), *Boundary-Layer Meteorol.* "The spray contribution to net evaporation from the sea: A review of recent progress".

[14] Veron (2015), *Annual Review of Fluid Mechanics*, "Ocean Spray".

[45] Blanchard (1963), *Progress In Oceanography*, "The electrification of the atmosphere by particles from bubbles in the sea".
[46] Spiel (1995), *J. Geophys. Res.* "On the births of jet drops from bubbles bursting on water surfaces".

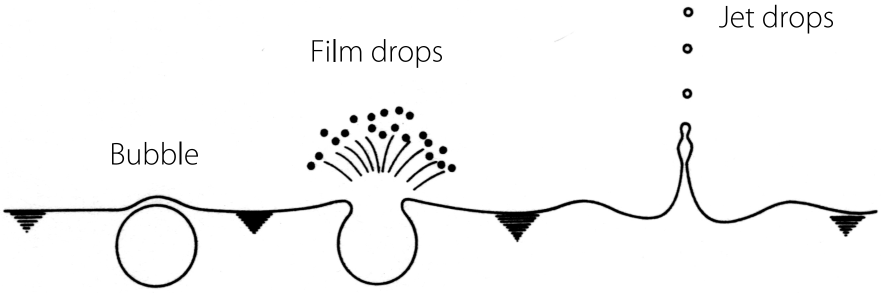

Figure 2.2: Scheme of the two production ways of droplets from a bursting bubble; redrawn from Ref. [49].

[49] Resch et al. (1986), *J. Geophys. Res.* "Marine Liquid Aerosol Production From Bursting of Air Bubbles".
[50] Woodcock et al. (1953), *Nature*, "Giant Condensation Nuclei from Bursting Bubbles".

[54] Duchemin et al. (2002), *Phys. Fluids*, "Jet formation in bubbles bursting at a free surface".

The work presented in this chapter is dedicated to jet drops production. Since the pioneering study of bursting bubbles published by Woodcock *et al.* in 1953 [50], the past sixty five years have witnessed a number of laboratory studies documenting jet drops properties [45, 46, 51–53]. The first comprehensive study, realized by Duchemin *et al.* [54] using numerical simulations, showed that fast jets are produced by the self-similar collapse of a cavity, but the numerical results, of jet velocity for example, did not match the experimental observation and a comprehensive picture of the mechanisms at play in bubble bursting were still lacking. This is how we started to work on this topic in 2012 and this chapter is gathering the main results of our work since then.

2.2 Experimental setup and numerical method

Experimental setup

Our experiment has been designed to be a model experiment of effervescence. It consists in releasing a single air bubble from a needle submerged in a liquid and recording the bubble bursting at the free surface and the ejected droplets. The liquids used include 13 solutions of water-glycerol-ethanol mixtures of viscosity in the range $\mu = 1 - 12$ mPa.s, surface tension $\gamma = 23 - 72$ mN.m^{-1}, and density $\rho = 780 - 1160$ kg.m^{-3}. Different needle diameters ([$5 - 1800$ μm]) allow us to create bubbles with various radii (R_b) ranging from 300 μm to 3 mm. The bubble collapse, drop velocity and drop size are analyzed through close-up and fast imagery (Photron SA-5). Depending on the experiment, frame rate is varied from 1000 to 400 000 images per second. Macro lenses and extension rings allow us to record with a definition reaching 7 μm per pixel. The jet speed V_{jet} is measured when the tip of the jet reaches the mean water level and the top drop speed V_{d} is measured when the first drop detaches from the jet. The top drop trajectory is recorded at 1000 frames per second, using a second digital high-speed camera (Phantom v7.11), triggered by the first one when the bubble collapses.

[36] Lhuissier et al. (2012), *Journal of Fluid Mechanics*, "Bursting bubble aerosols".
[17] Ghabache et al. (2014), *Physics of Fluids*, "On the physics of fizziness: How bubble bursting controls droplets ejection".
[48] Ghabache (2015), , "Surface libre hors équilibre : de l'effondrement de cavité aux jets étirés".

Static shape of a floating bubble

When the bubble reaches the free surface, it adopts an equilibrium shape which is the result of the competition of surface tension and gravity and can thus be obtained theoretically by solving the Young–Laplace equations [17, 36, 48]. Figure 2.3 displays in green the corresponding numerical profile superimposed on an experimental snapshot of a bubble before bursting. The agreement is perfect. Moreover, it is clear that the bubbles are not spherical, so we need to defined an equivalent radius. The red dashed line is a semi-elliptic fit of the bottom part of the static bubble. It captures properly the inferior half of the bubble and consequently allows us to define the bubble parameters: a, b, and the corresponding bubble radius:

$$R_b = (a^2 b)^{1/3}. \tag{2.1}$$

a and b identify respectively the semi-minor and semi-major axis of the ellipsoid.

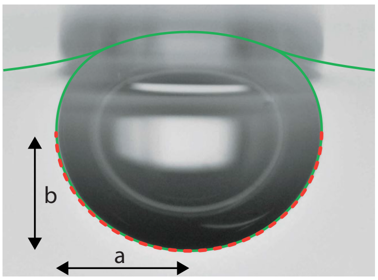

Figure 2.3: Picture of a static floating bubble at the free surface. Green profile is obtained by numerical integration of the Young–Laplace equation using Mathematica software [36, 55]. The red dashed line is a semi-elliptic fit of the bottom part of the static bubble. a and b identify respectively the semi-minor and semi-major axis of the ellipsoid.

Numerical method

The 2D axisymmetric simulations were performed first by L. Deike [47] and since 2018 by A. Berny [20]. They used respectively the open source solver Gerris and the Basilisk open-source library, solving the two-phase incompressible Navier–Stokes equations with surface tension. The adaptive mesh is critical to the success of these simulations as it allows fast solution for discretizations with an equivalent resolution of up to 4^{14} grid points.

We initialize the liquid-gas interface with the theoretical static shape of the bubble cavity left after the initial film breaks-up (Figure 2.3). The initial condition of the simulation is therefore a close match to the experimental one. The density and viscosity ratios is set to $\rho_{\text{liq}}/\rho_{\text{gaz}} = 998$ and $\mu_{\text{liq}}/\mu_{\text{gaz}} = 55$, which is close to the values for air and water.

[47] Deike et al. (2017), *Geophysical Research Letters*, "Air entrainment by breaking waves".

[20] Berny et al. (2020), *Physical Review Fluids*, "Role of all jet drops in mass transfer from bursting bubbles".

Control parameters and dimensionless number

The control parameters in this problem are the bubble radius R_b, the gravity g and the liquid parameters: viscosity μ, surface tension γ and density ρ. The system is therefore fully described by only two dimensionless numbers. One of them is the Bond number, which compares the effect of gravity and capillarity:

$$\mathrm{Bo} = \frac{\rho g R_b^2}{\gamma}, \tag{2.2}$$

It will usually be interpreted as a nondimensional bubble radius. The other one can be the Morton number, which only depends on the fluid properties and, consequently, has the advantage of being constant for a given fluid:

$$\mathrm{Mo} = \frac{g\mu^4}{\rho\gamma^3}, \tag{2.3}$$

This number will be used in the experimental study. However it is hard to interpret as it mixes all parameters, consequently we will also use the Laplace number instead, it compares the effect of inertiocapillarity and viscosity:

$$\mathrm{La} = \frac{\rho\gamma R_b}{\mu^2}, \tag{2.4}$$

This dimensionless number is similar to a Reynolds number with a capillary velocity, it will be used in the numerical study. It will usually be interpreted as a nondimensional inverse viscosity. Note that the Morton number can be expressed as a function of the Laplace number: $\mathrm{Mo} = \mathrm{Bo}\mathrm{La}^{-2}$.

2.3 Cavity collapse and jet dynamics

Let us now look at the collapse of the unstable open cavity and the subsequent jet dynamics. We bring a new comprehensive picture of the mechanisms at play in bubble bursting. In particular, the sequence of violent events preluding jet formation [54, 56] and the roles of liquid properties are discussed.

This section is mainly extracted from: [17] Ghabache et al. (2014), *Phys. Fluids*, "On the physics of fizziness: How bubble bursting controls droplets ejection".

Jet velocity dependance with bubble size in water

Figure 2.4 illustrates a typical jetting event following a bubble bursting at a free surface in water. The top sequence shows the free surface view while the bottom one displays the underwater dynamics. The top sequence takes place between the two first images of the bottom one as indicated by the arrows. The first image of the top sequence shows our static bubble from the top. Then the film separating the bubble from the atmosphere drains and bursts leaving the unstable open cavity. This cavity is millimeter-sized so the restoring force which tends to bring this hole back to a flat equilibrium is capillary driven. Bottom sequence displays capillary waves propagating along this cavity and focusing at the bottom. These collapsing waves give rise to the high speed vertical jet shooting out above the free surface as observed on the top sequence. The jet then fragments into droplets due to end pinching mechanism (described in Section 2.5) generating an aerosol of one to twenty droplets.

[56] MacIntyre (1972), *Journal of Geophysical Research*, "Flow patterns in breaking bubbles".
[54] Duchemin et al. (2002), *Phys. Fluids*, "Jet formation in bubbles bursting at a free surface".

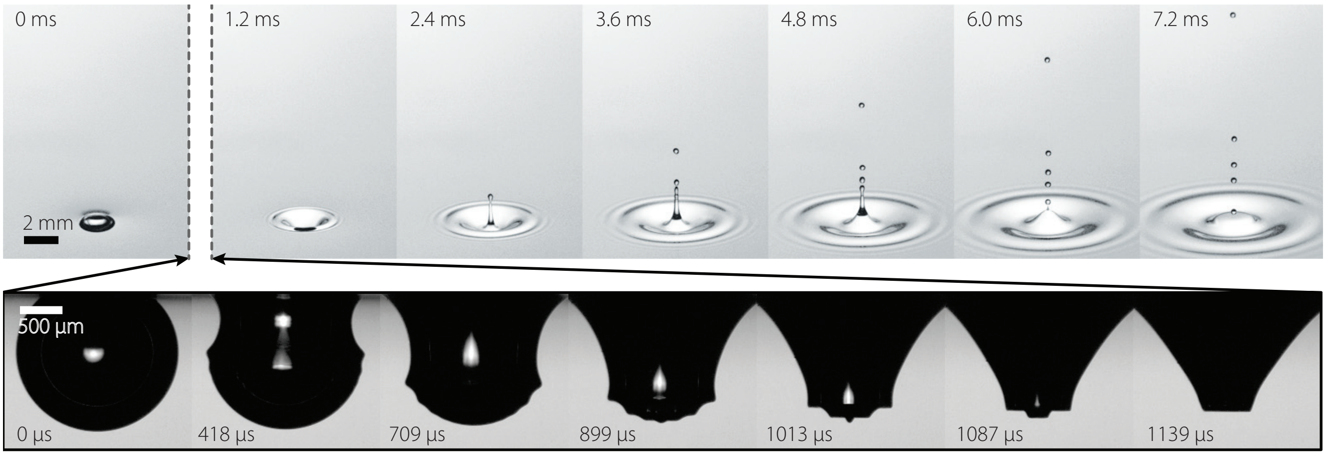

Figure 2.4: Time sequence of a typical jetting event following a bubble bursting at a free surface in water. The top sequence shows the bubble bursting event above the free surface, while the bottom sequence displays the bubble under the free surface during the collapse giving birth to the vertical upward jet. The bottom sequence takes place between the two first images of the top one. The times are shown on the snapshots with the same origin.

In order to establish the role played by the relevant parameters in the jet dynamics, we express the jet tip velocity V_{jet} as a function of the control parameters using the following relation between the three dimensionless numbers that fully describe the jet dynamics:

$$\text{We} = F(\text{Bo}, \text{Mo}), \tag{2.5}$$

where the Weber number We (see definition in the margin), which compares the effect of inertia and capillarity on the jet dynamics, is a function of the Bond number and the Morton number, that have been introduced in Section 2.2. Various scaling relations for the velocity are reported in the literature, ranging from exponential fits of experimental data [46] (see curved dashed line in Figure 2.5) to algebraic laws $V_{\text{jet}} \propto R_b^{-1/2}$ in numerical simulations disregarding gravity [54]. This diversity certainly emphasized the need for further experimental analysis.

$$\text{We} = \frac{\rho V_{\text{jet}}^2 R_b}{\gamma}$$

$$\text{Bo} = \frac{\rho g R_b^2}{\gamma}$$

$$\text{Mo} = \frac{g \mu^4}{\rho \gamma^3}$$

[46] Spiel (1995), *J. Geophys. Res.* "On the births of jet drops from bubbles bursting on water surfaces".

[54] Duchemin et al. (2002), *Phys. Fluids*, "Jet formation in bubbles bursting at a free surface".

We set out by investigating experimentally in Figure 2.5 the dependence of V_{jet} with R_b in a log-log plot. Our experimental data (red circles) rest along the line $V_{\text{jet}} \propto R_b^{-1}$, as indicated by the red dashed line fitting the experimental velocities. Note that bubbles with $\text{Bo} > 1$ (radii greater than 3mm) give rise to jets with a different dynamics and are not considered in this study. On the same figure various data from the literature have been plotted: the top drop velocity measured experimentally in fresh water [46] or in sea water [45], and the maximum tip velocity of the jet computed numerically in fresh water [53]. Regardless of some slight differences they all follow the same trend $V_{\text{jet}} \propto R_b^{-1}$. This specifies the form of Equation 2.5 providing the variation with Bond number, yielding:

[45] Blanchard (1963), *Progress In Oceanography*, "The electrification of the atmosphere by particles from bubbles in the sea".

[53] Boulton-Stone et al. (1993), *Journal of Fluid Mechanics*, "Gas bubbles bursting at a free surface".

$$\text{We} = \text{Bo}^{-1/2} f(\text{Mo}). \tag{2.6}$$

The R_b^{-1} behavior is the footprint of gravity effects. Though the Bond number remains small in the experiments, the gravity plays a role in the collapse dynamics through the initial static bubble shape. Note that Froude number of the jet at the mean water level is $\text{Fr} = V_{\text{jet}}/\sqrt{g R_b} = \sqrt{\text{We}/\text{Bo}}$, and can be expressed here as $\text{Fr} = \text{Bo}^{-3/4} f(\text{Mo})^{1/2}$. In water, with the Bond values of Figure 2.5 one obtains $\text{Fr} \in [7 - 160] > 1$, indicating that gravity hardly affects the initial jet dynamics confirming the role of the initial shape in the jet velocity selection.

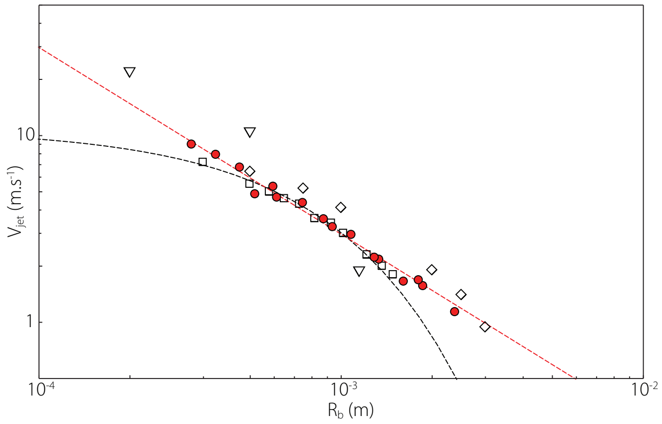

Figure 2.5: Jet velocity V_{jet}, measured when the jet passes the free surface level, as a function of the bubble radius R_b in water, from our experiments (red circle) and data from the literature: (square) top drop velocity along with the exponential fit represented by the curved dashed line $V \propto e^{-1.27.10^3 R_b}$ [46] , (diamonds) maximum tip velocity computed numerically [53] and (triangle) top drop velocity [45]. The red dashed line is a fit of our experimental data exhibiting the common trend $V_{\text{jet}} \propto R_b^{-1}$.

Jet velocity dependance with liquid properties

We now investigate how the jet eruption velocity V_{jet} depends on the liquid properties and therefore on the Morton number. The Weber number is plotted as a function of the Bond number for various Morton number on Figure 2.6 (a). To browse the Morton range we mainly change the liquid viscosity (see table of Figure 2.6). The first clear observation is that the jet dynamics depends on the viscosity although the jet Reynolds number is greater than 1. Furthermore, the regime $\mathrm{We} \propto \mathrm{Bo}^{-1/2}$ is retained on around four decades in Morton number, from 1 mPa.s to around 7.5 mPa.s, all plotted with filled symbols. Finally, for values of viscosity less than 6 mPa.s we observe a surprising increase of the Weber number with Morton number, meaning that for a given bubble radius in this range, *the jet is drastically faster as the liquid viscosity is increased.*

The non-dimensional jet velocity $\mathrm{We}\,\mathrm{Bo}^{1/2}$ is plotted as a function of the Morton number on Figure 2.6(b), therefore specifying $f(\mathrm{Mo})$ (see Equation 2.6). A bell shaped curve is clearly observed with a maximum for $\mu \simeq 5$ mPa.s. To illustrate this unexpected behavior we display inside Figure 2.6 four snapshots of the jet at the same dimensionless time ($\mathrm{t}/\sqrt{\rho R^3/\gamma} = 1/5$), same Bond number ($\mathrm{Bo} \simeq 0.14$) but four different Morton numbers. The jet shape undergoes a neat qualitative change as the liquid gets more viscous: the jet first becomes thinner, detaching more and smaller droplets and then ends up fat and small for high Morton number.

Capillary wave dynamics and cavity collapse

In order to grasp the mechanisms leading to such a particular dynamics, we now turn to the jet formation by focusing on the cavity collapse *per se*. Lower sequence of Figure 2.4 displays a typical bubble collapse in water, where a train of capillary waves propagates, converges to the nadir (bottom of the cavity), and gives rise to the jet. Figure 2.7 (a) to (c) show a temporal zoom of the last microseconds before the cavity collapses ($t \simeq t_0$) for three different Morton numbers and same Bond number. These three sequences are the cavity collapse leading to the three jets (1), (2) and (3) displayed on Figure 2.6. On the last image of each sequence the cavity is reversed and the upward jet (not seen on the picture) is developing. These sequences show that the cavity reversals are very similar between the 6.2 mPa.s (b) and 12 mPa.s

	●	■	◀	⬢	△	◆	✡	▶	○	△
µ (mPa.s)	1	1.2 Eth	2.1	3.3	4.4	5.2	6.2	7.4	9.7	12
Mo	$2.6\ 10^{-11}$	$2.1\ 10^{-9}$	$6.0\ 10^{-10}$	$3.9\ 10^{-9}$	$1.1\ 10^{-8}$	$2.3\ 10^{-8}$	$4.9\ 10^{-8}$	$9.8\ 10^{-8}$	$2.9\ 10^{-7}$	$6.7\ 10^{-7}$

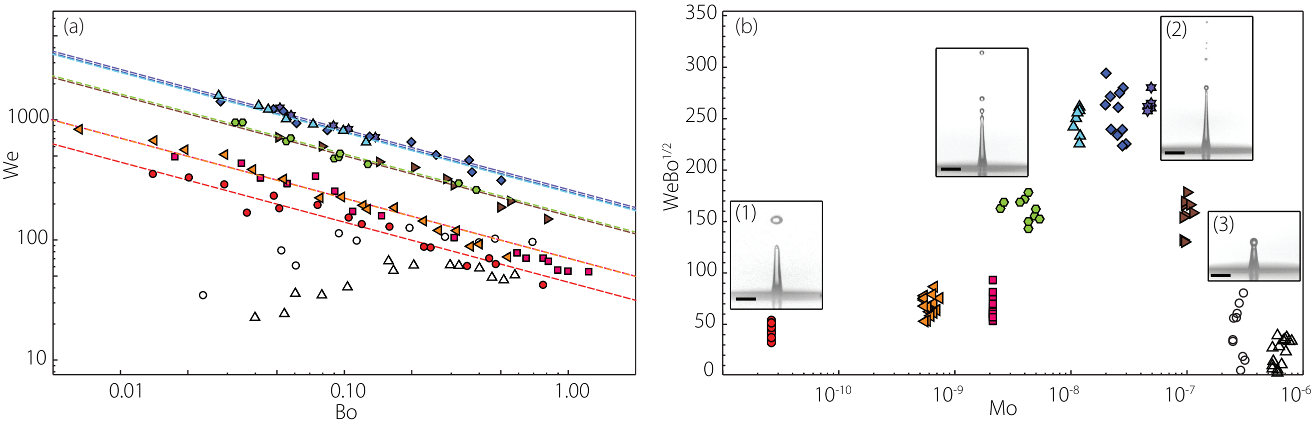

Figure 2.6: Table: Value of the liquid viscosity and of the associated Morton number corresponding to each symbol. Eth. stands for Ethanol . (a) Weber number as a function of the Bond number for various values of the Morton number. All the colored symbols follow the same trend $\mathrm{We} \propto \mathrm{Bo}^{-1/2}$ as showed by the dashed lines. (b) $\mathrm{We\,Bo}^{1/2}$ as a function of the Morton number Mo. Four snapshots display the typical jet observed at the same dimensionless time $(\mathrm{t}/\sqrt{\rho R^3/\gamma} = 1/5)$, same Bond number ($\mathrm{Bo} \simeq 0.14$) and four different Morton numbers corresponding to red circle, green hexagon, purple star, empty triangle. The black bar represents 500 μm.

(c) solutions and drastically different from water (a). In particular the small capillary waves present in the water collapse (a) have disappeared for higher viscosities (b) and (c). It has been shown in numerical simulation [54] and in other experimental contexts [57, 58] that such collapse exhibits a self-similar dynamics that can lead in some cases to very thin and rapid jets. In such a situation, the cavity collapses, through a nonlinear balance between capillary force and inertia, leads to a self-similar behavior where the lengths scale like $(\gamma(t_0 - t)^2/\rho)^{1/3}$ (t_0 corresponding to the instant of the singular collapse) [59]. In the three cases presented here, the same self-similar collapse is clearly at play, as shown on Figure 2.7(d,e) where the different cavity profiles plotted at different times before t_0 collapse when lengths are divided by $(t_0 - t)^{2/3}$. Consequently, we observe a capillary-inertia self-similar collapse for each case, even though the jets show clear differences (see Figure 2.6 (1), (2) and (3)) and are not singular. Interestingly, shapes, timescales and overall self-similar evolution for the collapsing cavity are identical for the high viscosity cases (b) and (c) as shown in Figure 2.7 (e). The fact that jet velocity falls with increasing viscosity therefore does not depend on the details of the cavity collapse, but more likely on the large viscous stresses developing in the highly strained region at the jet root. However, these collapses are strongly different from the collapse in water (a) which is perturbed by the presence of the small capillary waves. These waves are always traveling on top of the interface and are inherent to the complex dynamics. But we observe that increasing the viscosity leads to smoothing the collapse. In particular the closest time to t_0 in water, represented by the green dashed profile, does not coalesce properly, signifying that the dynamics is no more self-similar. This results in a collapse leaving its self-similar regime sooner than in a more viscous case, when the remnant ripples are damped. By defining $\mathrm{L}_{\min}$ as the width of the small cavity when the collapse just quitted it self-similar behavior, Figure 2.7 (f) shows the variation of this effective collapsing cavity giving rise to the jet and reveals that it decreases with Morton number. This agrees with the idea of a self-similar collapse getting closer to the singularity as viscosity is increased and justifies why the jet velocity is increasing with Morton number.

[54] Duchemin et al. (2002), *Phys. Fluids*, "Jet formation in bubbles bursting at a free surface".

[57] Zeff et al. (2000), *Nature*, "Singularity dynamics in curvature collapse and jet eruption on a fluid surface".
[58] Bartolo et al. (2006), *Phys. Rev. Lett.* "Singular Jets and Bubbles in Drop Impact".

[59] Keller et al. (1983), *SIAM Journal on Applied Mathematics*, "Surface Tension Driven Flows".

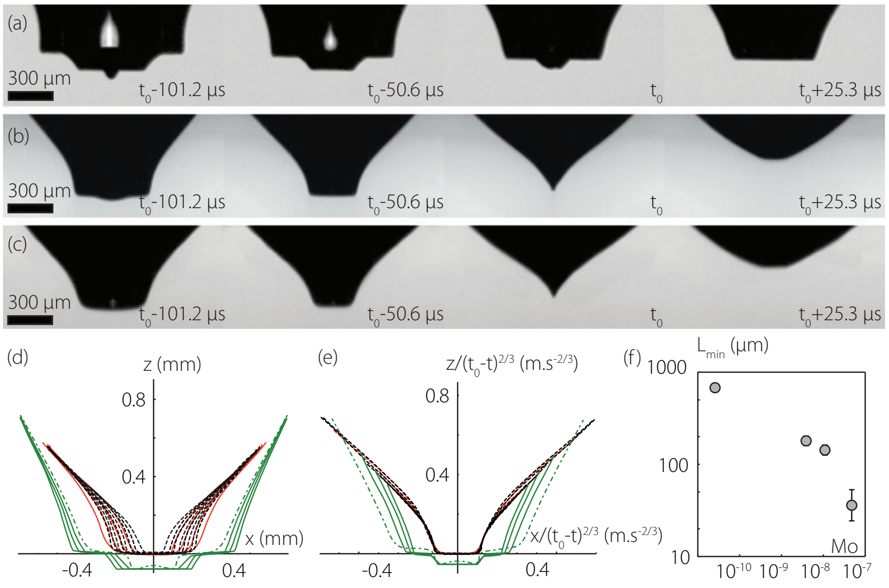

Figure 2.7: Snapshots of the final stage of the cavity collapse before the jet develops. (a), (b) and (c) correspond respectively to the jets (1), (2) and (3) of Figure 2.6. t_0 identifies the time of the wave collapse giving rise to the jet. The cavity profiles corresponding to the three sequences are plotted at different times on (d) (green for sequence (a), black for (b) and red for (c)). (e) shows the collapse of these profiles according to the capillary-inertia self-similar behavior where lengths scale with $(t_0 - t)^{2/3}$. (f) $\mathrm{L_{min}}$ versus Morton number. $\mathrm{L_{min}}$ defines the width of the small left cavity when the collapse just quitted it self-similar behavior. The size of this effective cavity giving rise to the jet eruption decreases with viscosity for $\mu \lesssim 6$ mPa.s.

Finally, two regimes of the jet dynamics as a function of the Morton number have been pointed out: for Mo $\lesssim 3.10^{-8}$ the viscosity promotes the jet velocity by smoothing the collapsing cavity and for Mo $\gtrsim 3.10^{-8}$ the jet velocity decreases with viscosity. At the frontier of these two regimes the jet is very thin and its velocity is maximal.

Toward a coupled experimental-numerical study

Morton and Laplace numbers with experimental results

At this point it is clear that both viscosity and gravity control the jet velocity. However it is impossible to really untangle the respective role of each of these two effects using the couple of dimensionless numbers Bond and Morton, as both effects are included in the Morton number. As we saw before, we used the Morton number because it is convenient from an experimental point of view, but in order to consider viscosity, separately from gravity effects, Laplace number (La) should be used, instead of Morton number. Indeed, Laplace number compares capillaro-inertia and viscosity, and does not contain gravity (the definitions are reminded in the margin). Note that another consequence of using Mo and mixing gravity and viscosity in the same number is that if the gravity, g, goes to zero, the effect of viscosity disappears, which is wrong: a bubble bursting at an interface in space would be influenced by the liquid viscosity.

$$\mathrm{Mo} = \frac{g\mu^4}{\rho\gamma^3}$$

$$\mathrm{La} = \frac{\rho\gamma R_b}{\mu^2}$$

$$\mathrm{Mo} = \mathrm{BoLa}^{-2}$$

Actually, one of the first physical study of the jet dynamics produced by bubble bursting has been realized numerically by neglecting the effect of gravity [54]. In this context only two dimensionless numbers fully describe the system. Duchemin *et al.* used the Laplace number (La) as a control parameter and they measured the capillary number which represents the jet velocity non-dimensionalized by the visco-capillary velocity (γ/μ):

[54] Duchemin et al. (2002), *Phys. Fluids*, "Jet formation in bubbles bursting at a free surface".

$$Ca = \frac{V_{\text{jet}}\mu}{\gamma}$$

Figure 2.8 (a) presents the results of Duchemin *et al.* [54] with black crosses, for which the Bond number is null, along with our experimental results for which the symbols represents the Morton number (see legend) and the color the Bond number (see color scale). From right to left, as the Laplace number decreases, the effect of viscosity becomes more important and, as we saw previously, the jet velocity increases. This behavior is recovered for any value of the Bond number. After a maximum is reached, the jet capillary number decreases. We observe that without gravity (Bo=0), the maximum occurs for an optimum Laplace number of order thousand. It corresponds to the near singular collapse described previously. Experimentally this regime is only approached for the viscous liquids. With this representation, it is now clear that the primary control on the jet velocity is the viscosity, the effect of the Bond number remaining smaller than the effect of Laplace number. The primary influence of the Bond number (i.e. gravity) is thus a downward shift of a master distribution. But it is not the only influence, indeed, we can distinguish that as the Bond number increases, the optimum Laplace number, for which the maximum jet velocity is reached, is shifted to larger Laplace number. It is not easy to observe on this graph as, here, both the Bond and the Laplace are varied simultaneously through the Morton number.

Now we want to change the Laplace and the Bond numbers independently. But this is impossible to do experimentally. Moreover, for a given liquid (Morton number), with our experiment we were not able to produce bubbles smaller than 200 microns diameter, although they exist in the ocean for example. These arguments pushed us into carrying out a numerical study to support and extend our experimental results.

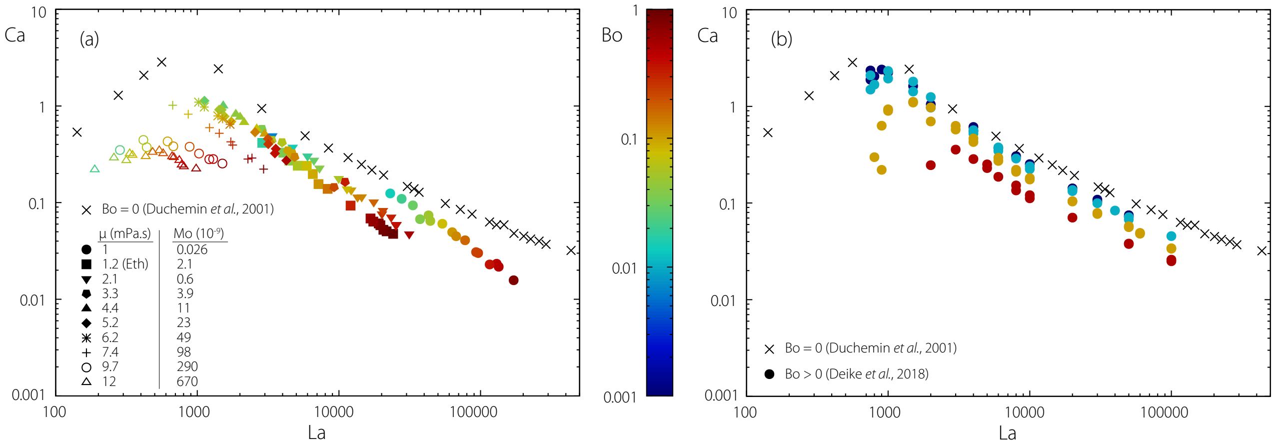

Figure 2.8: (a) Jet capillary number Ca as a function of the Laplace number La, for: (a) the data set of Duchemin *et al.* [54] (black crosses) for which the Bond number is equal to 0, and the 10 Morton numbers used experimentally. The corresponding value of viscosity is shown in the legend and the value of Morton numbers appears in Figure 2.6(b). The value of the Bond number for the experimental data is color-coded using the color scale bar in the middle. (b) $Bo = 0$ from Duchemin *et al.* with black crosses and four different Bond numbers computed numerically: $Bo = 0.001$ in dark blue, $Bo = 0.01$ in light blue, $Bo = 0.1$ in yellow and $Bo = 0.5$ in red. The Bond number is color-coded using the same scale as in (a).

Numerical results

I would be unable to go into the numerical details, they are in the corresponding paper [18], but note that some care needs to be taken in the definition of the ejection speed in order to obtain meaningful comparisons. Numerically, we measure the jet velocity from the jet birth and we observe that, after a transient regime it reaches a plateau value. This is the value we take for the jet velocity V_{jet}. We will see later that this value is the same as the first drop velocity.

[18] Deike et al. (2018), *Physical Review Fluids*, "Dynamics of jets produced by bursting bubbles".

Figure 2.8 (b) shows the Capillary number versus Laplace number for five different Bond numbers: Bo $\in [0-0.5]$. For the sake of clarity the experimental data on Figure (a) are not plotted on this figure, but the agreement between numerical and experimental results is perfect, validating the numerical method (see [18] for details). This result is important as it paves the way for further investigation with this powerful tool.

Moreover, we observe on this curve that the Bo > 0 curves really recover the shape of Bo $= 0$ curve, but with two mains influences of the gravity. First, as we saw on the Figure (a), at a given Laplace number, the velocity slightly decreases with increasing Bond number. Second, the optimal Laplace number, for which the highest velocity is observed, stays constant for Bo < 0.1 and increases with the Bond number for Bo > 0.1. The maximum capillary jet velocity decreases as the Bond number increases.

2.4 Drops velocity

Considering the excellent results we obtain numerically, we decided to go further and use it to progress on the drops velocity characterization.

This section is mainly extracted from: [20] Berny et al. (2020), *Phys. Rev. Fluids*, "Role of all jet drops in mass transfer from bursting bubbles".

Top drop velocity

We consider in this subsection the velocity of the first ejected drop, *e.g.* pink drop on the Figure 2.9, measured just after its formation, V_{d_1} and we define a new capillary number based on this velocity:

$$\mathrm{Ca}_{d_1} = \frac{V_{d_1}\mu}{\gamma}$$

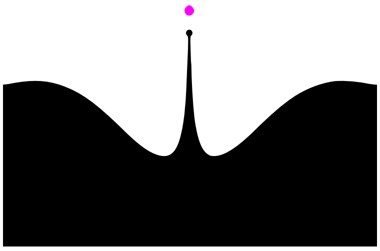

Figure 2.9: Axisymmetric profile of the jet and droplets. The pink droplet is the first ejected.

Figure 2.10 presents both this first droplet dimensionless velocity Ca_{d_1} obtained with Basilisk (filled diamonds) and data of jet velocity Ca from Figure 2.8(b) [18] obtained with Gerris (empty triangles), as a function of Laplace and for different Bond numbers between 0.94×10^{-3} and 1. Note that, as we said before, the data from Deike *et al.* were already validated against experimental data from Ghabache *et al.* [17]. We obtain a good agreement between the two data sets for the whole range of Laplace and Bond numbers. This has two consequences: first of all, it validates the new numerical setup, as well as the algorithms in Basilisk ; second of all, it shows that the jet velocity on its plateau value used in Deike *et al.* [18] is the same as the drop velocity. The discussion of Figure 2.8 applies then to the drop velocity. In particular, a maximum in ejection speed of around three times the visco-capillary velocity is also obtained for a Laplace number around 1000 at low Bond numbers. At higher Bond numbers this maximum decreases and the value of the corresponding optimal Laplace number increases.

Gañàn-Calvo [60] proposed a scaling law for the velocity of the first drop based on a balance of the momentum equation terms during curvature reversal, which leads to the black curve in Figure 2.10 (a), given by:

[60] Gañán-Calvo (2017), *Physical review letters*, "Revision of bubble bursting: universal scaling laws of top jet drop size and speed".

$$\mathrm{Ca} = k_v \left(\mathrm{La}\left(\mathrm{La}_\star^{-1/2} - \mathrm{La}^{-1/2}\right)\right)^{-3/4} \tag{2.7}$$

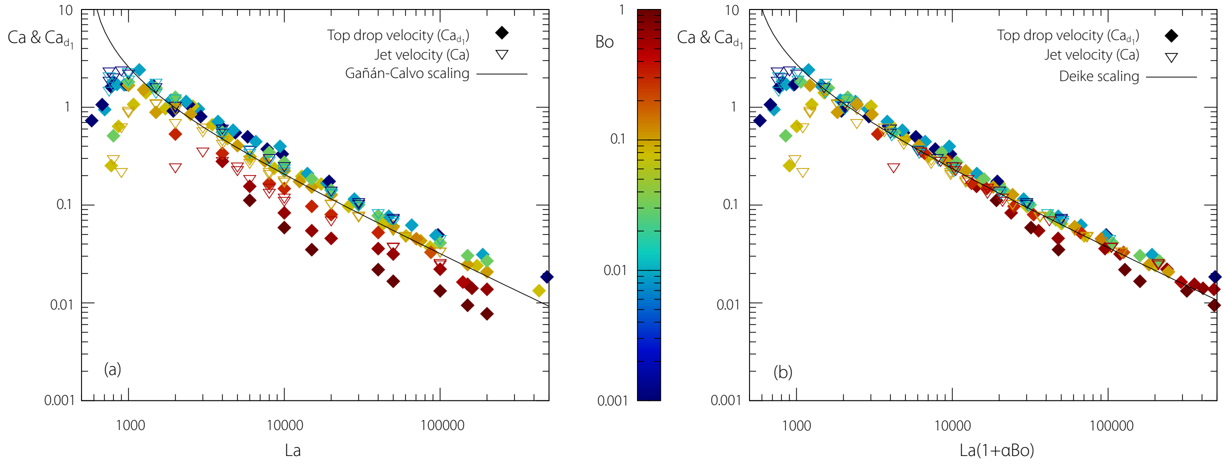

Figure 2.10: (a) Dimensionless velocity of the jet (Ca, open triangles) and of top drop (Ca_{d_1}, plain diamonds) as a function of the Laplace number La. The color scale indicates the Bond number of the simulation as shown on the color scale bar in the middle. The black line represents the scaling law proposed by Gañàn-Calvo under the no-gravity assumption [60]. (b) Rescaled data set using the empirical relation proposed by Deike *et al.* [18]. The black line represents the scaling law proposed by Deike *et al.* [18] and adapted from Gañàn-Calvo [60].

where $\mathrm{La}_\star \simeq 500$ is the critical value of the Laplace number below which no droplet is produced, and $k_v \simeq 16$ is a nondimensional coefficient fitted to the data. Note that gravity is not taken into account in this scaling ($\mathrm{Bo} = 0$).

The slight effect of gravity is taken into account empirically in the rescaling of the x-axis proposed in Figure 2.10 (b), which can be written

$$\mathrm{Ca} = k_{v\mathrm{Deike}}\,(1+\alpha\mathrm{Bo})^{-3/4}\,\mathrm{La}^{-3/4}\left(\mathrm{La}_*^{-1/2} - \mathrm{La}^{-1/2}\right)^{-3/4} \qquad (2.8)$$

where α is a nondimensional coefficient. We fitted $\alpha = 2.2$ and $k_{v\mathrm{Deike}} = 19$ to the data to obtain the rescaling in Figure 2.10 (b). The rescaling seems to work reasonably well. Note that Ref. [61] discusses another scaling that accounts for the effect of the gravity and appears fully compatible with the present empirical formula.

[61] Gañán-Calvo (2018), *Phys. Rev. Fluids*, "Scaling laws of top jet drop size and speed from bubble bursting including gravity and inviscid limit".

Velocity of all drops

Figure 2.11 presents a numerical snapshot of a jet with 5 drops ejected, all with a different color. Within our range of control parameters, between $i = 0$ and 17 droplets are ejected when a bubble bursts. Using the same simulations as just presented we can characterize all the droplets produced by a bursting bubble.

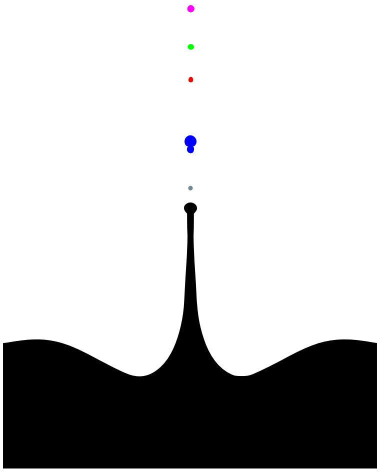

Figure 2.11: Axisymmetric profile of the same jet as in Figure 2.9. All ejected drops have a different color.

We focus here on the ejection velocity of the three droplets following the first one, namely Ca_{d_i} with $i = 2$ to 4, shown in Figure 2.12 as functions of the bubble Laplace and Bond numbers. The scaling relation of Gañàn-Calvo[60], Equation 2.7, describing the velocity of the first droplet ($i = 1$) at small Bond numbers is indicated for comparison in each panel. The dimensionless velocity of all droplets follow a trend similar to that of the first droplet. It is slightly slower and with an increasing scatter as the droplet number i is increased. This result was not really expected, we would have expected higher difference as i is increased. Increasing the Bond number also tends to decrease the velocity of the droplets, and even suppress the creation of droplets entirely

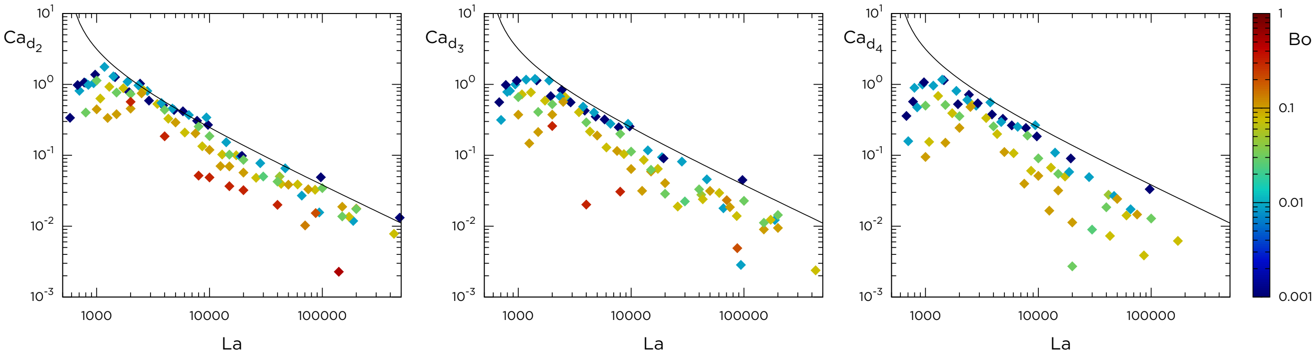

Figure 2.12: (Left column) Dimensionless velocity, Ca_{d_i}, of droplets number $i = 2$ to 5 (top to bottom) as functions of the Laplace and Bond numbers (color-coded). The solid line reproduces the scaling relation of [60] for the first droplet, under the vanishing Bond number assumption. (Right column) Ratio of the dimensionless velocity of droplets number $i = 2$ to 5 (top to bottom) to the velocity of the first droplet Ca_{d_1}.

for large enough values, and even more as i increases, which explains the absence of red symbols on Ca_{d_4} plot.

Note that in addition to provide the first comprehensive data set of the bubble bursting drop velocity dynamics, we will see that this exhaustive drop velocity characterization will feed a drop evaporation model presented in Section 2.6.

2.5 End pinching and drops size

After the drop dynamics, this section focuses now on the size of the *jet drops* produced by bubble bursting as a function of the liquid properties and the mother bubble size [62] (Figure 2.13). Our experimental work will first allow us to determine relevant scaling laws for the top drop diameter, to discuss their regime of existence, and to interpret the mechanisms at play. Then, numerical study will provide exhaustive data on the whole range of control parameters, will allow us to precise the relevant scaling law for the top drop size and will enable characterization of all droplets size.

This section is mainly extracted from: [19] Ghabache & Séon (2016), *Phys. Rev. Fluids*, "Size of the top jet drop produced by bubble bursting".

[62] Spiel (1994), *J. Geophys. Res.* "The number and size of jet drops produced by air bubbles bursting on a fresh water surface".

The end-pinching mechanism

An infinite cylinder of liquid at rest, subjected to the influence of surface tension, will break up into a number of individual droplets through the so-called Rayleigh-Plateau instability. The bubble bursting jets, depicted in Figure 2.13, are finite and do not break as a consequence of Rayleigh-Plateau instability. Instead, the breakup takes place at the jet tip and detaches one drop at a time. This mechanism, called *end-pinching*, consists of a competition between the capillary retraction of the jet tip, shaping a blob [63], and a pressure-driven flow from the cylindrical jet toward the bulbous end. This leads to the development of a neck, where the jet joins the blob, and thus to the drop detachment via a capillary pinch off process. This mechanism has been first described in the context of a strongly deformed viscous drop [64] and later for a free liquid filament of arbitrary viscosity [65]. This end-pinching capillary breakup of liquid jets is important in several industrial contexts, especially because of the broad range of applications of inkjet printing technology. Indeed, it enables accurate drop deposition of liquids, and includes production of organic thin-film transistors, Liquid Crystal Displays (LCD), fuel or solar cells,

[63] Keller et al. (1995), *Physics of Fluids*, "Blob formation".

[64] Stone et al. (1989), *Journal of Fluid Mechanics*, "Relaxation and breakup of an initially extended drop in an otherwise quiescent fluid".

[65] Castrejón-Pita et al. (2012), *Physical review letters*, "Breakup of liquid filaments".

Printed Circuit Boards (PCB), dispensing of DNA and protein substances, or even fabrication of living tissue [66].

[66] Singh et al. (2010), *Advanced materials*, "Inkjet printing—process and its applications".

Top jet drop size variation

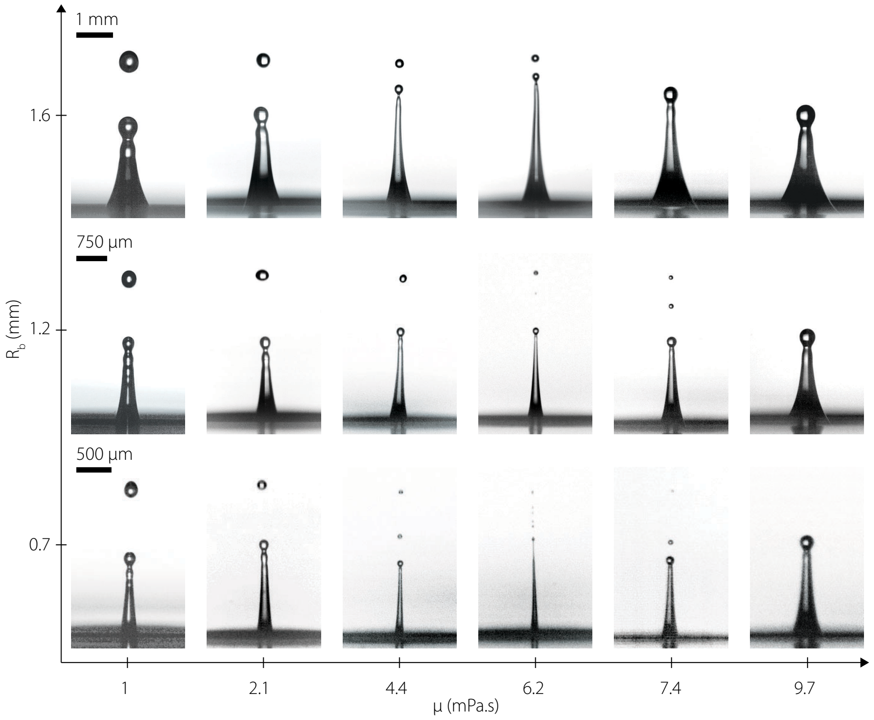

Figure 2.13: Snapshot of a typical jetting event following a bubble bursting at a free surface. The jets and drops shape is displayed for three mother bubble radii, reported on the y-axis, bursting in water and five water-glycerol mixtures of viscosity indicated on the x-axis. For those six solutions, the surface tension is almost constant (ranging from 64 to 72 mN.m^{-1}) so that one mainly observes in this figure the effect of changing viscosity. Top drop size decreases with bubble radius and increasing liquid viscosity. The biggest drop, on the top left corner of this diagram, is about 400 μm radius and the smallest ($R_b = 0.7$ mm and $\mu = 7.4$ mPa.s) reached 20 μm. The scale bar is showed on the top left corner of each bubble radius and is the same the whole row.

Figure 2.13 presents the jet and released drop shape following bubble bursting. In the cases where no drop detaches the jets are displayed at their maximum height. On the x and y-axis the jets and top drops shape is represented, respectively, for six different liquid viscosities and three different mother bubble radii. It is clear on this diagram that, independently of the viscosity, the bigger the bubble the bigger the top drop. This intuitive result has been observed in water in various previous studies [62]. The variation of drop size with viscosity has been qualitatively seen in the previous section (see snapshots of Figure 2.6 (b)). Irrespectively of the bubble radius in the range considered here, the top drop shrinks as viscosity is increased, and seems to reach a minimum for a liquid viscosity around 6-7 mPa.s here. For higher viscosities, no drop is detached, in accordance with previous study [67]. Even if already observed, this decrease of the drop radius with viscosity is surprising, in particular because the Laplace number based on the drop radius, namely $\mathrm{La}_d = \rho\gamma R_d/\mu^2$, which compares the effect of capillarity and viscosity, is included between 100 and 10^6 and is consequently always higher than 1. This therefore suggests that viscous effects should be neglected in the description of jet breakup, as done in similar cases [68]. We will see further down why, in this particular case of bubble bursting jet, the liquid viscosity has such a strong influence.

[62] Spiel (1994), *J. Geophys. Res.* "The number and size of jet drops produced by air bubbles bursting on a fresh water surface".

[67] Walls et al. (2015), *Phys. Rev. E*, "Jet drops from bursting bubbles: How gravity and viscosity couple to inhibit droplet production".

$$\mathrm{La}_d = \frac{\rho\gamma R_d}{\mu^2}$$

[68] Gordillo et al. (2010), *J. Fluid Mech.* "Generation and breakup of Worthington jets after cavity collapse. Part 2. Tip breakup of stretched jets".

Top jet drop radius and bubble bursting

We start by ploting, in Figure 2.14 (a), the experimental variation of the top drop radius R_d as a function of the mother bubble radius R_b for different

	●	◀	●	▲	◇	✡	▷	◆	▼	■
γ (mN/m)	72	67	65	65	65	64	64	48	48	48
μ (mPa.s)	1.0	2.1	3.3	4.4	5.2	6.2	7.4	1.6	2.6	3.6

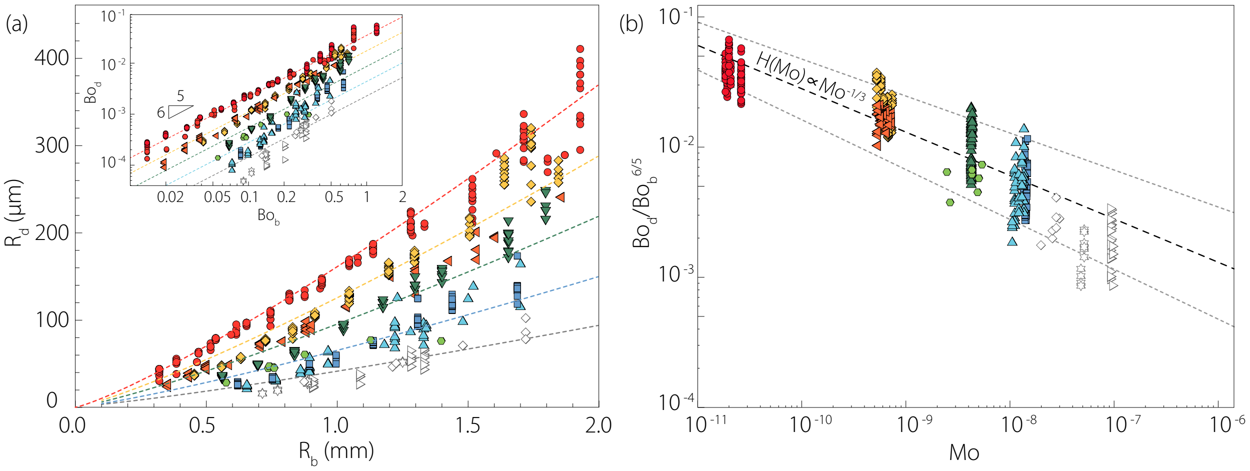

Figure 2.14: (a) Top drop radius as a function of the mother bubble radius for bubble bursting in liquids with different surface tension and viscosity. The parameters of these liquids associated to the corresponding symboles are summarized in the table above the graph. In the inset, the Bond number built on the drop radius is plotted as a function of the Bond number built on the bubble radius for the same liquids. The dashed lines represent $R_d \propto R_b^{6/5}$ in the graph and $Bo_d \propto Bo_b^{6/5}$ in the inset. (b) $\mathrm{Bo}_d/\mathrm{Bo}_b^{6/5}$ as a function of the Morton number. The dashed line fits the experimental data plotted with closed symbols, up to $\mathrm{Mo} \sim 10^{-8}$, following the trend $\mathrm{Bo}_d/\mathrm{Bo}_b^{6/5} \propto \mathrm{Mo}^{-1/3}$. The error bar on the exponent is 1/20, and the two bounds $\mathrm{H(Mo)} \propto \mathrm{Mo}^{-1/3\pm1/20}$ are plotted on the graph with dotted line.

values of the liquid parameters (μ, γ and ρ) indicated in the table above. This quantifies our previous observation of drop shrinking with decreasing bubble radius and increasing liquid viscosity, from 400 μm to 20 μm for the solutions plotted here. We also observe that the same drop shrinking occurs when surface tension is decreased. Moreover, it appears that, regardless of the liquid parameters considered in this graph, the drop size increases with bubble radius following roughly the same variation for all the curves: $R_d \propto R_b^{6/5}$, shown with dashed lines on the graph. Note that when $R_b \geq 0.1$ mm, the relationship $R_d = 0.075 R_b^{1.3}$ has been proposed in Ref. [69], with radii expressed in millimeters. This variation is very closed to the one we find.

[69] Massel (2007), , "Ocean Waves Breaking and Marine Aerosol Fluxes".

We can build a Bond number based on the drop diameter:

$$\mathrm{Bo}_d = \rho g R_d^2/\gamma$$

In order to fully describing the top drop size selection, a relation between this dimensionless number and two others among those introduced in Section 2.2 has to be found. For the convenience reasons related to experimental work, we are looking for a relation under the form $\mathrm{Bo}_d = F(\mathrm{Bo}_b, \mathrm{Mo})$. The dimensionless numbers being reminded in the margin. On the inset of Figure 2.14 (a) the variation of the top drop Bond number is plotted as a function of the mother bubble Bond number for the same solutions. The variation $\mathrm{Bo}_d \propto \mathrm{Bo}_b^{6/5}$ is also plotted with dashed lines. This power law, independent of the liquid parameters, still works reasonably well, allowing us to write the following scaling law:

$$\mathrm{Bo}_d = \frac{\rho g R_d^2}{\gamma}$$

$$\mathrm{Bo}_b = \frac{\rho g R_b^2}{\gamma}$$

$$\mathrm{Mo} = \frac{g\mu^4}{\rho\gamma^3}$$

$$\mathrm{Bo}_d = \mathrm{Bo}_b^{6/5} H(\mathrm{Mo}). \tag{2.9}$$

With the aim of estimating the dependance of the drop size with the liquid properties, namely H(Mo), $\mathrm{Bo}_d/\mathrm{Bo}_b^{6/5}$ is plotted as a function of the Morton number on Figure 2.14 (b). We observe that the data with closed symbols gather along a line, up to $\mathrm{Mo} \simeq 10^{-8}$, corresponding to a viscosity $\mu =$

5.2 mPa.s for a water-glycerol mixture. This line is properly fitted by H(Mo) $= \mathcal{A}\ \mathrm{Mo}^{-1/3}$ with $\mathcal{A} = 1.1\ 10^{-5}$. As the results are slightly scattered we estimate the error bar by fitting the lower and upper bounds and we find $\mathrm{H(Mo)} \propto \mathrm{Mo}^{-1/3\pm1/20}$, these two bounds are plotted on the graph with dotted line. Therefore, in this regime, ranging on around three decades in Morton number, we established a scaling law for the top drop size as a function of the bubble radius and liquid parameters, in the context of bubble bursting:

$$\mathrm{Bo}_d \propto \mathrm{Bo}_b^{6/5} \mathrm{Mo}^{-1/3}. \tag{2.10}$$

This result is interesting because the bubble radius and the liquid parameters are the natural experimental parameters for bursting bubble aerosol measurement. However, under this form, Equation 2.10 is delicate to interpret, in particular, the confusing role of viscosity, that is expected to be negligible (La $\gg$ 1). In addition, this scaling law contains substantial experimental data scattering due to an accumulation of variability, when the jet is created and when the drop is detached. In the following, we wish therefore to improve this scaling law. First, we start by expressing the drop radius as a function of only jet parameters, typically by disposing of the bubble radius. Second, we use numerical simulation to extend the range of the control parameters and plot the drop radius in another dimensionless numbers space.

Top jet drop radius and jet dynamics

When a bubble collapses, a jet is formed with a given shape, tip velocity, local strain rate, etc. In this regime, where Mo $\lesssim 10^{-8}$, the decrease of the drop size with Morton number comes along with a thinning down of the whole jet and an increase of the jet velocity. This has been largely discussed in Section 2.3 and the corresponding scaling law, for the jet velocity as a function of the bubble radius and liquid parameters, has been proposed: $\mathrm{We}_b = \mathrm{Bo}_b^{-1/2} f(\mathrm{Mo})$. Therefore, with the aim of decoupling the effects of bubble collapse and jet dynamics on the drop detachment, this scaling can be combined with Equation 2.10 in order to eliminate the bubble radius. This eventually yields the following scaling law relating the drop radius, the jet velocity and the liquid parameters:

$\mathrm{We}_b = \dfrac{\rho V_{\mathrm{jet}}^2 R_b}{\gamma}$

$$\mathrm{Bo}_d = (\mathrm{Fr}_d \mathrm{We}_d)^{-3/5}\, G(\mathrm{Mo}) \tag{2.11}$$

where $\mathrm{Fr}_d = V_{\mathrm{jet}}^2/gR_d$, leading to $\mathrm{Fr}_d\mathrm{We}_d = \rho V_{\mathrm{jet}}^4/\gamma g$ which compares the effect of inertia upon capillarity and gravity on the jet dynamics, and is, in particular, independent of bubble radius and viscosity.

$\mathrm{Fr}_d\mathrm{We}_d = \dfrac{\rho V_{\mathrm{jet}}^4}{\gamma g}$

In the Figure 2.15 the drop Bond number Bo_d is plotted as a function of $\mathrm{Fr}_d\mathrm{We}_d$ and we observe an excellent collapse of all the experimental data represented with closed symbols (Mo $\lesssim 10^{-8}$) leading to:

$$\mathrm{Bo}_d \propto (\mathrm{Fr}_d \mathrm{We}_d)^{-3/5} \tag{2.12}$$

The fonction G(Mo) appears to be a constant, viscosity is removed from the scaling law relating the drop radius, the jet velocity and the liquid parameters. The insert Figure 2.15 presents $\mathrm{Bo}_d/\left(\mathrm{Fr}_d\mathrm{We}_d\right)^{-3/5}$ as a function of Morton number and confirms that the drop Bond number is independent of viscosity for the closed symbols. This inviscid behaviour stops at Mo $\simeq 10^{-8}$, viscosity playing a role for open symbols, between 10^{-8} and 10^{-7} (corresponding to

$\mu \sim 5$ and 7 mPa.s for water glycerol mixtures). Above $\mathrm{Mo} \simeq 10^{-7}$ no more drop can detach.

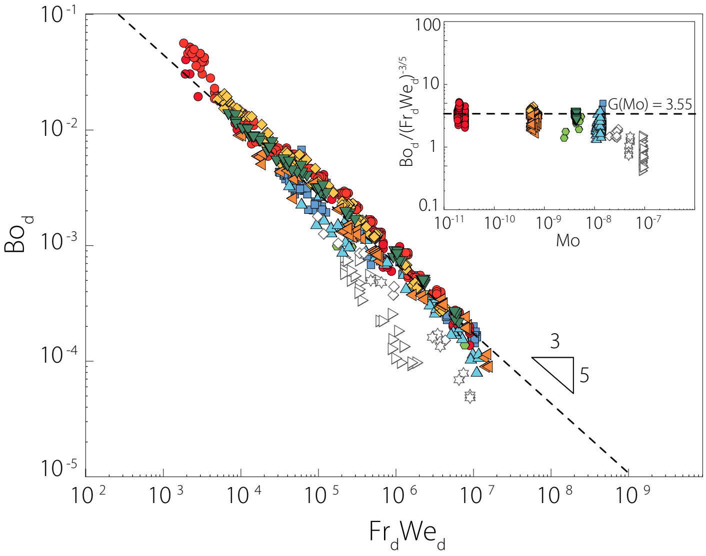

Figure 2.15: Drop Bond number as a function of the product of Froud and Weber number $\mathrm{Fr}_d\mathrm{We}_d = \rho V_{\text{jet}}^4/\gamma g$ for various values of the Morton number. For $\mathrm{Mo} \lesssim 10^{-8}$, all the data, plotted with closed symbols, collapse on a single curve following the trend $\mathrm{Bo}_d \propto (\mathrm{Fr}_d\mathrm{We}_d)^{-3/5}$ as shown by the dashed line. In the inset, $\mathrm{Bo}_d/\left(\mathrm{Fr}_d\mathrm{We}_d\right)^{-3/5}$ is plotted as a function of Mo. The dashed line fitting the data on the same range is a constant, equals to 3.55. Data corresponding to $\mathrm{Mo} \in [10^{-8}, 10^{-7}]$ plotted with open symbols leave the inviscid regime. Above $\mathrm{Mo} \simeq 10^{-7}$ no more drop can detach.

Equation 2.12, valid for $\mathrm{Mo} \lesssim 10^{-8}$, is therefore more robust, with less scattering than Equation 2.10. Furthermore, it demonstrates that viscosity does not participate to the drop detachment process. This result was predictable as the Laplace number is always higher than one. However, we may now wonder why the drop radius was dependent on the liquid viscosity in Figure 2.13, Figure 2.14 and Equation 2.10. Actually, this influence of viscosity on drop size was only through the jet's formation as a memory of the bubble collapse, as we discussed in Section 2.3. Increasing the liquid viscosity changes the wave focusing, producing a thinner jet and therefore smaller droplets. In Equation 2.12, this shaping effect is then entirely contained through V_{jet} and viscosity can disappear, shedding light on the inviscid behavior of the drop detachment mechanism. Finally, the Bond number of the drop seems to be only selected by a competition between the given inertia, which makes the jet rising and stretching, and the duet gravity-capillarity which pulls on the jet tip so as to form a blob, initiating an end-pinching mechanism and consequently releasing a drop. While the influence of capillarity is obvious in this blob formation, the one of gravity can be more surprising. By expressing the drop radius R_d as a function of the control parameters we observe that the influence of gravity is weak ($\mathrm{R}_d \propto g^{-1/5}$) and, at the height the drop is detached, the gravity might play a role. Indeed, the Froude number built on the drop detachment height h_{det}, $\mathrm{Fr}(h_{\text{det}}) = V_{\text{jet}}^2/gh_{\text{det}}$, equals to $\mathrm{O}(1)$ for top drops projected by the largest bubbles. Anyway, the influence of gravity reminds mysterious, the next section brings more insights on its influence.

New scaling law for the top jet drop radius

Equation 2.12 provides an elegant scaling for the top drop size that works reasonably and brings interesting interpretation. But everything is not satisfying. By disposing of the bubble radius, this scaling hides a crucial control parameter. Moreover, none of the rescaling we have proposed exhibited the singularity we observed on the drop velocity. Consequently, we are looking for a new scaling law based on the same experimental data. As discussed in previous section, we assume that gravity is not crucial and can be only considered as a correction, viscosity being the main parameter. Thus, the drop radius R_d is now nondimensionalized with capillarity and viscosity so as to form the Laplace number of the drop:

$$\mathrm{La}_d = \frac{\rho \gamma R_d}{\mu^2}$$

The dimensionless control parameters becoming the Laplace number based on the bubble radius, La, instead of the Morton number and the Bond number. The system is now described by a relation of the form: $\mathrm{La}_d = \Pi(\mathrm{La}, \mathrm{Bo})$. With this set of dimensionless numbers, the gravity is only included in the Bond number, and Laplace number reflects the effect of viscosity.

$$\mathrm{La} = \frac{\rho \gamma R_b}{\mu^2}$$

$$\mathrm{Bo} = \frac{\rho g R_b^2}{\gamma}$$

Figure 2.16 (a) presents the same experimental data as presented in the previous section but plotted with this new nondimensionalization: La_d versus La for various bubble Bond numbers Bo. The viscosity, surface tension and the corresponding Morton number are indicated in the legend. The bubble Bond number is color-coded using the color scale bar. We observe an excellent rescaling of all data along a unique curve, even the viscous data that did not properly rescaled in the previous scaling laws ($\mu = 5.2, 6.2, 7.4$ mPa.s). This rescaling signifies that there is no influence of the bubble Bond number. In other words, this nondimensionalization strongly suggests that the drop radius is selected independently of gravity. In the scaling of Equation 2.10 the dependence with gravity was actually very weak ($R_d \propto g^{-1/15}$), but the choice of introducing the Bond number draw attention on gravity and was probably not appropriate. Another consequence of this new nondimensionalization is the degenerescence from 3 to 2 dimensionless numbers describing the process of drop size selection as function of bubble size and liquid parameter. Moreover, in accordance with what has been previously observed and discussed, we retrieve the drop shrinking induced by the increase of viscosity. This drop reduction is interpreted the same way we interpreted the increase of the jet velocity: getting closer to the singularity accelerates and slims the jet. However, by analogy with Figure 2.10 we expect to reach a change of behavior at the singularity, around $\mathrm{La} \sim 1000$. Unfortunately, the experimental data are

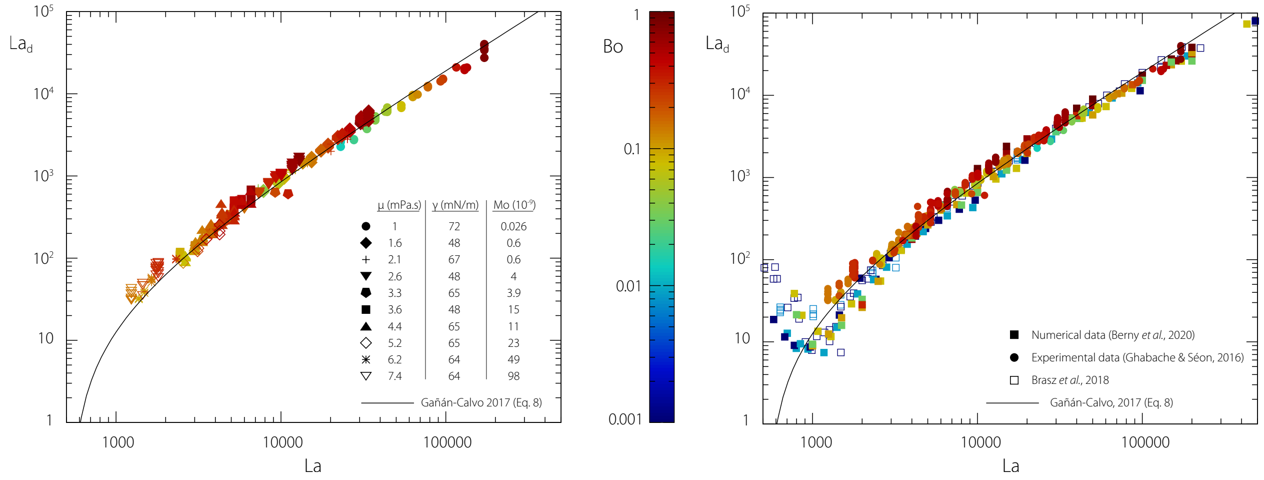

Figure 2.16: Droplet Laplace number $\mathrm{La_d}$ as a function of the bubble Laplace number La, with Bo color-coded for (a) our experimental data [19] and (b) the same experimental data, our numerical data [20] and the experimental and numerical data from Brasz *et al.* [70]. In (a) the different symbols represent the different Morton numbers and in (b) the symbols are related to the study. The symbols are specified in the legend. The black curve is the scaling law Equation 2.13 from Ref. [60], it describes well the data for $\mathrm{La} > 1000$. Note that in (b) our numerical and experimental data have slightly different way to define the bubble radius, for numerical it is on the equivalent sphere and on the experimental on the measured ellipse at the bottom of the cavity. This difference induces slight discrepancy between the two series, and has been corrected in the ref [20].

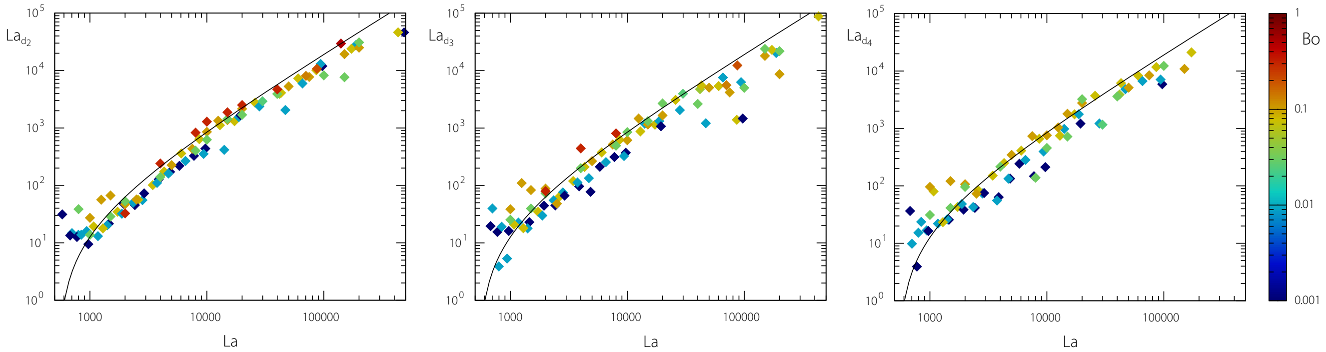

Figure 2.17: Sizes of the droplets $i = 2$ to 4 (top to bottom), La_{d_i} as functions of the bubble Laplace number, La, and Bond number (color-coded). The black line is the scaling relation of Equation 2.13 for the size of the first droplet, from [60].

here lacking, we would need to produce smaller bubbles but do not have the adequate experimental setup. To go further we chose to go back to numerical simulation.

In Figure 2.16 (b) our numerical data are superimposed to our experimental data and to the numerical and experimental data of Brasz *et al.* [70]. The match between all the studies is excellent, for the full range of Laplace and Bond numbers, validating once more our numerical setup. Furthermore, the numerical simulations enable to reach the singularity. The evolution with Laplace number mirrors that of the droplet velocity, with a minimum obtained for the optimal Laplace number around 1000. Finally, all experimental and numerical data sets are remarkably consistent with the following scaling proposed by Gañàn-Calvo [60]:

[70] Brasz et al. (2018), *Physical Review Fluids*, "Minimum size for the top jet drop from a bursting bubble".

$$\mathrm{La}_{\mathrm{d}_1} = k_r \left(\sqrt{\mathrm{La}} \left(\sqrt{\frac{\mathrm{La}}{\mathrm{La}_*}} - 1 \right) \right)^{5/4} \tag{2.13}$$

[60] Gañán-Calvo (2017), *Physical review letters*, "Revision of bubble bursting: universal scaling laws of top jet drop size and speed".

where k_r is a nondimensional coefficient fitted to the data. This relationship described the data extremely well for Laplace numbers greater than the optimal value (1000), while not capturing the behavior below La=1000.

All jet drops size

Now that we are convinced our code is valid on our range of control parameter, we use it to propose a comprehensive study that characterize the size of all droplets produced during bubble bursting. Figure 2.17 presents the nondimensionalized size of the drops $n = 2$ to 4, expressed as a droplet Laplace number, La_d, as a function of the bubble Laplace number La, for the whole range of Bond numbers (color-coded). The scaling relation of Gañàn-Calvo [60], (Equation 2.13), that describes the size of the first droplet ($n = 1$) for any Bond number (Figure 2.16) is given for comparison. The general trends are similar to those for the droplet velocities: an overall dependency on the Laplace number matching that for the first droplet, increasing scatter as the droplet index is increased and a slight increase in droplet size with increasing Bond number. As for velocity, a statistical study of the size fluctuations would be necessary to properly quantify the variance. Note that close to the optimal Laplace number (La $\approx$ 1000), subsequent droplets are significantly larger than the first droplet, which suggests that the finite-time curvature singularity approached by the collapsing bubble no longer influences the drop size selection process. Finally, in addition to provide this exhaustive drop size characterization, we will now see how this feeds a drop evaporation model.

2.6 Drops evaporation

Driven by the knowledge we have gained in the study of jet and drop detachment dynamics, we now aim at estimating droplet evaporation and finding how liquid properties and bubble radius would tune the aerosol evaporation. This last section will be divided into two parts : first we define an evaporation model and we validate it experimentally ; second we use the drops size and velocity given by the numerical simulation to feed the model and estimate the mass transfert induced by jet drops as a function of the control parameters.

This section is mainly extracted from:
[22] Ghabache et al. (2016), *Scientific Reports*, "Evaporation of droplets in a Champagne wine aerosol".
[20] Berny et al. (2020), *Phys. Rev. Fluids*, "Role of all jet drops in mass transfer from bursting bubbles".

Simple model for drop evaporation

Upon ejection, a droplet has an initial radius and velocity, that we now know, and during its travel the drop evaporates, and both the radius $R_d(t)$ and the velocity $\frac{\mathrm{d}z}{\mathrm{d}t}$ will vary. The trajectory is captured by integrating the following differential equation:

$$\frac{4}{3}\rho\pi R_d^3\frac{d^2z}{dt^2}(t) = -\frac{1}{2}\rho_{\text{air}}\pi R_d^2(t)\left(\frac{dz}{dt}\right)^2 C_D - \frac{4}{3}\rho\pi R_d^3(t)g \tag{2.14}$$

with z the drop height and C_D the drop drag coefficient. Here C_D is taken as the drag coefficient on a solid sphere in steady motion. As the drop Reynolds number $\mathrm{Re}(t) = 2\frac{\rho_{\text{air}}}{\mu_{\text{air}}}\frac{dz}{dt}R_d(t)$ ranges from ten to a hundred, classical Stokes' drag, 24/Re, is not adequate and inertial terms need to be added. Many empirical or semiempirical equations have been proposed [71] to approximate C_D as a function of the Reynolds number on a given Reynolds range. Here $C_D = \frac{24}{\mathrm{Re}(t)}\left(1 + 0.15\ \mathrm{Re}(t)^{0.687}\right)$, valid for $Re < 800$ [72], has been taken.

[71] Clift et al. (2005), , "Bubbles, drops, and particles".

[72] Schiller et al. (1935), *Vdi Zeitung*, "A drag coefficient correlation".

Now we need a model for the drop shrinking due to evaporation. We consider a drop with an uniform temperature T (between 4 and 20°C) that moves into an environment with temperature $T_\infty = 20$°C and mass fraction of the vapor of the droplet material $Y_{\text{vap}}^{\infty} = \frac{\rho_{\text{vap}}^{\infty}}{\rho_{\text{air}}}$. The considered model implies that quasi-steady conditions prevail. Under these conditions, and considering the thermophysical properties as constant, the analysis of mass transfer processes into the gas phase near the droplet surface allows the determination of the regression rate of the droplet radius:

$$\frac{\mathrm{d}R_d^2(t)}{\mathrm{d}t} = -2j_0\left(1 + 0.3\mathrm{Sc}^{\frac{1}{3}}\mathrm{Re}(t)^{\frac{1}{2}}\right) \tag{2.15}$$

where Sc, the Schmidt number, is defined as the ratio of momentum diffusivity in air (ν_{air}) and mass diffusivity of vapor in air (D), and j_0 the evaporation parameter [73, 74]. In our case, where the gas temperature is low, evaporation process is only controlled by diffusion, which leads to $j_0 = \frac{\rho_{\text{air}}}{\rho_{\text{liq}}}D(Y_{\text{vap}}^{\text{surf}} - Y_{\text{vap}}^{\infty})$ [75] - the Stefan flow being negligible [74]. Equation 2.15 is the product of two terms: the first term $\frac{\mathrm{d}R_d^2(t)}{\mathrm{d}t} = -2j_0$ is the well known d^2-law for a pure diffusive evaporation, without relative motion between the droplet and the surrounding air [76, 77]. The drop motion is taken into account into the second term, using the standard Ranz and Marshall empirical mass transfer correlations for moving sphere $1 + 0.3\mathrm{Sc}^{\frac{1}{3}}\mathrm{Re}(t)^{\frac{1}{2}}$ [78]. This correction comes

[73] Frohn et al. (2000), , "Dynamics of droplets".
[74] Sirignano (1999), , "Fluid dynamics and transport of droplets and sprays".

[75] Cazabat et al. (2010), *Soft Matter*, "Evaporation of macroscopic sessile droplets".

[76] Langmuir (1918), *Physical review*, "The evaporation of small spheres".
[77] Fuchs (1959), , "Evaporation and droplet growth in gaseous media".

[78] Ranz et al. (1952), *Chem. Eng. Prog*, "Evaporation from drops".

from the assumption that the mass exchange between the droplet surface and the gas may be modeled as occurring within a spherical diffusion film of constant thickness $R_d(t)/(0.3\text{Sc}^{\frac{1}{3}}\text{Re}(t)^{\frac{1}{2}})$ - this behavior goes by the names of Prandlt-Blasius-Pohlhausen (1921) [79].

We remind that our experiments are done with a mixture of water, glycerol and ethanol. For the calculation of the vapor mass fraction of each substance at the surface of the droplet $Y^{\text{surf}}_{\text{vap}}$, the heat transfer equation and the Clausius-Clapeyron equation are considered. Because the vapor pressure of the glycerol is about six orders of magnitude lower than this of water or ethanol, evaporation of glycerol has been neglected. With the intrinsic difference of volatility between water and ethanol, and an ambient partial pressure taken to 50% of vapor pressure for water (relative humidity) and 0% for ethanol, we obtain an evaporation parameter (j_0) for ethanol around five times greater than evaporation parameter for water. Expectedly, ethanol evaporates easier than water. More details on this analysis are given in the "Methods" section of Ghabache *et al.* (2016) [22].

[79] Pohlhausen (1921), *ZAMM-Journal of Applied Mathematics and Mechanics/Zeitschrift für Angewandte Mathematik und Mechanik*, "Der Wärmeaustausch zwischen festen Körpern und Flüssigkeiten mit kleiner Reibung und kleiner Wärmeleitung".

[22] Ghabache et al. (2016), *Scientific Reports*, "Evaporation of droplets in a Champagne wine aerosol".

Drop evaporation from trajectory

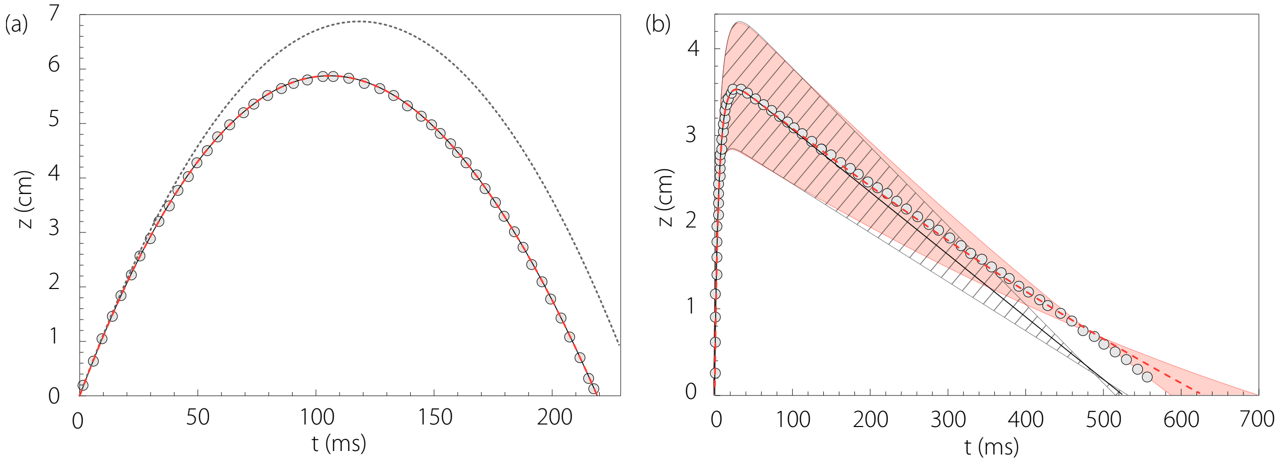

Figure 2.18: Drop height z as a function of time. The gray circles correspond to the experimental trajectory, the dashed black curve corresponds to the trajectory obtained by solving numerically Equation 2.14 (no evaporation, R_d constant) and the plain red curve corresponds to the trajectory obtained by solving numerically Equation 2.14) & Equation 2.15 (with evaporation, R_d(t) non constant). (a) Trajectories for a typical big drop: $R_d = 307$ μm and $V_d = 1.16$ m.s^{-1}. The dotted curve corresponds to the ballistic trajectory $z(t) = V_d t - \frac{1}{2}gt^2$. Here $\delta R_d(t)/R_d(0)$ reaches a final value less than 0.06% before landing. (b) Trajectories for a typical small droplet: $R_d = 24$ μm and $V_d = 8.30$ m.s^{-1}. The hatched gray and red zones represent the error in the numerical resolution of the respective models induced by the experimental error on the initial drop size measurement: $R_d = 24 \pm 3$ μm (experimental error on the initial velocity is negligible). Here $\delta R_d(t)/R_d(0)$ reaches a final value of about 20% before landing.

Now, the system of differential equations (Equation 2.14 & Equation 2.15) can be solved. The initial conditions $\dot{z}(0)$ and $R_d(0)$ are given either by the experimental or numerical measurement of the initial drop velocity and radius, *resp.* V_d and R_d. In Figure 2.18 (a), the experimental height of a first jet drop ejected is plotted with gray circles as a function of time. The considered drop is among our biggest ($R_d = 307$ μm). It follows a trajectory close to a parabola showing that the drop is big enough for the influence of the drag to be weak. The grey dotted line represents the purely ballistic parabola trajectory without drag. In the same graph, the theoretical trajectories, without evaporation (Equation 2.14) and with evaporation (Equation 2.14 & Equation 2.15) are plotted respectively with plain black and dashed red curves, they are superimposed on each other. We observe that the model accounts well for the experimental trajectory, validating the assumptions of Equation 2.14. Moreover, the superimposition of the two models shows that, in this case, the trajectory is not modified by the evaporation. It does not mean that no liquid evaporates but simply that the drop radius reduction δR_d is weak compared to the initial drop radius $R_d(0)$. Indeed, in this case $\delta R_d/\ R_d(0)$ reaches less than 0.06 %. This result is consistent but it does not allow us to validate the evaporation model.

Figure 2.18 (b) presents with gray circles the experimental trajectory of a small jet drop ($R_d = 24\ \mu$m). In this case the curve is typical of a trajectory where drag forces prevail over inertia, and the theoretical trajectory without evaporation (Equation 2.14, plain black curve) does not capture the experimental curve. However, when evaporation is considered, (Equation 2.14 & Equation 2.15, dashed red curve) the experimental trajectory is retrieved. In this case, the drop shrinking due to evaporation, $\delta R_d/\ R_d(0) \simeq 20$ %, is important enough to change the drag ($\sim R_d(t)^2$) and modify the trajectory. By capturing reasonably well the experimental trajectory, our evaporation model shows it gives a good estimation of the liquid mass transferred. Note that the experimental determination of the initial radius R_d is not very accurate ($R_d = 24 \pm 3\ \mu$m) therefore the error bar needs to be included in the model: the hatched gray zone and the red zone represent the corresponding error bar in the numerical resolution. Despite the errors and approximations, the experimental trajectory is still well captured by our evaporation model and could not be captured with just a constant radius trajectory model (Equation 2.14). Our evaporation model is therefore well adapted to this system and will be used in the following in order to estimate the evaporated liquid mass for a bubble bursting event.

Evaporation results

We use now the simulations to provide the initial conditions on the droplet dynamics required to implement this simple evaporation model, i.e., the initial size and velocity of all ejected droplets. We obtain the total volume of evaporated liquid per droplet, e.g., for droplet i: $V_{d_i}^{\text{evap}}$.

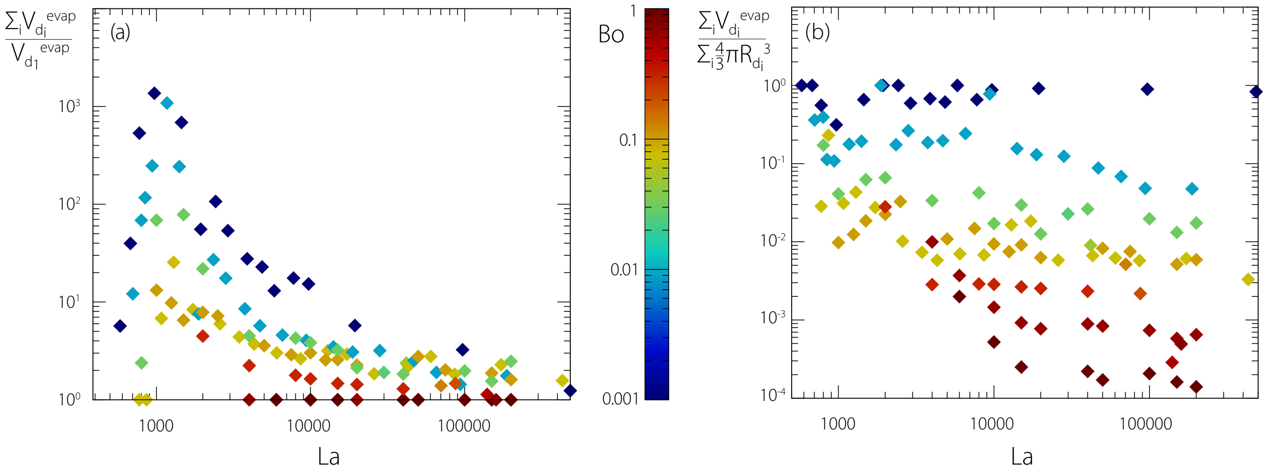

Figure 2.19: (a) Total evaporated volume, $\sum_i V_{d_i}^{\text{evap}}$ normalized by $V_{d_1}^{\text{evap}}$ as a function of Bond and Laplace numbers. The total evaporated volume can be orders of magnitude larger than the evaporated volume from the first drop. (b) Total evaporated volume compare to the total ejected volume of the droplets in the air $\sum_i V_{d_i}^{\text{evap}}$, as a function of Bond and Laplace numbers. For both the Bond number is color coded following the color scale in the middle. By controlling the flight time of the droplet in the air gravity is the main effect acting on the evaporated volume.

Figure 2.19 (a), shows the sum of the evaporated volumes of all the droplets compared to the first one $\sum_i V_{d_i}^{\mathrm{evap}}/V_{d_1}^{\mathrm{evap}}$, as a function of the Laplace and Bond number. When there is more than just one ejected droplet, we observe that the total evaporated volume is at least twice higher than the volume loss by the first drop. Around Laplace close to the singularity ($\sim$1000), it can even be several orders of magnitude larger. This effect becomes less important for larger Bond number, in particular since increasing the Bond number both reduces the number of ejected droplets and the flight time of the droplets in the air. These results are important as they show that the evaporation of the subsequent droplets can not be neglected ($i > 1$); in fact, the evaporation of the droplets following the first one is comparable to the first one and at La around 1000 it even becomes dominant.

Finally, Figure 2.19 (b) shows the total evaporated volume for all the droplets $\sum_i V_{d_i}^{\mathrm{evap}}$, normalized by the initial volume of all the droplets $\sum_i \frac{4}{3}\pi R_{di}^3$, as a function of the Laplace and Bond number. We observe that for vanishing Bond number, the entire droplets are being evaporated. Then it appears that the normalized evaporated mass stays almost independent of the Laplace number and decreases as Bond number is higher. It is interesting to observe that the Bond number mainly controls this normalized evaporation. Its crucial influence on the drop evaporation is probably due to the effect of gravity and the decrease in the ejection velocity.

More interpretation of our evaporation model can be found in the related article [20]. Note that the coupled modeling of the dynamics of the interfaces, temperature and evaporation, while being possible in principle, is a challenging computational problem given the wide range of scales involved. Numerical schemes able to accurately perform this type of coupled thermodynamical modeling are a subject of active research. The relative simplicity of the (experimentally validated) evaporation-trajectory model used in the present study is at present an advantage, compared to the complexity and cost of such future DNS, as it allows one to investigate the effect of multiple droplets on the total evaporation rate, which happens at time scales much larger than the present simulated dynamics.

In terms of applicability of this simple evaporation model in ocean-atmosphere context, it is clear that our model does not take into account any small-scale atmospheric boundary layer above the surface. As such it is more representative of laboratory conditions with essentially still air. The primary influence of an atmospheric boundary layer will be on the flight time of the eject droplets which is expected to increase. The evaporation should still be described by the d^2 relation, however. Indeed, the transport of the particle by the air flow will decrease the relative Reynolds number between the droplet and the air. The flight time could also be corrected according to the characteristics of the boundary layer and the droplet size as discussed by Refs. [14, 40]. Note finally that we do not consider the limiting effects of surface tension and salinity of the water, which limits evaporation for droplets smaller than 80μm, these effects likely preventing complete evaporation of the droplets.

[40] Andreas et al. (1995), *Boundary-Layer Meteorol.* "The spray contribution to net evaporation from the sea: A review of recent progress".

[14] Veron (2015), *Annual Review of Fluid Mechanics*, "Ocean Spray".

2.7 Conclusions

Before concluding, I would like to raise the fact that this chapter tells a story started eight years ago. I chose not to completely rewrite it, even though it leads to some inconsistency, essentially in the scaling laws : for example

Figure 2.6 and Figure 2.10 (b) or Figure 2.14 (b) and Figure 2.16 (a). The reason is that everything is not totally clear yet. The main inconstancy lies in the treatment of gravity and mainly comes from two points: first is to include the Bond number in the scaling (Figure 2.6) or just as a correction (Figure 2.10) ; second is the experimental biais of using a dimensionless number that is constant for a liquid : the Morton number, that also includes gravity and complicates its interpretation. Today, I would think that Figure 2.10 (b) and Figure 2.14 (b) are better, in the sens that the physical ingredients are better presented and easier to interpret. However, strictly speaking, the scaling laws presented in the previous studies are still correct and, still, I can hardly believe that the Bond number is just a correction when I see Figure 2.6 (a). Even more important, the interpretations are still mainly valid and can be applied on the new scalings, as for instance the viscosity sheltering the self similar collapse or the inviscid end-pinching drop.

Despite these few points that still need to be clarified, our work, based on a model experiment, presents unique contributions on the bursting bubble dynamics, from the bubble lying at the free surface to the evaporation of the produced droplets. The outcomes are important both from a fundamental point of view and for the application, in particular in oceanography, or in sparkling wine industry for example. In the general context of the physics of effervescence, we provide a comprehensive picture of the entire process: bubble collapse, counter intuitive role of viscosity, jet formation, and drop detachment, dynamics, trajectory and evaporation.

We fully characterize all the jet droplets produced by bubble bursting, in particular their number, size and velocity as functions of bubble size and liquid properties. The size and velocity distribution of the jet drops aerosol can now easily be computed as long as we know the bubble size distribution. Combining these numerical results with a relatively simple evaporation model, we estimate the mass transfert for all drop during their flight time. Thus, we demonstrated that all the jet droplets play a significant role in the total amount of water evaporated during a single bubble bursting event, in contrast with what was assumed in previous studies where only the first droplet was considered.

The ejection process of the droplets following the first one presents some internal variability, which should be studied systematically with a statistical analysis. Furthermore, the present extensive experimental and numerical data set will nurture the active debate on the theoretical scalings for the number, size and velocity proposed in the literature and the exact physical interpretation of the underlying mechanism [60, 61, 80, 81].

[60] Gañán-Calvo (2017), *Physical review letters*, "Revision of bubble bursting: universal scaling laws of top jet drop size and speed".
[61] Gañán-Calvo (2018), *Phys. Rev. Fluids*, "Scaling laws of top jet drop size and speed from bubble bursting including gravity and inviscid limit".
[80] Gordillo et al. (2019), *Journal of Fluid Mechanics*, "Capillary waves control the ejection of bubble bursting jets".
[81] Blanco-Rodriguez et al. (2020), *Journal of Fluid Mechanics*, "On the sea spray aerosol originated from bubble bursting jets".

Finally, the various scalings and results were obtained considering an idealized configuration of a single bubble bursting in a quiescent liquid, neglecting various effects which could be of importance under realistic ocean-atmosphere conditions, such as the influence of the wave field, the turbulent boundary layers in the air or water, collective effects or complex physico-chemistry of the interface induced by surfactants. The evaporation model we use also presents limitations in the case of sea water which would need to be considered when applying the proposed framework to ocean spray. These will constitute natural developments of this work.

Freezing Drop Impact

3

3.1 Introduction

As introduced in Section 1.3, freezing of capillary flows is widely encountered in many examples and can reveal a very rich behavior [82–84]. In this Chapter, we present our contribution to the understanding of the coupling between drop impact and freezing. When a drop impacts a solid surface, it usually highly deforms, sometimes detaches droplets or bounces, and in all cases takes splendid shapes resulting from a subtle interplay between inertia, surface tension, viscosity and substrate wetting. This iconic problem of fluid mechanics has been, and still is, extensively studied [26, 85]. On the other hand, the freezing of a liquid sphere, considered in the mid-19th century as a model for the earth formation, probably constitutes the first solidification study of history [86], and keeps intriguing researchers today [87]. This work combines these two model problems to report on the unexpected shapes taken by frozen impacted drops, due to the interaction between the drop impact hydrodynamics and its rapid freezing [88, 89].

Understanding this complex coupling would be useful in many different contexts. Probably one of the most relevant is the phenomenon of ice accretion on super-structures such as planes [90], power-lines [91], bridge cables [92] or wind turbines [93]. It can also cause hazardous conditions for pedestrians and cars and thus may cause immeasurable economic losses [94]. Nowadays, the main strategy to prevent most of these undesirable effects is to develop anti-icing surfaces [95], but the results are not satisfying and new paradigms could emerge from a better understanding of the freezing dynamics in complex configurations [96]. When solidification is coupled to drop impact, the geometry of the resulting frozen drop, called splat in metallurgy, can be very diverse, showing in particular various shapes and roughnesses [97] [98]. Knowing the shape of these splats is crucial as they enter in models of plasma spraying, a well-established means of forming thick coatings (300μm) useful in many applications (thermal protection, resistance to corrosion, oxidation ...) [99–102]. Finally, when the solid layer becomes cooler it contracts and the frozen structure can either remain stuck on the substrate or detach through a self-peeling process [103] or even fragment into a myriad of small ice pieces [33]. These behaviors depend on the thickness of the frozen impacted drop and the substrate temperature, and are crucial in the context of de-icing. Therefore, we understand how much it is important to have a precise prediction of the shape, or more precisely of the thickness profil, of the solid drop after freezing.

Without impact, the simplest case of the freezing of a sessile drop on a cold surface, already gives rise to a surprising pointy ice drop [104, 105], raising the question of the contact angle between water and ice [106]. When the drop is deposited on the substrate, the frozen drop shape and thickness depend on the contact line solidification dynamics [107–109]. In this work, we aim at understanding the subtle coupling giving rise to the frozen shape and obtaining a prediction of the final ice thickness resulting from the impact of a drop on cold surfaces.

[82] CHEN et al. (2011), *Physical Review E*, "Experiments on the morphology of icicles".

[83] MOORE et al. (2017), *Journal of Fluid Mechanics*, "Ice formation within a thin film flowing over a flat plate".

[84] AHMADI et al. (2019), *Nature communications*, "How soap bubbles freeze".

[85] WORTHINGTON (1876 - 1877), *Proceedings of the Royal Society of London*, "On the Forms Assumed by Drops of Liquids Falling Vertically on a Horizontal Plate".

[26] JOSSERAND et al. (2016), *Annual Review of Fluid Mechanics*, "Drop impact on a solid surface".

[86] LAMÉ et al. (1831), , "Mémoire sur la solidification par refroidissement d'un globe liquide".

[87] WILDEMAN et al. (2017), *Physical Review Letters*, "Fast Dynamics of Water Droplets Freezing from the Outside In".

[90] CEBECI et al. (2003), *Annual review of fluid mechanics*, "Aircraft icing".

[94] JONES (1996), , "Ice accretion in freezing rain.".

[95] KREDER et al. (2016), *Nature Reviews Materials*, "Design of anti-icing surfaces: smooth, textured or slippery?".

[97] DHIMAN et al. (2007), *Surface and Coatings Technology*, "Predicting splat morphology in a thermal spray process".

[103] RUITER et al. (2018), *Nature Physics*, "Self-peeling of impacting droplets".

[33] GHABACHE et al. (2016), *Physical Review Letters*, "Frozen impacted drop: From fragmentation to hierarchical crack patterns".

The chapter is organized as follows: after presenting the experimental setup (Section 3.2), we introduce the two generic shape of a frozen drop as illustrated in Figure 3.1 (Section 3.3). Then, the solidification dynamics of a liquid suddenly put in contact with a cold substrate is tackled from a general point of view in Section 3.4. We develop and interpret a theoretical model of heat and solidification front propagation, and we compare it to a dedicated model experiment. In the following of the chapter, the drop impact on cold substrate is analyzed step by step. Section 3.5 is focused on the drop spreading at impact, the maximum spreading diameter is given as function of the thermal parameter. Finally, Section 3.6 and Section 3.7 are dedicated to the complex building of the frozen structure (Figure 3.1), resulting from the subtle interplay of solidification dynamics and dewetting of water on ice.

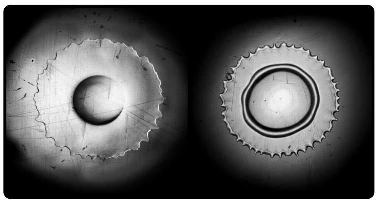

Figure 3.1: Two different shapes of the frozen drop.

3.2 Experimental setup

Our drop impact setup is presented in Figure 3.2, it consists of a syringe pump pushing water at room temperature through a capillary tube from which the drop falls. As the pumping is slow enough, the size of the drop is entirely controlled by the radius of the capillary tube. We used two different drop radii: R = 1.9 mm and 1.2 mm. The impact velocity U_0 is controlled by the height of fall H, which in our case ranges from 15 cm to 45 cm, so that U_0 ranges from 1.7 m.s^{-1} to 3 m.s^{-1} (following roughly $U_0 = \sqrt{2gH}$).

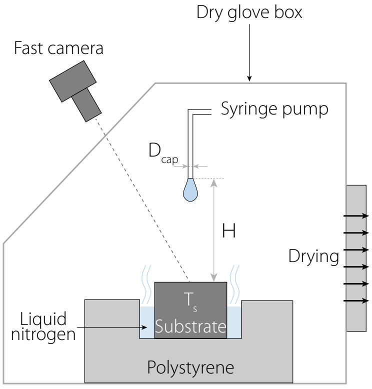

Figure 3.2: Experimental setup.

We use three large blocks (100 × 100× 30 mm) of different materials (steel, copper, marble) as substrates, their distinct thermal properties, given in Table 3.1, allowing us to change the rate of freezing [110] [103]. The substrate is placed into a bowl and cooled down by pouring a certain amount of liquid nitrogen (Figure 3.2). The minimal temperature reached in this work is around −100°C. Due to the substrate heat capacity and to the bowl thermal isolation, it takes several hours for the system to warm up to room temperature. The change in the substrate temperature is thus much less than 1°C during the time of an experiment which is roughly 1 second.

[110] Bennett et al. (1994), *Journal of Materials Science*, "Heat transfer aspects of splat-quench solidification: modelling and experiment".

This experiment is placed inside a dry air chamber in order to minimize the frost formation. The substrate temperature T_s is measured before each experiment using a surface thermometer. The impact dynamic is studied using a high-speed camera. The height profile of the frozen drop is extracted with a polychromatic confocal sensor moving along a translation platform[1] .

[1] The profilometer is a CCS Optima+ from STIL Optics mounted with the CL3MG70 optical sensor. It enables the location of an interface with a precision of order 1 μm refreshed at 10kgHz. It is translated at a constant 1 mm.s^{-1} velocity above the ice-air interface. It yields the distance between the sensor and the ice versus time, which gives us the height profiles.

Table 3.1: Thermal properties of the materials used in the study: density (ρ), thermal conductivity (k), heat capacity at constant pressure (c_p) and thermal diffusivity (α). From Lide [111].

Material	ρ (kg.m^{-3})	k (W.m^{-1}.K^{-1})	c_p (J.kg^{-1}.K^{-1})	α (mm^2.kg^{-1})
Water	1000	0.58	4185	0.14
Ice	916	2.14	2110	1.1
Copper	8960	401	380	110
Steel	7800	16	400	5.1
Marble	2500	3.1	880	1.4

3.3 Qualitative description

This section is mainly extracted from: [32] Thiévenaz et al. (2020), *Phys. Rev. Fluids*, "Retraction and freezing of a water film on ice".

At room temperature, as a water drop impacts a solid substrate, it spreads, reaches a maximal radius and immediately starts to retract back to an equilibrium radius [26]. The impact of a water drop on a cold substrate is represented by two timelines (Figure 3.3 (a)&(b)) corresponding to two

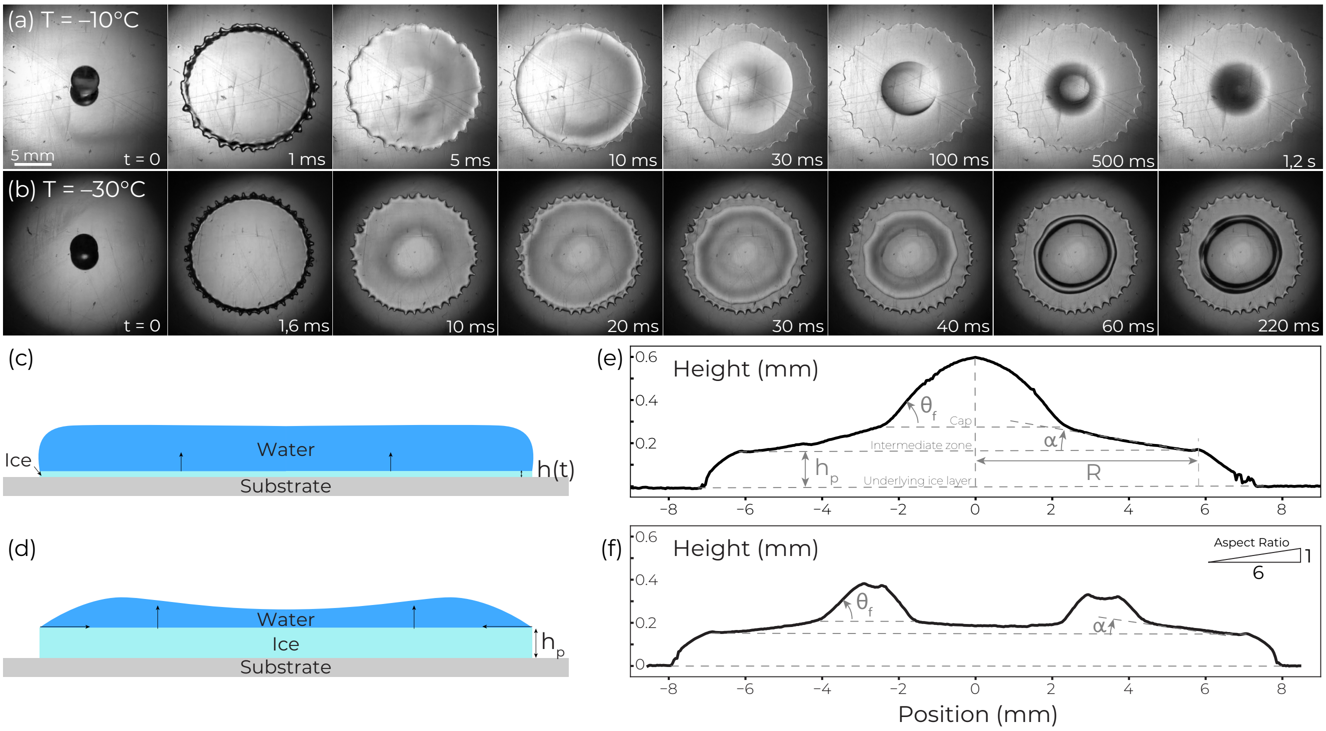

Figure 3.3: (a)&(b) Images sequences of the impact of a water drop on a cold aluminium surface at two different temperatures. (c)&(d) Schematic view of the first instants of a drop impacting a supercooled substrate, in particular the ice and water dynamics. (e)&(f) Height profiles extracted from experiments similar to (a)&(b). The two ice structures will be referred as *cap* (a,e) and *ring* patterns (b, f). The uncertainty Δh is of order 1μm.

different substrate temperatures: -10°C and -30°C. In the first milliseconds of the impact the drop spreads and reaches its maximal diameter (second image). We observe that this maximal spreading diameter appears slightly larger for -10°C than for -30°C, suggesting that the rapid spreading after impact is affected by the solidification. The coupling between spreading and solidification will be analyzed in Section 3.5.

After reaching its maximum diameter (second image), the drop does not retract, it is stuck at its maximal diameter. This pinning is due to the formation of a thin layer of ice between the substrate and the liquid during the spreading. Before the third image of each sequence, the system is thus in the configuration described by Figure 3.3 (c): a thin layer of ice attached to the substrate and growing vertically, beneath a liquid film pinned at the edge of the ice layer Freezing goes on and the ice layer grows following the classical self-similar diffusive law $h(t) \propto \sqrt{t}$ as in the Stefan problems [112]. In Section 3.6 an excellent estimation of the effective diffusion coefficient is obtained by taking into account the heat propagation in the ice and in the substrate. The remaining water layer is not stable due to its high aspect ratio, so that it still needs to retract in order to reach its equilibrium, and at the fourth image, the contact angle of the water on ice has relaxed down to its deweting value (Section 3.6) and the liquid layer can start its retraction (configuration schematized in Figure 3.3 (d)). The thickness of the ice layer at this point is called h_p.

[112] Rubinstein (1971), , "The Stefan Problem".

Between the fourth and the sixth image the liquid retracts on ice, leading to the two different shapes: a spherical cap (Figure 3.3 (a)) or a half-ring (Figure 3.3 (b)) of water on top of a thin ice disc (Section 3.7). Finally, the remaining liquid finishes freezing quasi-statically, over a few hundreds of milliseconds.

The retraction of a liquid on its own solid phase is not *a priori* expected thermodynamically, this is in fact not observed for molten metal or wax drop impacts [109, 113] and seems to be a peculiar feature of water. It indicates in particular that liquid water and ice exhibit a non-zero contact angle as it has already been observed in a few other configurations [106, 114–116].

Figure 3.3 (e)&(f) present the height profiles of the frozen drops obtained by scanning the drop diameter with our optical profilometer. They correspond to the two shapes observed in (a) and (b) and define the notations used in the following. Note that the aspect ratio of these two figures is 6, meaning that these ice structures are really flat: typically a few hundreds of microns thick and about one centimeter wide. On both profiles we can observe three different zones: the underlying ice layer of thickness h_p (the so-called ice pancake), the pattern on the top, which can be a spherical *cap* (Figure 3.3 (e)) or a *ring* (Figure 3.3 (f)), and an intermediate zone. We define the angle α as the angle between the ice-air interface and the horizontal in the intermediate zone, and the angle θ_f between the pattern and the horizontal. In the following, our goal is to quantitatively characterize the formation of such ice structures.

Figure 3.4: Josef Stefan (24 March 1835 – 7 January 1893) was an Slovene physicist, mathematician, and poet of the Austrian Empire.

3.4 Solidification dynamics of a liquid on a substrate

We begin this quantitative study by introducing a simplified 1-D solidification model that aims at describing the solidification front dynamics in the problem of a liquid film on a cold solid substrate. It will be essential to the description of the frozen drop formation.

This section is mainly extracted from: [30] Thiévenaz et al. (2019), *J. Fluid Mech.*, "Solidification dynamics of an impacted drop".

Presentation of the problem

We consider a material existing in two phase states: liquid and solid, on top of a cold substrate. As schematized in Figure 3.5, the flat solid substrate is infinite and fills the halfspace $z < 0$, with a temperature T_s below the melting temperature T_m. It is in contact with the solid layer of the material (for $0 < z < h(t)$), that is growing in its melt ($z > h(t)$). $h(t)$ is the position of the solidification front. This configuration belongs to the large class of Stefan problems, a particular kind of boundary value problem where a phase boundary can move with time. It is named after Josef Stefan (Figure 3.4) who first, in 1889, solved the original configuration in which a solidification front propagates between two phases (liquid and solid) of the same material, without substrate [117, 118]. In Figure 3.5, this *original Stefan problem* amounts to replace the substrate by the solid phase.

[117] Stefan (1891), *Ann. Physik Chemie*, "Über die Theorie der Eisbildung, insbesondere über die Eisbildung im Polarmeere".

[118] Brillouin (1930), , "Sur quelques problèmes non résolus de la Physique Mathématique classique Propagation de la fusion".

Configurations belonging to Stefan problems, even restricted to the solidification-melting phase change, are abundant, in an impressively wide range of application. We can cite as examples: the solidification of the earth, supposed to be molten at the origin, which triggered the first work of interest in this area, by Gabriel Lamé (1795 - 1870) and Benoît Paul Émile Clapeyron (1799 - 1864) [86]. Or the formation of ice crystals, like snowflakes, that grow out from seeds in an environment of supersaturated water vapor. In this problem the ingredients of the original Stefan problem are not sufficient, Gibbs-Thomson equation and 3D effects need to be added [119]. Also, the modelling of the dynamics of sea ice on the surface of the polar oceans [120] or the shape of an icicle [121], where the liquid motions and the associated convective heat

[86] Lamé et al. (1831), , "Mémoire sur la solidification par refroidissement d'un globe liquide".

[119] Langer (1980), *Reviews of Modern Physics*, "Instabilities and pattern formation in crystal growth".

[120] Worster (2000), *Perspectives in fluid dynamics: a collective introduction to current research*, "Solidifcation of Fluids".

[121] Neufeld et al. (2010), *Journal of Fluid Mechanics*, "On the mechanisms of icicle evolution".

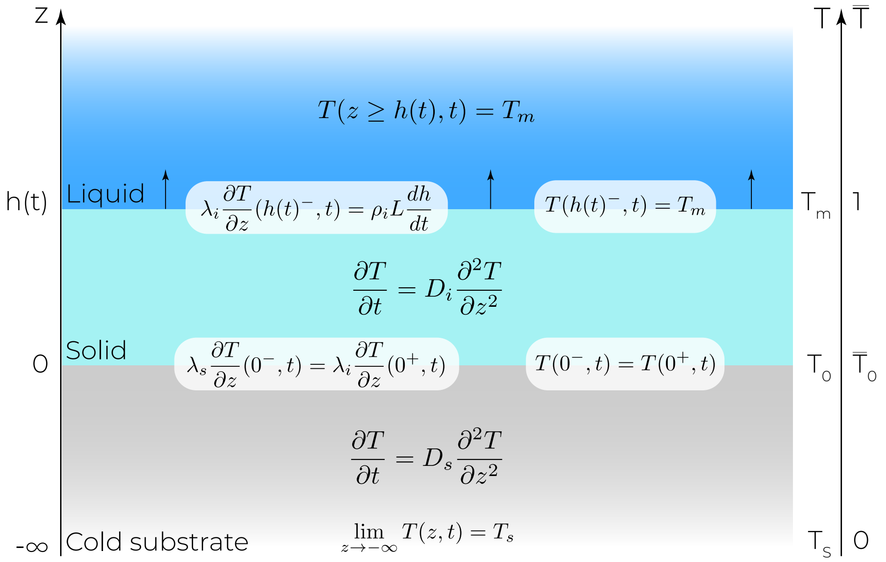

Figure 3.5: Summary of the model hypotheses: A finite layer of solid lies between the semi-infinite melt ($z > h(t)$) and the semi-infinite substrate ($z < 0$). The temperature of the whole melt is set constant at the melting point ($T = T_m$), while the temperature of the substrate tends to T_S when z goes to $-\infty$. The temperature in the solid phases is given by a set of two heat equations, with a specific diffusion coefficient D_k for each phase, coupled by the temperature and heat flux continuity at $z = 0$. At the solidification front ($z = h(t)$), the Stefan condition imposes the downward thermal flux be equal to the latent heat liberated by the freezing.

transfert have to be considered. *Idem* for various lava flows [122] that cool and gradually solidify until they come to rest. Cooling can occur from the surrounding atmosphere (or water) or from the underlying solid [123], and in ancient time, some of the lavas were hotter than today and were even capable of melting the underlying rock and shaping their own thermal erosion bed [124]. In industry, Stefan problems are often studied in the context of melting or solidification of metals or metal alloys [125], where the properties of the solid (in particular, its mechanical and thermal properties) are functions of the kinetics of solidification, such that Czochralski crystal growth, used for example in the fabrication of semi-conductor wafers [126], laser welding [127], or synthesis of nanoparticles from metal films melting [128]. Finally, this class of problems is also a fantastic playground for mathematicians [112, 129]. But to the best of our knowledge, we are not aware of a system of equations modeling solid growth by a sudden contact between a liquid and a cold solid substrate.

In the following, we assume the melt stays at rest, at constant temperature everywhere (T_m). We neglect the variation of heat capacity and of thermal conductivity with temperature. We also neglect the thermal expansion, and more generally the variation of density. In other words, the thermal parameters of the media are the following: the latent heat of solidification L, the heat capacity C_{pk}, the thermal conductivity λ_k, the heat diffusion coefficient $D_k = \lambda_k/(\rho_k C_{pk})$ and the density ρ_k, are taken as constant. The subscript k stands for l in the liquid phase, i in the solid phase and s for the substrate (Figure 3.5). The approximation of taking the liquid at the melting temperature T_m will be discussed in the experimental comparison paragraph. It can be justified *a priori* by both, the small thickness of the liquid layer and the little energy needed to cool the water down to its melting temperature: $C_{pl}(T_d - T_m) \sim 4000 \times 20 \sim 8 \cdot 10^4$ J·kg^{-1}, where T_d is the initial temperature of the liquid drop, compared to the latent heat for solidification ($L \sim 3 \cdot 10^5$ J·kg^{-1}).

Under these assumptions, the mathematical problem that needs to be solved is described in Figure 3.5: a constant temperature T_m in the liquid, two heat equations for the temperature field $T(z, t)$, and four boundary conditions. At the solid-substrate interface ($z = 0$) they impose both the continuity of the temperature and of the heat flux, and at the solid-liquid interface ($z = h(t)$) they impose both the continuity of the temperature and the law

[122] Griffiths (2000), *Annual Review of Fluid Mechanics*, "The dynamics of lava flows".

[123] Huppert (1989), *Journal of Fluid Mechanics*, "Phase changes following the initiation of a hot turbulent flow over a cold solid surface".

[124] Huppert (1986), *Journal of Fluid Mechanics*, "The intrusion of fluid mechanics into geology".

[125] Viskanta (1988), *Journal of Heat Transfer*, "Heat transfer during melting and solidification of metals".

[126] Nishinaga (2014), , "Handbook of crystal growth: fundamentals".

[127] Allmen et al. (2013), , "Laser-beam interactions with materials: physical principles and applications".

[128] Font et al. (2017), *Int. J. Heat Mass Transf.* "Substrate melting during laser heating of nanoscale metal films".

[112] Rubinstein (1971), , "The Stefan Problem".

[129] Gupta (2003), , "The Classical Stefan Problem - Basic Concepts, Modelling and Analysis".

of motion of the solidification front. This energy conservation law under liquid-solid phase change is called the *Stefan condition*. Here, it imposes that the solidification front velocity is proportional to the rate at which latent heat can be transported in the solid phase. The solidification front is thus controlled by the diffusion in the solid and the substrate through the Stefan condition. Finally, we impose a constant temperature T_s far in the substrate and we complement this set of equations by the initial conditions taken at $t = 0$: $T(z, 0) = T_s$ for $z \leq 0$ and $h(0) = 0$, indicating that at $t = 0$ the liquid is suddenly put in contact with the substrate.

Solution of our unidimensional solidification model

Similarity analysis shows that this diffusive problem exhibits a self-similar structure, with the usual self-similar variables involved in diffusion problems, namely $\frac{z}{\sqrt{D_i t}}$ in the ice and $\frac{z}{\sqrt{D_s t}}$ in the substrate, even in the presence of the moving solidification front. In this case, the solidification front location follows also a square-root in time law, witnessing the diffusive property of the dynamics:

$$h(t) = \sqrt{D_{\text{eff}} t} \tag{3.1}$$

where D_{eff} is the effective diffusion coefficient that determines the growth of the solid layer. It is really the quantity of interest of our problem that we need to compute.

Introducing the self-similar variable in the set of equations of Figure 3.5 we obtain the following solutions for the temperature field:

$$T(z,t) = T_0 + (T_0 - T_s) \cdot \text{Erf}\left(\frac{z}{2\sqrt{D_s t}}\right) \quad \text{for } z \leq 0 \quad \text{and} \tag{3.2}$$

$$T(z,t) = T_0 + \frac{e_s}{e_i}(T_0 - T_s) \cdot \text{Erf}\left(\frac{z}{2\sqrt{D_i t}}\right) \quad \text{for } 0 \leq z \leq h(t) \tag{3.3}$$

The error function, Erf, is defined by:

$$\text{Erf}(x) = \frac{2}{\sqrt{\pi}} \int_0^x e^{-\xi^2} d\xi. \tag{3.4}$$

where $e_{s,i} = \sqrt{\lambda_{s,i}\rho_{s,i}C_{ps,i}}$ are the effusivities of the substrate and the solid, and T_0 the contact temperature at the solid-substrate interface, a constant in time in this self-similar framework. The effusivity of a material is the physical quantity that witnesses both its heat capacity and its ability to diffuse it. T_0 is an integration constant to be determined by the boundary conditions. Then, by imposing the Stefan condition at $z = h(t)$, we obtain the following transcendental equation:

$$\text{St} = \frac{\sqrt{\pi\beta}}{2} e^{\frac{\beta}{4}} \left(\frac{e_i}{e_s} + \text{Erf}\left(\frac{\sqrt{\beta}}{2}\right)\right) \tag{3.5}$$

that links St, the Stefan number, with the ratio of the diffusion coefficients β, defined respectively by:

$$\text{St} = \frac{C_{pi}(T_m - T_s)}{L} \quad \text{and} \quad \beta = \frac{D_{\text{eff}}}{D_i}. \tag{3.6}$$

This implicit Equation 3.5 has to be solved numerically and the values of D_{eff} used further on are those obtained numerically. From the Equation 3.5 it is easy to deduce the asymptotic behaviours for small and large Stefan numbers:

$$\beta \sim \frac{4e_s^2}{\pi e_i^2}\text{St}^2 \quad \text{for St} \ll 1, \qquad \text{and} \qquad \beta \sim 4\ln(\text{St}) \quad \text{for St} \gg 1. \tag{3.7}$$

Note that in the case the substrate has a high effusivity, the ratio of effusivity is much smaller than one (for copper $e_i/e_s \simeq 0.05$, for steel $e_i/e_s \simeq 0.3$) and the asymptotic behaviour for small Stefan numbers becomes:

$$\beta \sim \frac{4}{\sqrt{\pi}} St \quad \text{for St} \ll 1 \text{ and } \frac{e_i}{e_s} \ll 1. \tag{3.8}$$

Experimental comparison

In the aim of validating our model and its assumptions, we carry out a model experiment which consists in putting in contact a liquid with a substrate at a temperature below the solidification temperature (Figure 3.6). The liquid is initially poured in a transparent PMMA tube of 3.4 cm diameter. We use two different liquids (water and hexadecane) and two different substrates (copper and steel). We also vary the initial temperature of the water (20 and 0°C) and the thickness of the initial water layer (between 4 millimeters and a few centimeters). Finally, the propagation of the solidification front, h(t), is recorded using a camera, between one and ten frames per second depending on the experiment.

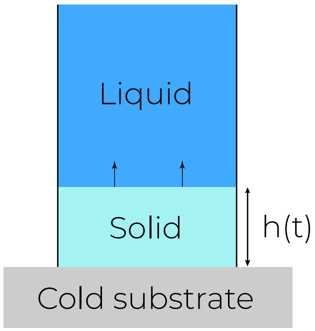

Figure 3.6: Schematic of the experimental setup: a liquid-filled cylinder is set upon a cold substrate. The liquid starts freezing into a solid layer of thickness $h(t)$.

Figure 3.7 (a) presents the growth of the ice layer, h(t), with respect to time for water solidifying on a copper substrate. The blue and red squares are for water at 20°C and two different temperatures of the substrate, respectively -38°C and -26°C as indicated in the graph. As expected the freezing front propagates faster when the substrate is colder. In the same graph, the empty triangles show the front propagation with water initially at 0°C. Their variations coincide with the preceding ones on the whole range of time, indicating that solidifying water at 20°C or at 0°C gives rise to the same solidification dynamics. This important observation justifies *a posteriori* the approximation to consider the liquid layer at T_m in the model and to neglect the heat flux in the liquid. Superimposed on these four experimental curves, the lines are the best fit

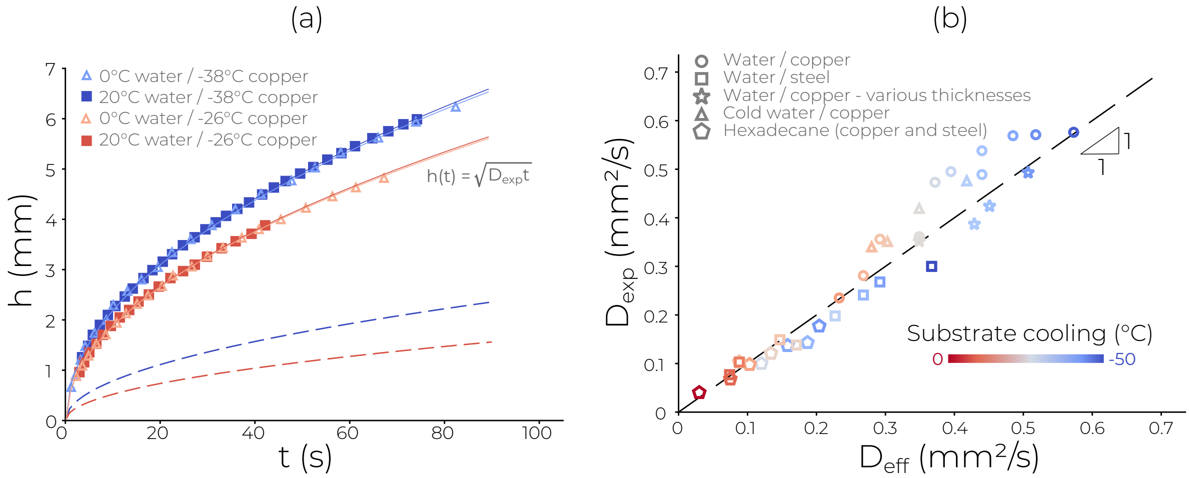

Figure 3.7: (a) Growth of the solid phase as a function of time. $h(t)$ is plotted in the case of water freezing on a copper plate at two different temperatures (blue and red squares), the liquid being initially at room temperature. The same experiments are repeated with water slightly warmer than 0°C (triangles), showing no differences. The dynamic of each experiment is fitted by a square root function (full lines), in order to get its diffusion coefficient D_{exp}. Dashed lines represents the dynamic predicted by the *classical Stefan problem* (without the substrate), for the two different temperatures. (b) Comparison of the experimental freezing dynamic and the theory: The diffusion coefficients D_{exp} and D_{eff}, respectively experimental and theoretical, are compared for a wide range of parameters. The colour refers to the substrate cooling $\Delta T = T_s - T_m$. Circles (respectively squares) represents water at room temperature freezing on copper (respectively steel). Stars refer to thin thicknesses of water freezing on copper, triangles to 0°C water freezing on copper. Finally, pentagons are for hexadecane freezing on both metals. The $y = x$ guideline is shown as a dashed line.

using a square root function of the form:

$$h(t) = \sqrt{D_{\mathrm{exp}} t}, \tag{3.9}$$

with D_{exp} an experimental diffusion coefficient that quantifies the solidification dynamics. We observe that, as shown in the model, the solidification front follows a diffusive law. Finally, we plot on the same graph with dashed line the variation of h(t) given by the *classical Stefan problem* associated to the two substrate temperatures. In these plots, the substrate is treated as if it was ice and the thermal parameters of the substrate are consequently note taken into account. It appears that, by promoting the heat transfert, the substrate highly increases the front propagation velocity.

By fitting the solidification front evolution by Equation 3.9 on each experiment we obtain D_{exp}, the experimental diffusion coefficients. In Figure 3.7 (b) we compare them to the effective diffusion coefficient given by our 1D model D_{eff}, for all of our experiments: water (0, 20°C and different liquid thicknesses) and hexadecane, on copper and steel (see the different markers on the graph), and for various substrate temperatures between 0 and -50°C, indicated by the colour of the markers. All the data gather along the black dashed line that has a slope of 1, indicating that for each experiment $D_{\mathrm{exp}} \simeq D_{\mathrm{eff}}$: our 1D model provides therefore an excellent estimation of the dynamics of the upwards solidification when a liquid is placed on the top of a cold substrate.

3.5 Drop spreading on a cold surface

We now start the study of a drop impact on a cold substrate, and we begin with the initial drop spreading. We will see how it is influenced by the liquid solidification, even at the very first time.

This section is mainly extracted from: [31] Thiévenaz et al. (2020), *Subm. to Europhys. Lett.*, "Freezing-damped impact of a water drop".

Introduction

The sole question of how does a liquid drop spread on a solid surface has given rise to a wide literature [26]. Particularly, researchers have been interested in scaling laws for the maximal spreading of the drop, depending on whether the resisting force to spreading is viscosity [99] or capillarity [130] and often both [131]. The coupling between spreading and solidification has also been investigated, but mainly in the context of low impact velocity, namely drop deposition [107–109]. The few studies on drop impacts spreading and solidification rather focused on molten metal droplets [132]. But, in the general case, the maximum spreading of the solidifying impacting drop remains a largely open question.

[99] Madejski (1976), *Int. J. Heat Mass Transf.* "Solidification of droplets on a cold surface".

[130] Clanet et al. (2004), *J. Fluid Mech*, "Maximal deformation of an impacting drop".

[131] Laan et al. (2014), *Physical Review Applied*, "Maximum Diameter of Impacting Liquid Droplets".

[109] Schiaffino et al. (1997), *Phys. Fluids*, "Motion and arrest of a molten contact line on a cold surface: an experimental study".

[108] Tavakoli et al. (2014), *Langmuir*, "Spreading and arrest of a molten liquid on cold substrates".

[107] De Ruiter et al. (2017), *Phys. Rev. Fluids*, "Contact line arrest in solidifying spreading drops".

[132] Gielen et al. (2020), *J. Fluid Mech.* "Solidification of liquid metal drops during impact".

In this section, we investigate experimentally the spreading and freezing of water drops at room temperature on a silicon wafer cooled down below 0°C. By observing the similarities between viscous damping and solidification, we are able to reduce this complex problem, which couples flow and thermal diffusion, to the simple case of an isothermal viscous drop impact with an effective viscosity. We thus obtain a way to express the maximal spreading radius of the drop as a function of the freezing rate and the liquid parameters.

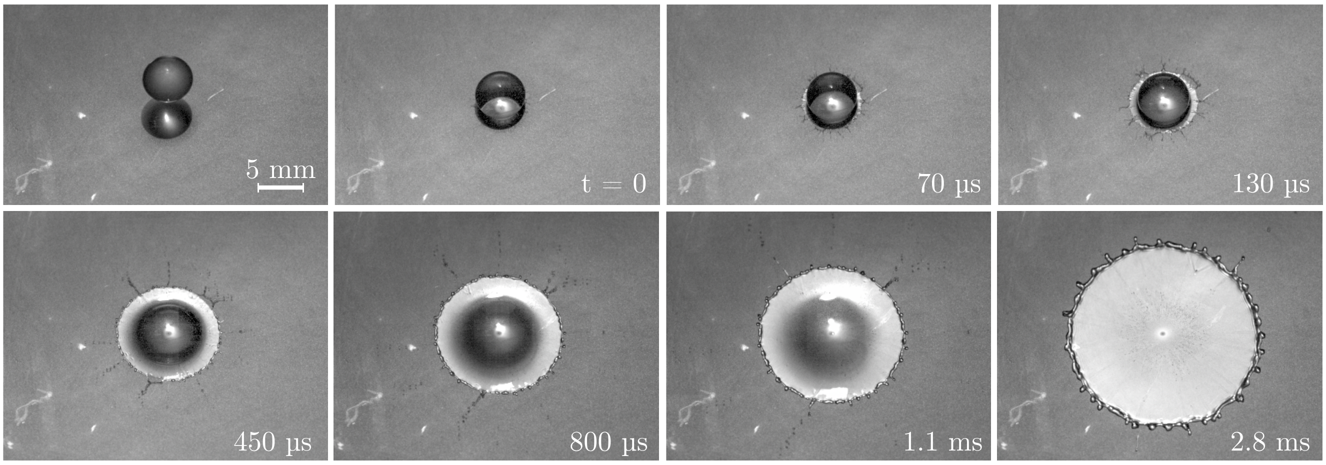

Figure 3.8: Image sequence of a drop impacting at $U_0 = 3.1$ m.s^{-1} and spreading on a silicon wafer at -19°C.

Qualitative observation

Figure 3.8 presents the typical impact dynamics which occurs within a few milliseconds, for a drop impacting a silicon wafer at $T_s = -19°\text{C}$. The drop impacts at $t = 0$ then starts spreading. It reaches its maximal radius $R_{\max}$ after 3 ms. During the spreading, liquid is pushed outward into a rim, which may destabilize and form corrugations. After a much longer time the drop is completely frozen (Figure 3.3), through the mechanisms that will be described in the next sections [30, 32].

Splashing, that is the detachment of droplets from the main drop, can be observed in some cases. However, since the volume of liquid ejected remains negligible, we choose to neglect its effect on the maximum radius.

[30] Thiévenaz et al. (2019), *J. Fluid Mech.* "Solidification dynamics of an impacted drop".
[32] Thiévenaz et al. (2020), *Phys. Rev. Fluids*, "Retraction and freezing of a water film on ice".

Maximum spreading

In order to characterise the dynamics of the spreading drop, we define: the spreading parameter ξ as the ratio between the radius of the liquid film at time t, $R(t)$, and the initial radius of the drop R_0 ; and its maximal value $\xi_{\max}$, yielding:

$$\xi(t) = \frac{R(t)}{R_0}; \qquad \xi_{\max} = \frac{R_{\max}}{R_0} \tag{3.10}$$

Figure 3.9 (a) shows the evolution of the spreading parameter $\xi(t)$ versus the non-dimensionalised time: $\tau = U_0 t/R_0$, for two different experiments corresponding to two different substrate temperatures with the same impact velocity. It appears clearly that at lower temperature (blue curve, $T_s = -84°\text{C}$), the drop spreads less far than at room temperature (red curve, $T_s = 18°\text{C}$). This observation is reinforced by Figure 3.9 (b), which plots the maximal spreading parameter $\xi_{\max}$ versus the substrate temperature, for constant impact velocity and drop radius. Although above 0°C the value of $\xi_{\max}$ does not show any significant trend, below 0°C the maximal spreading parameter decreases slowly: over the considered substrate temperature range, $\xi_{\max}$ drops by about 40%. This change of behaviour across 0°C suggests a role of the solidification rather than the temperature in the damping of the drop impact.

Figure 3.9 (b) concerns a single value of U_0. In order to gather the whole range of impact velocities on the same graph, the maximal spreading parameter is plotted in Figure 3.9 (c) versus the Reynolds number, for each of our

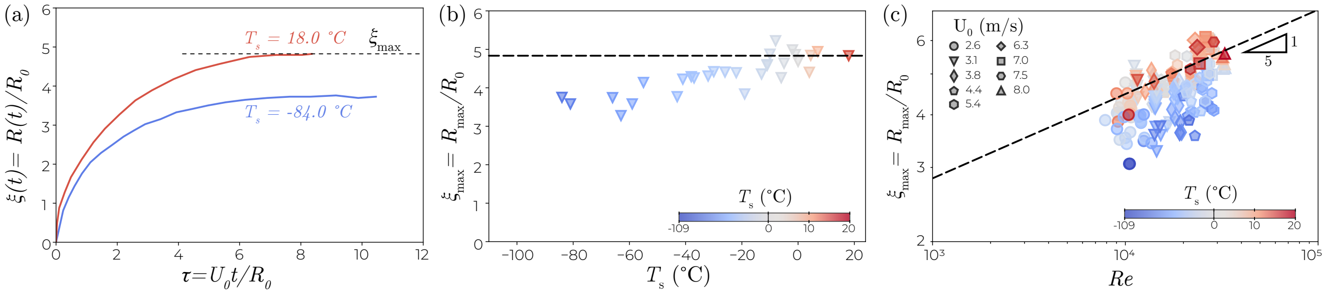

Figure 3.9: (a) Comparison of the non-dimensional spreading dynamic $\xi = f(\tau)$ for two substrate temperature T_s. (b) Maximal spreading ξ_{max} versus the substrate temperature T_s, for a given $U_0 = 3.1$ m.s^{-1} . At -100°C, it has dropped 40% of its room temperature value (dashed line). (c) Maximal spreading versus the Reynolds number for different substrate temperatures (colours, red for hot) and for U_0 varying between 1.7 and 8 m.s^{-1} (symbols). Experiments at $T_s \geq 0$°C (warm colours) show a good agreement with a power law 1/5 (dashed line). However, this is not the case for experiments at $T_s < 0$°C (cold colours) in which water freezes.

experiments at different temperatures and impact velocities. The data for substrate temperatures above the melting temperature, that appear in red, all gather on the same line of slope 1/5 in this logarithmic diagram. As expected, data for negative substrate temperatures fall systematically below this line, and the colder the substrate the smaller the spreading radius. The following is dedicated to propose a model to explain this difference, in other words to understand the influence of temperature in the maximum spreading of a drop impact.

Viscous damping characterisation

The spreading of a drop on a solid substrate has a long history [130, 133–135] that has reached a consensus only recently [131, 136]. The spreading dynamic is controlled by the balance between the drop inertia on one hand, and both capillarity and viscous forces on the other hand. The difficulty lies in the correct estimate of the interplay between the viscous and the capillary damping mechanisms, and the solution is in fact deduced by analysing their asymptotic behaviours [135]. When viscous dissipation can be neglected, the energy balance between inertia and capillarity gives a maximum spreading radius scaling like $\xi_{max} \sim We^{1/2}$. Oppositely, when capillary forces can be neglected, the maximum spreading radius R_{max} is reached when the thickness of the spreading drop ($\sim R_0^3/R_{max}^2$ using mass conservation) becomes comparable to the thickness of the viscous boundary layer, which obeys the usual diffusive growth law, to reach: $\delta_\nu = \sqrt{\nu R_{max}/U_0}$. This gives the scaling [99, 130, 134]:

$$\xi_{max} \sim Re^{1/5} \tag{3.11}$$

which has been verified experimentally [137]. These two asymptotic regimes have suggested the following general law for the maximum spreading [135]: $\xi_{max} = Re^{1/5} f(P)$, where $P = We Re^{-2/5}$ is the impact parameter. The function f behaves as $f(x) \sim 1$ when $x \to \infty$ and $f(x) \sim \sqrt{x}$ when $x \ll 1$, in agreement with the asymptotic regimes. Using a Padé approximant method, Laan *et al.* [131] have proposed the following approximation for $f(x) = x/(A + x)$, leading to the formula for the maximum spreading factor:

[133] Madejski (1983), *International Journal of Heat and Mass Transfer*, "Droplets on impact with a solid surface".
[130] Clanet et al. (2004), *J. Fluid Mech*, "Maximal deformation of an impacting drop".
[134] Fedorchenko et al. (2005), *Physics of Fluids*, "Effect of capillary and viscous forces on spreading of a liquid drop impinging on a solid surface".
[135] Eggers et al. (2010), *Physics of Fluids*, "Drop dynamics after impact on a solid wall: theory and simulations".
[131] Laan et al. (2014), *Physical Review Applied*, "Maximum Diameter of Impacting Liquid Droplets".
[136] Lee et al. (2016), *Journal of Fluid Mechanics*, "Universal rescaling of drop impact on smooth and rough surfaces".
[137] Lagubeau et al. (2012), *Journal of Fluid Mechanics*, "Spreading dynamics of drop impacts".

$$\xi_{max} \sim Re^{1/5} \frac{P^{1/2}}{A + P^{1/2}}, \tag{3.12}$$

$$\mathrm{We} = \frac{\rho U_0^2 R_0}{\gamma}$$

$$\mathrm{Re} = \frac{U_0 R_0}{\nu}$$

where A is a fitting parameter of order one (found to be $A = 1.24$ in Ref. [131]). This formula gathers most of the known experimental and numerical results on a single curve, and a more refined version of it has been obtained later accounting for the liquid-substrate contact angle [136]. Remarkably, in our experiments the impact factor P varies from 7.8 to almost 57, indicating that we are in the large P regime where the maximum spreading radius is controlled by the viscous dissipation and follows a $Re^{1/5}$ law, as observed on Figure 3.9 (c) for the non-freezing case. This is also justified by the small values of the capillary number that compares the capillary and viscous forces, $Ca = \mu U_0/\gamma$, which in our experiments ranges from 0.036 to 0.11. The prefactor of the $Re^{1/5}$ scaling law, plotted with dashed line in Figure 3.9 (c), is fitted to the experiments with $T_\mathrm{s} > 0°\mathrm{C}$.

Effective viscosity

Experiments above 0°C, in shades of redx in Figure 3.9 (c), show a good agreement with the scaling law. On the other hand, for $T_\mathrm{s} < 0$ the spreading parameter is systematically below this curve, showing that some additional damping is at work. We have seen in the previous section that when water is in contact with a substrate at a temperature below the freezing point, a layer of ice grows upward from the substrate, and its thickness is controlled by thermal diffusion inside the ice. The growth of this ice layer, $\delta_\mathrm{f} = \sqrt{D_\mathrm{eff}t}$, is similar to that of the viscous boundary layer, $\delta_\nu = \sqrt{\nu t}$, where D_eff is our diffusion coefficient that controls the ice propagation dynamics[2] , and ν is the kinematic viscosity of water. For the temperature range considered here, D_eff varies from 0 (for $T_\mathrm{s} \geq T_m$) to 1.04 $\mathrm{mm}^2.\mathrm{s}^{-1}$ (for $T_\mathrm{s} = -109°\mathrm{C}$). It reaches the same order than the kinematic viscosity of water, $\nu = 1\ \mathrm{mm}^2.\mathrm{s}^{-1}$. Thus, the ice and the viscous layers can be considered as boundary layers to the inviscid, ice-free flow.

Consequently, here we consider that the viscous boundary layer grows on top of the freezing layer, with a negligible coupling between them[3] . This configuration can be globally considered as a mixed boundary layer of size:

$$\delta = \delta_\nu + \delta_\mathrm{f} = \sqrt{\nu t} + \sqrt{D_\mathrm{eff}t}, \tag{3.13}$$

as shown in the schematic cross-section of the drop spreading and freezing Figure 3.10. As the liquid spreads, the viscous boundary layer of thickness δ_ν grows from the solid surface upwards, and concentrates the viscous dissipation. At the same time, the ice layer δ_f grows with a similar square-root-of-time dynamic. When the liquid freezes, it stops moving, which constitutes a loss of kinetic energy. Hence, both phenomena reduce the drop inertia. The dynamics of the two phenomena are associated and the damping operates across the thickness mixed boundary layer δ.

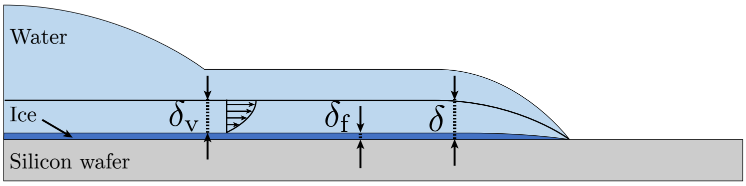

Figure 3.10: Schematic of a drop spreading and freezing on a cold substrate. Viscous damping occurs across the viscous boundary layer $\delta_\nu = \sqrt{\nu t}$, whereas the growing ice layer has thickness $\delta_\mathrm{f} = \sqrt{D_\mathrm{eff}t}$. As a results, the spreading is damped across a total thickness $\delta = \delta_\nu + \delta_\mathrm{f}$.

If we now assume that the spreading stops when the mixed boundary layer δ reaches the free surface, we obtain a similar result as in the non freezing case

[2] We recall that D_eff depends on the thermal properties of the ice and the substrate and is computed by solving Equation 3.5 with Equation 3.6.

[3] This uncoupling has been demonstrated in the related paper:
[31] Thiévenaz et al. (2020), *Subm. to Europhys. Lett.*, "Freezing-damped drop impact".

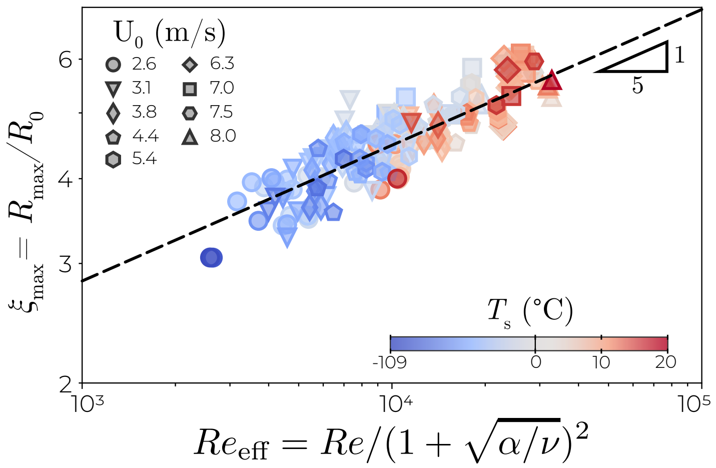

Figure 3.11: Maximal spreading versus the effective Reynolds number (Equation 3.15). The new definition of the Reynolds number shifts the experiments where freezing occurs (blue) to the left, and yields a good agreement with the power law 1/5. The dashed line has a slope 1/5 and its prefactor is fitted to the experiments above 0°C only.

(Equation 3.11), by defining the effective viscosity ν_{eff}, such as $\delta = \sqrt{\nu_{\text{eff}} t}$:

$$\nu_{\text{eff}} = \nu \left(1 + \sqrt{\frac{D_{\text{eff}}}{\nu}}\right)^2 . \tag{3.14}$$

Using ν_{eff}, we can define the effective Reynolds number Re_{eff}:

$$Re_{\text{eff}} = \frac{Re}{\left(1 + \sqrt{\frac{D_{\text{eff}}}{\nu}}\right)^2} . \tag{3.15}$$

Therefore, in the viscosity-dominated regime considered here, we expect the following spreading law:

$$\xi_{\max} \sim Re_{\text{eff}}^{1/5} .$$

Above 0°C, $D_{\text{eff}} = 0$ and thus $Re_{\text{eff}} = Re$, which returns the viscous scaling $\xi_{\max} = Re^{1/5}$. Below 0°C, the colder the temperature, the higher the freezing rate D_{eff}, the smaller the effective Reynolds number. With the aim of confronting this model against our experimental data, Figure 3.11 plots the maximal spreading parameter versus the effective Reynolds number. As in Figure 3.9 (c) the dashed line represents the power law $\xi_{\max} \sim Re_{\text{eff}}^{1/5}$ fitted with the experiments above 0°C, which remains unchanged. Only the points representing the experiments below 0°C have shifted to the left towards the small Reynolds numbers. There is now a good agreement between all data and the power law, for the whole range of temperature. This proves that the freezing of the spreading drop can be appropriately modelled through an effective viscosity, whose magnitude is set by the freezing rate.

Our results suggest moreover that the spreading law given by Equation 3.12 could be generalized to the case of sub-freezing substrate by redefining the effective impact parameter $P = WeRe_{\text{eff}}^{-2/5}$, leading to:

$$\xi_{\max} \sim Re_{\text{eff}}^{1/5} \frac{P^{1/2}}{A + P^{1/2}} , \tag{3.16}$$

Since our experiments are dominated by viscous damping, this expression does not provide a better fit to our data than the purely viscous $Re_{\text{eff}}^{1/5}$ law. Validating this expression would require more experiments and would deserve a dedicated study.

Finally, rather than an effect of solidification, the decrease of $\xi_{\max}$ with temperature could be due to the increase of viscosity of water depending on the temperature. Indeed, between 20°C and 0°C, the viscosity of water almost doubles, from 1 mPa.s to 1.79 mPa.s [111]. For the water viscosity to increase further below 0°C, it would need to be supercooled, otherwise it would just be solid. The viscosity of supercooled water does indeed increase at lower temperatures: at -20°C it is 4.33 mPa.s, more than twice its value at 0° [138]. However, it is unlikely that the temperature dependence of viscosity be the main cause for the damping for two reasons: firstly, we do not observe any decrease in the maximal spreading above 0°C, which could be attributed to the increase in the viscosity of water ; secondly, supercooled water does not exist below -40°C. This is contradictory with our observations which are consistent over the whole range of temperature from -109°C to 18°C.

[111] Lide (2005), , "CRC handbook of chemistry and physics".

[138] Hallett (1963), *Proceedings of the Physical Society*, "The temperature dependence of the viscosity of supercooled water".

3.6 Relaxation and solidifcation

The drop impacts, spreads, reaches its maximum diameter, and the frozen structure starts growing. This section is dedicated to predict the thickness h_p of the underlying layer of the frozen impacted drop (Figure 3.13).

This section is mainly extracted from: [30] Thiévenaz et al. (2019), *J. Fluid Mech.*, "Solidification dynamics of an impacted drop".

The stationary contact line (SCL) regime

As we observed in Figure 3.3 and we recall in Figure 3.12, after spreading, the contact line seems steady for a while, typically from (a) to (d), before a dewetting transition occurs leading to the retraction of the water film on the ice layer. It is thus expected that the thickness of the ice pancake h_p, whose definition is reminded in Figure 3.13, is built by thermal conduction during this time. Consequently, we need first to characterize the duration of this regime, that we call stationary contact line (SCL) regime [139]. Figure 3.14 (a) presents the variation of the liquid film radius during an impact, plotted as a function of time, for three different substrate temperatures. The dashed line shows the liquid drop radius evolution at room temperature and the two solid lines at freezing températur: -14°C and -30°C. Without freezing (dashed line), the drop spreads rapidly, reaches its maximal diameter and almost instantaneously retracts. The behaviour is different when the drop freezes. Indeed, after having reached its maximal diameter (illustrated on the curve with the inserts), the stationary contact line regime is observed: the liquid remains attached to the ice layer close to its maximum radius. There, the liquid radius barely varies with time during approximately $60 - 70$ ms before the retraction of the liquid film starts. This time between the spreading and the retraction regimes defines the SCL time: τ_{SCL}, as shown on the curves. We note that the two SCL times, for the two different temperatures, seem to be quite close.

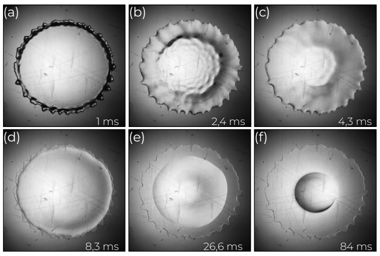

Figure 3.12: Images sequence of the impact of a water drop on a cold surface. From (a) to (d) defines the stationary contact line regime.

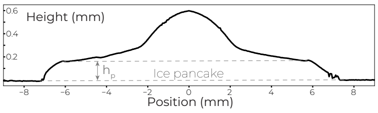

Figure 3.13: Height profile of a frozen drop, extracted from Figure 3.3 (e).

[139] Rivetti et al. (2015), *Soft Matter*, "Universal contact-line dynamics at the nanoscale".

Figure 3.14 (b) shows the dependence of the time τ_{SCL} with the temperature, for different heights of fall (indicated in the legend of (c)) and same drop size (1.9 mm) and substrate material (steel). We use $\Delta T = T_m - T_s$, where T_m is the freezing temperature of the liquid (for water $T_m = 0$°C so that $\Delta T = -T_s$), which is the relevant temperature here, because we saw that the energy needed to cool the drop down to T_m can be neglected. The first observation is that τ_{SCL} always reaches a plateau where it is independent of ΔT. The value of this plateau strongly depends on the drop impact velocity and thus on the initial spreading of the liquid film: the larger the maximal diameter at impact, the shorter the liquid layer stays stationary atop the ice

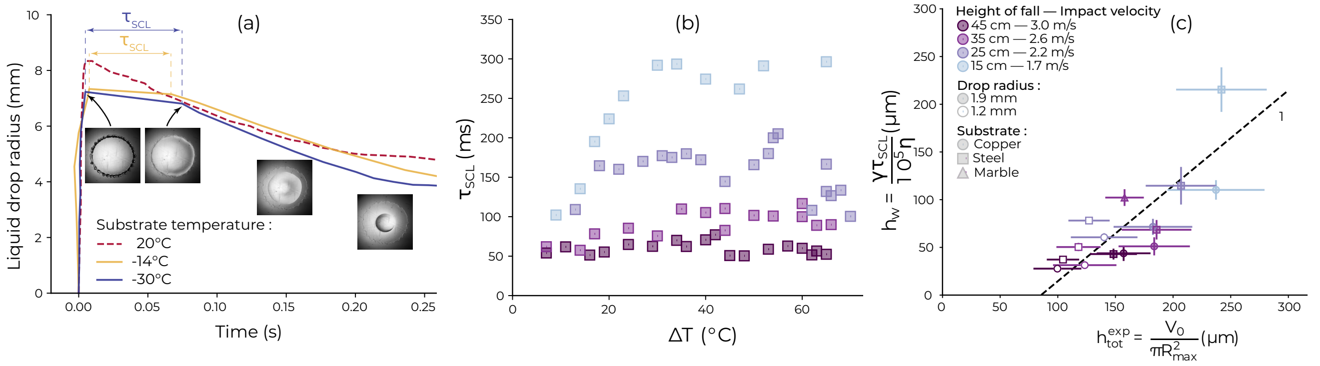

Figure 3.14: (a) The radius of the liquid film is plotted as function of time. Inset pictures show the aspect of the film on the different stages. (b) τ_{SCL} as a function of the temperature ΔT for different impact velocities indicated on the legend of (c). The drop radius is 1.9mm and the substrate is steel. (d) Theoretical prediction for the water film thickness h_w as a function of its experimental estimation $h_{\text{tot}}^{\text{exp}}$. Each point represents a series experiments with given impact velocity, substrate and drop radius as indicated in the legend. The error bars contain the variations within each series. The dashed line is a linear fit with the slope set to one.

pancake before retracting. These results suggest therefore that τ_{SCL} might be independent of the heat transfert and due to the sole liquid dynamics.

To explain the existence of this delay τ_{SCL} between spreading and retraction when water freezes, we will use an argument of a previous work, by Rivetti *et al.* [139], on the relaxation of a contact line pinned at the edge of a polymer film. Similarly, we assume here that the time τ_{SCL} is due to the relaxation dynamics of the contact angle θ formed by the liquid film and the growing ice pancake, and pinned at its edge. The contact line relaxation starts at an angle (θ_{init}) given by the spreading dynamics and ends when θ reaches a critical value θ^* enabling its depinning, required to its receding motion. This dynamics is schematized in Figure 3.15. In the experiment of Ref. [139], this angle is $\theta^* = 4.5° \pm 0.5°$ and surprisingly appears to be independent of the liquid and of the film thickness. Because the liquid film is very thin, its dynamics can be taken in the lubrication regime so that the contact line relaxation is expected to follow a capillaro-viscous relaxation time $t_w \propto (h_w\eta)/\gamma$, with the proportional coefficient being a function of θ^*, about 10^5 in their experiments. Note that, as soon as the contact line retracts, they showed that θ increases to a receding contact angle which stays roughly constant during dewetting.

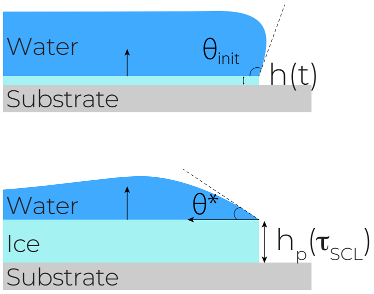

Figure 3.15: Schematic view of the stationary contact line regime during a drop impact on a cold substrate. The contact line relaxes from θ_{init} to θ^*, enabling the liquid film depinning.

In order to show that the same relaxation dynamics is at play in our experiments, we compare in Figure 3.14 (c) the characteristic thickness h_w of the liquid film that corresponds to the relaxation time τ_{SCL} following this capillaro-viscous dynamics, *i.e.* $h_w = \gamma\tau_{\text{SCL}}/(10^5\eta)$, and the characteristic thickness of the water film $h_{\text{tot}}^{\text{exp}}$ formed at the end of the spreading, neglecting ice formation: $h_{\text{tot}}^{\text{exp}} = V_{\text{tot}}/\pi R_{\text{max}}^2$ with V_{tot} the total volume of the drop and R_{max} the spreading radius. Remarkably, the experimental data gather along a line of slope 1, suggesting that this relaxation scenario of the contact line is correct. Note that, since $h_{\text{tot}}^{\text{exp}}$ corresponds to the total height of the spread drop, it is the sum of the ice pancake and the water film, so that the intersection of the dotted line with the x-axis gives a consistent estimation of the ice pancake thickness. We point out that the thicknesses of the ice and liquid layer are varying in time, so that $h_{\text{tot}}^{\text{exp}}$ is just a rough approximation of the liquid film thickness. This might explain the data scattering around the linear prediction. The fact that this dewetting angle θ^* appears to be almost independent on the substrates, the liquids and the film thicknesses, while our experiments and those of Ref. [139] concern film with totally different thickness, is a very interesting and intriguing result. It might shed light on an universal dewetting mechanism that should deserve specific investigations in the future.

Finally, following these results, the stationary contact line time (τ_{SCL}) varies linearly with the thickness of the liquid pancake at impact ($h_{\mathrm{tot}}^{\mathrm{exp}}$). As the spread drop diameter increases with the impact velocity, the liquid pancake is thinner and we understand the decrease of τ_{SCL} when the impact velocity increases, observed on Figure 3.14 (b). In this scenario, the thermal properties of the substrate plays no direct role, explaining thus the independence of τ_{SCL} with the temperature.

The ice pancake

At this point, we know the time during which the ice pancake (see Figure 3.16 (a) in the margin) is building (τ_{SCL}) and we have a validated model for the ice growth dynamics (D_{eff}); we now need the experimental measurements of the pancake thickness: h_p. Figure 3.16 (b)-(d) show the ice thickness h_p, deduced from the height profiles of the frozen drops (Figure 3.16 (a)), as a function of ΔT, respectively for four different drop impact velocities (b), three different substrates (c) and two different drop sizes (d). These control parameters, and their corresponding markers, are the same as those used in Figure 3.14.

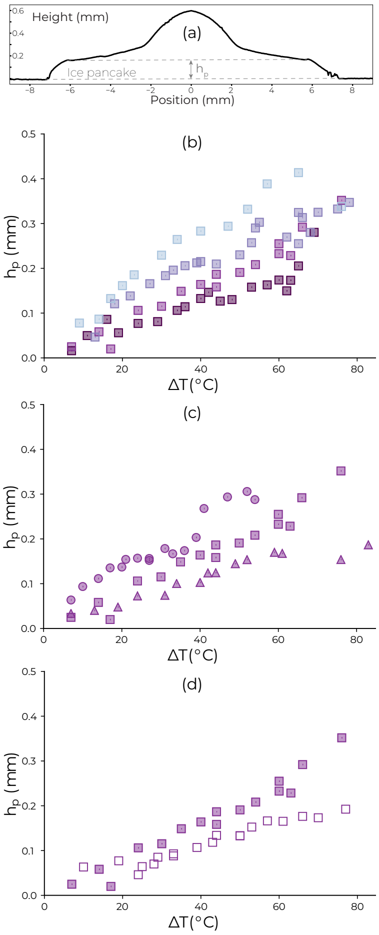

Figure 3.16: (a) Height profile of a frozen drop, extracted from Figure 3.3 (e). (b) Evolution of the underlying ice plate thickness h_p as a function of the temperature ΔT for different impact velocities, on the same substrate (steel) and with the same drop radius (1.9mm). (c) Evolution of h_p along ΔT, for different substrates, with the same impact velocity (2.6 m.s^{-1}) and drop radius (1.9 mm). (d) Evolution of h_p with ΔT for different drop radius, on the same substrate (steel) and at the same velocity (2.6 m.s^{-1}).

These graphs show that the underlying ice layer becomes thicker when: *(i)* the substrate is colder (Figure 3.16 (b), (c) and (d)); which is expected since more liquid can be frozen during the solidification time that appeared to be mostly constant with ΔT (Figure 3.14 (b) and (c)). *(ii)* The substrate heat conductivity increases (Figure 3.16 (c)): the heat is indeed transferred to the substrate with higher efficiency, so that the freezing front can propagate faster during a solidification time that, again, does not vary much (Figure 3.14 (d)). *(iii)* The drop impact velocity is slower (Figure 3.16 (b)), or the drop size is smaller (Figure 3.16 (d)), because the spread drop stays freezing longer before retracting (Figure 3.14 (b) and (c)).

We can now compare our experimental results to our theoretical model. Figure 3.17 presents the variation of $h_p^2/\tau_{\mathrm{SCL}}$, which represents the experimental diffusion coefficient of the solidification front, as a function of the theoretical diffusion coefficient D_{eff}, for all the substrate materials, substrate temperatures, drop sizes and impact velocities investigated experimentally. The substrate temperature ranges from -5°C to -80°C, which yields the Stefan number ranging from approximately 10^{-2} to 1. We observe a nice collapse of all the data into a straight line of slope 1. We can therefore conclude that the ice pancake thickness is well described by the expression:

$$h_p^2 \simeq D_{\mathrm{eff}} \tau_{\mathrm{SCL}}.$$

This indicates clearly that our simplified 1D model describes correctly the dynamics, and that the ice pancake formation is controlled by the thermal diffusion during the depinning time of the remaining liquid film (τ_{SCL}).

We observe that some experiments are not collapsing on the line with the others. They appear particularly for an effective diffusive coefficient greater than 3.10^{-7} m^2.s^{-1}. This limit of our model probably comes from the hypothesis of semi-infinite water in the freezing model. Indeed, if we estimate the thickness of the water film at impact $h_{\mathrm{tot}}^{\mathrm{exp}}$ with the drop volume V_{tot} and the spreading radius R_{max}, we find $h_{\mathrm{tot}}^{\mathrm{exp}} \sim V_{\mathrm{tot}}/\pi R_{\mathrm{max}}^2 \sim 200\mu$m, with a drop of volume

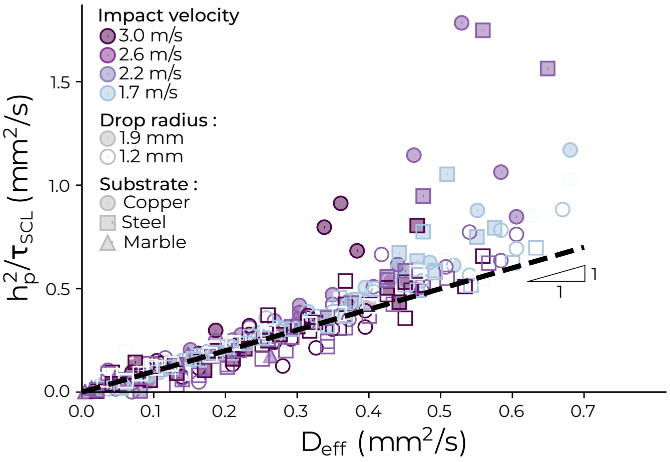

Figure 3.17: Rescaling of the measurements against the model: the measured diffusivity of the solidification front, h_p^2/τ_{SCL} is plotted against the effective diffusion coefficient D_{eff} (see Equation 3.1). It shows a good collapse for all experiments, regardless of the substrate (symbols), impact velocity (colour) or drop size (full or empty symbols). The dashed line has a slope 1.

$V_{\text{tot}} = 30\mu$L spreading to a radius of $R_{\max} = 7$mm. This thickness is smaller than the highest values of h_p, meaning that almost the whole water drop freezes during τ_{SCL} and the hypothesis of semi-infinite water does not hold anymore.

3.7 Retraction and pattern formation

Now that the formation of the underlying ice pancake has been understood and the ice structure properly characterized, the present section will be dedicated to rest of the frozen drop, namely the intermediate zone and the pattern on the top (see Figure 3.3). In order to understand these complex shapes, the behavior of a water film on ice has to be clarified, in particular its retraction and wetting dynamics. Even though it has been the focus of a few studies [140, 141], water capillary dynamics on ice still remains a highly complex subject. In particular because of the disordered quasi-liquid layer on top of the surface of ice [142–145].

This section is mainly extracted from: [32] Thiévenaz et al. (2020), *Phys. Rev. Fluids*, "Retraction and freezing of a water film on ice".

Let us first consider the retraction of the water film on the ice disc. Similarly to Figure 3.14 (a), Figure 3.18 (a) presents the film radius versus time, it shows in particular that the retraction velocity V_{ret} is constant during most of the retraction. Subsequently, the retraction velocity is plotted in Figure 3.18 (b) for each experiment versus $\Delta T = T_m - T_s$, with T_m the melting temperature – 0°C in our case – and T_s the substrate temperature. We observe that V_{ret} is roughly the same for any value of the control parameters, represented by different markers: it does not vary with impact velocity, drop radius, substrate material and temperature. Hence, we deduce the retraction velocity of water on ice:

$$V_{\text{ret}} \simeq 17 \pm 3 \text{ mm.s}^{-1}. \tag{3.17}$$

Yet, those control parameters do have an effect on the thickness of the liquid film which retracts on ice, which means that V_{ret} does not depend on the film thickness. As the film thickness appears in the Taylor-Culick velocity [146] ($\sqrt{\gamma/(\rho h_f)}$), this observation suggests that the capillary retraction is here balanced by viscosity, rather than by inertia.

[140] Knight (1971), *Philosophical magazine*, "Experiments on the contact angle of water on ice".
[141] Petrenko et al. (1999), , "Physics of ice".

[142] Frenken et al. (1985), *Physical review letters*, "Observation of surface melting".
[143] Lied et al. (1994), *Phys. Rev. Lett.* "Surface Melting of lce lh Single Crystals Revealed by Glancing Angle X-Ray Scattering".
[144] Li et al. (2007), *The Journal of Physical Chemistry C*, "Surface premelting of ice".
[145] Sazaki et al. (2012), *Proceedings of the National Academy of Sciences*, "Quasi-liquid layers on ice crystal surfaces are made up of two different phases".
[146] F.E.C. Culick (1960), *J. Appl. Phys.* "Comments on a ruptured soap film".

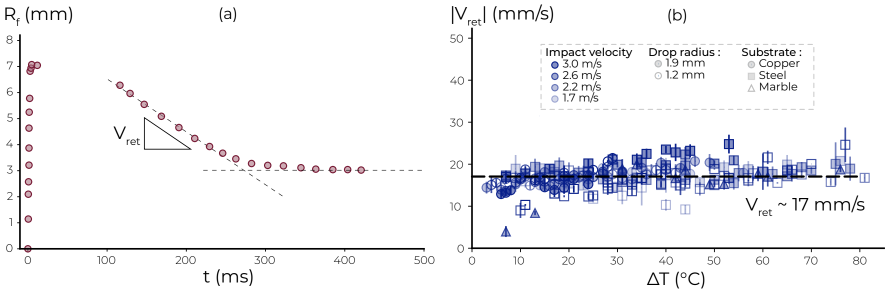

Figure 3.18: (a) Time evolution of the liquid film radius R_f for a single experiment. R_f decreases linearly during the retraction, therefore pointing at a constant retraction velocity V_ret. (b) Retraction velocity of the water film on ice, as a function of $\Delta T = T_m - T_s$, for a large set of experiments with a Weber number ranging from 48 to 234.

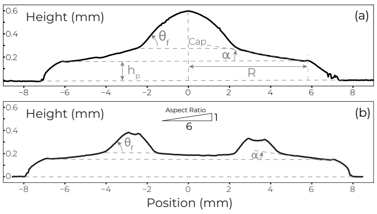

Figure 3.19: Height profiles of the two ice structures. They are referred as *cap* and *ring* patterns. Extracted from Figure 3.3.

In our experiment the ice keeps growing as long as there is water on it, so that the liquid film freezes as it retracts. The interplay between capillary retraction and solidification therefore controls the final shape of the frozen drop, and may be characterized by comparing the dynamics of both processes, which we do through scaling laws. Knowing the growth dynamics of ice ($h(t) = \sqrt{D_\mathrm{eff} t}$), we can determine the solidification velocity V_sol ($dh/dt = \sqrt{D_\mathrm{eff}}/(2\sqrt{t})$) at the moment water starts retracting ($t = h_\mathrm{p}^2/D_\mathrm{eff}$):

$$V_\mathrm{sol} = \frac{D_\mathrm{eff}}{2h_\mathrm{p}} \tag{3.18}$$

Figure 3.20 (a) shows the variation of $\tan(\alpha)$ (see Figure 3.19) versus the ratio of the solidification and retraction velocities, for all our experiments. All the data gather along a line $\tan(\alpha) \simeq 0.67 V_\mathrm{sol}/V_\mathrm{ret}$, which demonstrates that the ice slope α is indeed the result of the balance between vertical solidification and radial retraction. The lesser-than-one 0.67 factor is probably due to an overestimation of V_sol, as it is defined at the beginning of the retraction whereas the real instant velocity decreases over time.

Now, we question the mechanism that select the final pattern: *cap* (Figure 3.19 (a)) or *ring* (Figure 3.19 (b)). We observe on the timelines (Figure 3.3 (a)&(b)) that during the relaxation of the contact line (between the second and the fourth image, schematized by the transition from Figure 3.3 (c) to (d)), a rim appears at the edge of the liquid film creating a trough at the center [139, 147]. When this film with a curved free surface retracts two options exist: either the freezing rate is slow compared to the retraction and the rim will eventually collapse into a cap shape, either the freezing is quick enough to reach the trough before the rim collapses, in which case a liquid ring is left to freeze, yielding the ring shape. In order to study the transition from one shape to another, the timescales of retraction τ_ret and solidification τ_sol can be estimated using the characteristic lengths R (see Figure 3.19 (a)) and h_f, respectively the liquid film radius and thickness at

[139] Rivetti et al. (2015), *Soft Matter*, "Universal contact-line dynamics at the nanoscale".
[147] Edwards et al. (2016), *Science Advances*, "Not spreading in reverse: The dewetting of a liquid film into a single drop".

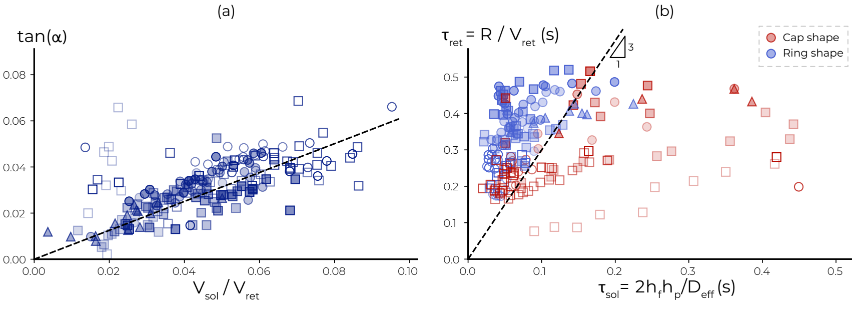

Figure 3.20: (a) Tangent of α as defined in Figure 3.19, versus $V_\mathrm{sol}/V_\mathrm{ret}$.The legend is the same as in Figure 3.18 (b). The dashed line is the best linear fit, the slope is 0.67. (b) Phase diagram of the final shapes: *cap* in red and *ring* in blue (see Figure 3.3 (a) &(b)), depending on τ_sol and τ_ret. The symbols shape and opacity represents the impact and freezing parameters, according to Figure 3.18 (b) legend. The dashed line is to guide eye.

the onset of retraction, measured from the thickness profiles[4] , yielding:

$$\tau_{\mathrm{ret}} = \frac{R}{V_{\mathrm{ret}}} \quad \text{and} \quad \tau_{\mathrm{sol}} = \frac{h_{\mathrm{f}}}{V_{\mathrm{sol}}} = \frac{2h_{\mathrm{f}}h_{\mathrm{p}}}{D_{\mathrm{eff}}} \tag{3.19}$$

Figure 3.20 (b) is a phase diagram that plots the timescales τ_{ret} versus τ_{sol} for our large range of control parameters values (see legend in Figure 3.18 (b)), by distinguishing the cap, in red, and ring, in blue. We obtain a clear separation between the two shapes, shown with a dashed line, validating the proposed mechanism of pattern selection. The dashed line has a slope of 3, larger than 1, which may be explained through two distinct contributions: the use of the film radius R that overestimates τ_{ret} since the film only retracts on a fraction of it, and the previously described overestimation of V_{sol} which translates into an underestimation of τ_{sol}.

The main exception to our criterion concerns the group of empty red markers in the lower left part of Figure 3.20 (b), which represents a series of impacts with small drops yielding a cap shape (red) whereas they should yield a ring shape (blue). This mismatch can be understood as the effect of the small width of the retracting liquid film which results from the impact of smaller drops: if the film is not spread enough no rim will form, and therefore no ice ring will freeze whatever the solidification time. However, although this explanation qualitatively explains our data, we have unfortunately not been able to find a simple criterion quantifying the minimal size required to form a retraction rim.

Either way, the scaling analyses presented in Figure 3.20 prove that the final shape of the frozen drop, be it the angle α or the pattern, ring or cap, is entirely defined by the competition between retraction and solidification. Note that another shape with two concentric rings instead of one can been observed, but this configuration is the result of the same mechanism that forms one ring.

Water-ice contact angle

Finally, this experiment provides an original way to progress on the wetting of water on ice. Indeed, the angle θ_{f} defined on Figure 3.19 or Figure 3.3 is related to the contact angle that water made with ice at the moment it has been frozen, even if it probably only gives an indirect measurement of the real contact angle. Indeed, the density variation during solidification might change this angle. Moreover, we may wonder whether the solid-liquid interface is horizontal during the solidification, although it seems supported by the simple relation between $\tan\alpha$, V_{ret} and V_{sol} seen in Figure 3.20 (a).

Figure 3.21 presents the variation of θ_{f} for all our experiments, versus the ratio of the characteristic times of solidification τ_{sol} and retraction τ_{ret}. We first observe a whole range of θ_{f} from less than one degree up to about fifteen degrees in the ring configuration ($\tau_{\mathrm{ret}} > 3\tau_{\mathrm{sol}}$), when the film is solidified while it is retracting. Note that, as the retraction velocity is constant (Figure 3.18), we would expect a constant value of the corresponding retraction angle that we do not observe on this graph. Indeed, in this case the receding contact line is frozen by the solidification front before water reached an equilibrium shape. Consequently, one should expect a strong modification of the water-ice angle due to capillary relaxation of the remaining liquid being faster than the solidification front propagation. This relaxation dynamics while freezing explains the difference between θ_{f} and the real contact angle, and

[4] The water film thickness at the onset of retraction h_f is estimated using the height profiles. Since the ice thickness at the same moment h_p can be easily measured, one may integrate the part of the profiles that is greater than h_p so as to obtain the volume of ice that froze after retraction started. By dividing this volume by the surface of the film πR^2 and correcting it by the density ratio of water and ice, we obtain the estimation of the water film thickness h_f.

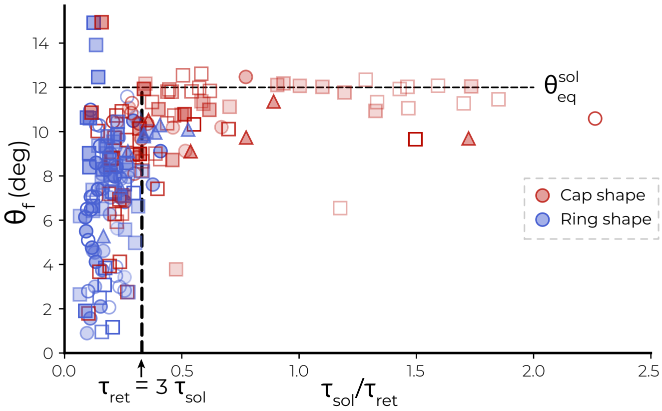

Figure 3.21: Final contact angle θ_f of the retracting water film on ice versus the ratio of the characteristic times of solidification and retraction: $\tau_\mathrm{sol}/\tau_\mathrm{ret}$. The vertical dashed line shows threshold that delimited the two ice shapes: $\tau_\mathrm{ret}/\tau_\mathrm{sol} = 3$, as in Figure 3.20 (b). The symbols shape and opacity represents the impact and freezing parameters, according to Figure 3.18 (b) legend.

this difference should depend on the experimental parameters and is difficult to predict. However, when the water film has time to form an equilibrium spherical cap before being frozen ($\tau_\mathrm{ret} < 3\tau_\mathrm{sol}$), its contact angle with the ice always reaches a constant limit value, for any control parameters. Depending whether a contact angle hysteresis exists or not [148], this particular angle may be an equilibrium angle or a retraction angle, but in either case it exists, it is unique and constant. Its value when solidified is called the *solidified equilibrium angle* $\theta_\mathrm{eq}^\mathrm{sol}$.

Despite the difference between the real contact angle and θ_f, it is interesting to compare our value $\theta_\mathrm{eq}^\mathrm{sol} \sim 12°$ with those reported previously in the literature. In fact, to our knowledge, only few studies have studied the ice-water contact angle and their results span a large range from 1° up to 40° [111, 114–116, 140, 141, 149, 150]. Knight [114] notably measured 12° in 1966 for the receding contact angle of water on ice by observing the retraction of a freezing puddle. On the other hand, as the interfacial tension between ice and water is very low due to their high affinity [116], Young's relation imposes that a non-zero contact angle of water on ice is equivalent to a surface free energy of ice lower than the surface tension of water at 0°C, 75.6 mJ.m^{-2} [111]. Van Oss *et al.* [116] found accordingly that the surface free energy of ice is 69.2 mJ.m^{-2}, which puts the contact angle of water on ice around 24°. Our value of $\theta_\mathrm{eq}^\mathrm{sol}$ is therefore consistent with this range of value, but still does not help to discriminate between the preceding observations. However, if the relation between our solid equilibrium contact angle $\theta_\mathrm{eq}^\mathrm{sol}$ and the real ice-water contact angle can be estimated by further research, this experiment would provide a new value of the contact angle of water on ice.

[148] Bonn et al. (2009), *Rev. Mod. Phys.* "Wetting and spreading".

[114] Knight (1966), *Journal of Colloid and Interface Science*, "The contact angle of water on ice".
[149] Ketcham et al. (1969), *Philosophical Magazine*, "An experimental determination of the surface energies of ice".
[140] Knight (1971), *Philosophical magazine*, "Experiments on the contact angle of water on ice".
[116] Van Oss et al. (1992), *Journal of adhesion science and technology*, "Surface tension parameters of ice obtained from contact angle data and from positive and negative particle adhesion to advancing freezing fronts".
[115] Makkonen (1997), *The Journal of Physical Chemistry B*, "Surface melting of ice".
[141] Petrenko et al. (1999), , "Physics of ice".
[150] Drelich et al. (2011), *Soft Matter*, "Hydrophilic and superhydrophilic surfaces and materials".
[111] Lide (2005), , "CRC handbook of chemistry and physics".

3.8 Crack patterns

As it is illustrated by the image on the front page, fractures can form on the frozen drop. This last section aims at shedding light on the different crack patterns that we observe and on the mechanisms behind their appearance.

This section is mainly extracted from: [30] Ghabache et al. (2016), *Physical Review Letters*, "Frozen impacted drop: From fragmentation to hierarchical crack patterns ".

Introduction

When molten glass drips into cold water, the outside cools - and shrinks - faster than the inside, creating pent-up tension in the so-called Prince Rupert's drop, known since before 1625 to have very striking mechanical properties [151, 152]. Indeed, while the drop's head stays impervious to even

[151] Merrett (1662), , "The Art of Glass".
[152] Chandrasekar et al. (1994), *Philos. Mag. Part B*, "The explosive disintegration of Prince Rupert's drops".

the strongest blows, flick the tail and the whole drop shatters in a myriad of small pieces, in less than a millisecond. In the same way, fragmentation is in fact present in many physical processes, from jet atomization to bubble bursting in fluids [153, 154], from spaghetti breaking [155] to popping balloons [156] or broken windows in solids [157]. It is related to diverse applications such as shell case bursting [158], ash generation during eruption [159], cooling lava [160] or meteoric cratering [161] for instance.

Fragmentation is thus a sudden process, where the whole considered domain divides extremely rapidly. At least as ubiquitous, there exists a complete different crack morphology where space-dividing pattern shows a strong hierarchy of slower fractures [162]. Fractures develop successively, and each new fracture joins older fractures at a typical angle close to ninety degrees [163]. Such patterns are usually observed when the shrinking of a material layer is frustrated by its deposition on a non shrinking substrate, such as drying-induced cracks in mud [164, 165], coffee [166], colloidal silicas [167], industrial coating [168] or artistic painting [169].

In this last section, we investigate experimentally the quenching of our frozen drop. We show how, as a function of the substrate temperature, the crack patterns produced by the thermal shock, change from a 2D fragmentation regime to a hierarchical fracture regime (Figure 3.22 (a)).

Qualitative description

Throughout all this last section, the drop radius and the falling height will be kept constant, respectively R =1.9 mm and H = 35 cm. The substrate is stainless steel. Figure 3.22 (b) and (c) present time sequences, for different substrate temperatures, respectively -31°C and -60°C. In Figure 3.22 (b) we find again the behaviour we have described in the previous sections with, in particular, the formation of a ring on an ice pancake. After the whole pancake is frozen (t $\sim$ 500ms) it keeps cooling. It is therefore shrinking, but the adhesion to the solid substrate limits this ice contraction. This frustration causes mechanical tensions that are suddenly relaxed by the formation of a pattern of fractures. This remarkable dynamics, called fragmentation, is a 2D equivalent to the Prince Rupert's drops shattering, described in the introduction. This solid fragmentation seems to propagate radially from a nucleation point. Experimental estimation gives a high front propagation velocity, typically between 800 and 1000 m.s^{-1}, which is a fraction of the Rayleigh wave speed.

Figure 3.22 (c) presents the same drop impact experiment but on even colder substrate (-46°C). In this case, shortly after the drop has pinned, while ripples are still visible, first fractures are observed on a growing ice layer (t $\sim$ 28 ms). Then more cracks propagate, hierarchically, by successive division of the frozen drop. The crack pattern is here typical of hierarchical fractures [162], with younger crack joining the older one at an angle close to 90°. The domains are larger and consequently less numerous than in the fragmentation regime. Note that, if this particular cracking dynamics is very similar to what is observed in the case of desiccation [166], here the time scales are much shorter.

To summarize the qualitative description of our experiment, the main different patterns are shown in Figure 3.22 (a) as a function of the temperature difference $\Delta T = T_m - T_s$, where T_s is the substrate temperature and $T_m =$ 0°C is the water freezing temperature. They are gathered in three different regimes:

[153] Marmottant et al. (2004), *Phys. Fluids*, "Fragmentation of stretched liquid ligaments".

[154] Villermaux (2007), *Annu. Rev. Fluid Mech.* "Fragmentation".

[155] Audoly et al. (2005), *Phys. Rev. Lett.* "Fragmentation of Rods by Cascading Cracks: Why Spaghetti Does Not Break in Half".

[156] Moulinet et al. (2015), *Phys. Rev. Lett.* "Popping Balloons: A Case Study of Dynamical Fragmentation".

[157] Vandenberghe et al. (2013), *Soft Matter*, "Geometry and fragmentation of soft brittle impacted bodies".

[158] Wittel et al. (2004), *Phys. Rev. Lett.* "Fragmentation of shells".

[159] Kokelaar (1986), *Bulletin of Volcanology*, "Magma-water interactions in subaqueous and emergent basaltic".

[160] Goehring et al. (2009), *Proc. Natl. Acad. Sci.* "Nonequilibrium scale selection mechanism for columnar jointing".

[161] Sagy et al. (2004), *J. Geophys. Res.: Solid Earth*, "Shatter cones: Branched, rapid fractures formed by shock impact".

[162] Bohn et al. (2005), *Phys. Rev. E*, "Hierarchical crack pattern as formed by successive domain divisions. I. Temporal and geometrical hierarchy".

[163] Shorlin et al. (2000), *Phys. Rev. E*, "Development and geometry of isotropic and directional shrinkage-crack patterns".

[164] Kindle (1917), *The Journal of Geology*, "Some factors affecting the development of mud-cracks".

[165] Korvin (1989), *Pure Appl. Geophys.* "Fractured but not fractal: Fragmentation of the gulf of suez basement".

[166] Groisman et al. (1994), *Europhys. Lett.* "An experimental study of cracking induced by desiccation".

[167] Pauchard et al. (1999), *Phys. Rev. E*, "Influence of salt content on crack patterns formed through colloidal suspension desiccation".

[168] Xu et al. (2009), *Drying Technology*, "Drying-induced cracks in thin film fabricated from colloidal dispersions".

[169] Pauchard et al. (2007), *Reflets de la Physique*, "Craquelures dans les couches picturales des peintures d'art".

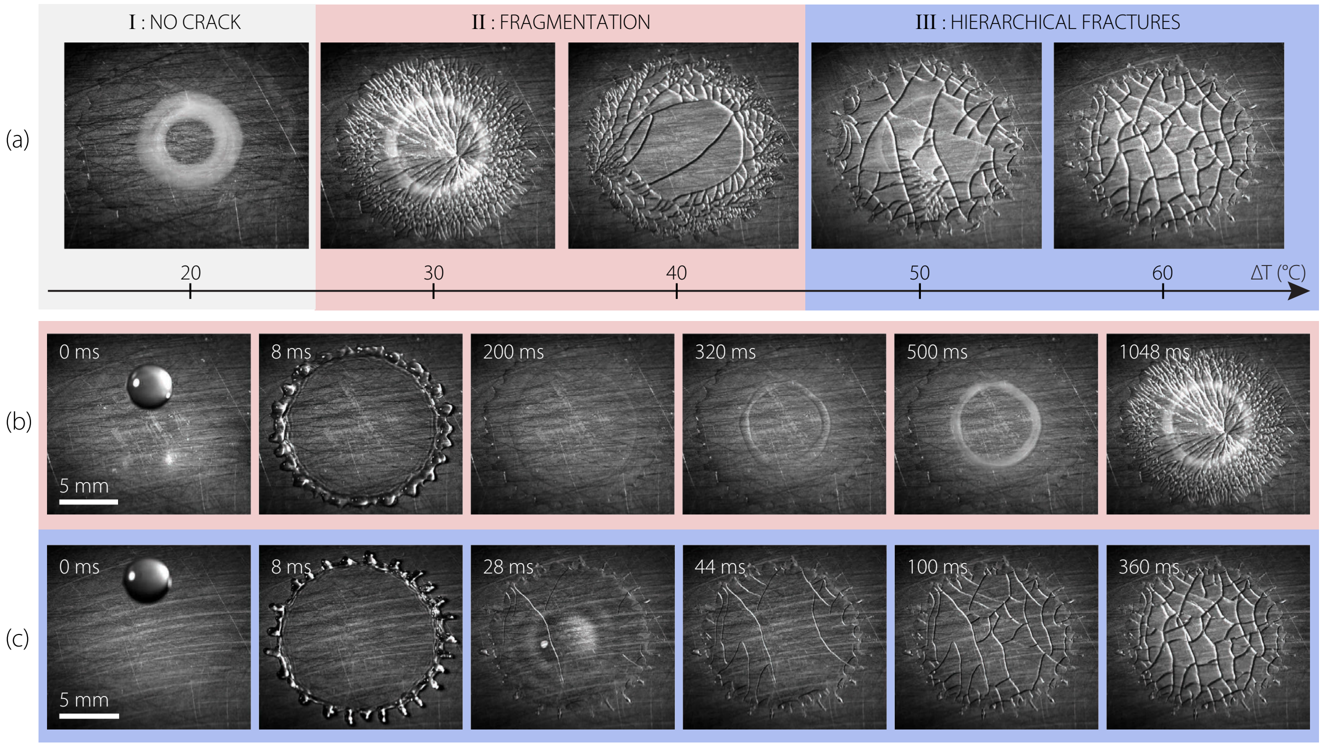

Figure 3.22: (a) Frieze presenting snapshots of the frozen pancakes formed after a water drop impacted, from a falling height $H = 36$ cm, a cold substrate at various temperature $T_s = -20.0°$, $-31.1°$, $-41.2°$, $-50.3°$ and $-59.6°$C from left to right (with $\Delta T = -T_s$). Depending on ΔT the frozen pancake presents different crack patterns that can be gathered into three different regimes: I - no cracks, II - fragmentation regime, III - hierarchical fractures regime. The transition temperatures are: $\Delta T^{(\mathrm{exp})}_{\text{I-II}} \sim 25°$C and $\Delta T^{(\mathrm{exp})}_{\text{II-III}} \sim 42°$C. (b) Sequence showing the drop impact and solidification dynamics preceding the fracture pattern observed on the second image of the frieze (a): $T_s = -31.1°$C. (c) Sequence preceding the fracture pattern observed on the fifth image of the frieze (a): $T_s = -59.6°$C. On these two sequences, the time and the scale bar are on the images.

- I: at low ΔT, the solid pancake remains smooth, no cracks are present.
- II: the fragmentation regime, at intermediate ΔT, the cracks appear suddenly from a nucleation point.
- III: the hierarchical regime, at high ΔT, the cracks are formed step by step.

The two sequences described above, Figure 3.22 (b) and (c), belong respectively to the beginning of regime II and the end of regime III. We observe that, close to the transition between the regimes, intermediate cases appear, with fragmentation only on the edge of the pancake or mix between fragmentation and hierarchical fractures. It is also worth emphasizing that while the fragmentation occurs after the whole pancake has solidified, the hierarchical cracks are usually formed during the solidification phase. Finally, this experiment is, to our knowledge, the first example where it is possible to pass continuously from a fragmentation to a hierarchical regime using a simple control parameter. Thermal shock in ceramic [170, 171] might have comparable behavior, but this has not been observed so far.

[170] Korneta et al. (1998), *Physical Review E*, "Topological and geometrical properties of crack patterns produced by the thermal shock in ceramics".
[171] Lahlil et al. (2013), *The Old Potter's Almanack*, "Crack patterns morphology of ancient Chinese wares".

Griffith length and frozen pancake thickness

These different regimes can be understood using classical fracture arguments [172]: indeed, since the freezing of the liquid is at 0°C, the new solid is submitted to a rapid thermal contraction as substrate temperature is below. If the ensuing deformation energy is high enough, fractures can appear in the

[172] Freund (1990), , "Dynamic Fracture Mechanics".

frozen pancake. This mechanism can be quantified using energy balance [173, 174]: we assume a linear isotropic elastic behavior of ice, with a Young's modulus $E = 9.33$ GPa. Its thermal contraction induces a deformation tensor field $\epsilon_{th}(\mathbf{x}, t) = \alpha \delta T \mathbf{I}$ where $\alpha = 5.3 \cdot 10^{-5}\,\mathrm{K}^{-1}$ is the ice thermal expansion coefficient taken constant here [141], $\mathbf{I}$ the identity tensor and $\delta T = T_m - T(\mathbf{x}, t)$, with $T(\mathbf{x}, t)$ the local time-dependent temperature in the ice domain. The density of elastic energy induced by this thermal contraction reads therefore $\mathcal{E} = \frac{3}{2} E \alpha^2 \delta T^2$.

[173] Adda-Bedia et al. (1996), *Physical Review E*, "Morphological instabilities of dynamic fractures in brittle solids".
[174] Bourdin et al. (2014), *Physical review letters*, "Morphogenesis and propagation of complex cracks induced by thermal shocks".
[141] Petrenko et al. (1999), , "Physics of ice".

A fracture in a brittle material consists in the formation of a new interface, associated to an energy per unit surface, the so-called Griffith energy, $G_c \simeq 1\ \mathrm{kg} \cdot \mathrm{s}^{-2}$ [175]. Balancing the elastic energy due to the thermal contraction of a cubic ice of length L_c, with homogeneous temperature T_s, $3E(\alpha \Delta T)^2 L_c^3/2$, with the energy of a crack breaking the cube in two part $2 G_c L_c^2$, leads to the introduction of the Griffith length (see Figure 3.23):

[175] Schulson et al. (2009), , "Creep and fracture of ice".

$$L_c = \frac{4 G_c}{3 E \alpha^2 \Delta T^2}. \tag{3.20}$$

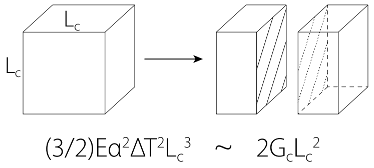

Figure 3.23: Small shrunk cubic ice (length Lc) with homogeneous temperature Ts breaks into 2 stress free pieces.

Above this typical length, breaking the shrunk solid becomes energetically favorable.

This length should be compared to the typical thickness of our pancake. For the sake of simplicity, we will not consider the complex shape of the frozen drop we described in the last section. We consider the simplest definition of the liquid pancake thickness: $h_{\text{tot}} = V_{\text{tot}}/\pi R_{\text{max}}^2$ with V_{tot} the total volume of the drop and R_{max} the spreading radius, and we will take the same shape for the frozen pancake. Three regimes can therefore be identified in the crack formation, depending on the ratio between the Griffith length L_c and the typical height h_{tot} of the liquid pancake [176]. If $h_{\text{tot}} \ll L_c$, no crack formation is expected by the thermal shock, this first regime is observed on the first image of Figure 3.22 (a). On the other hand, for $h_{\text{tot}} \gg L_c$ one expects that the cracks appear before the whole solidification of the pancake, when a solid ice layer of thickness of the order of L_c is formed. This is the behaviour observed on Figure 3.22 (c) and therefore corresponding to regime III. In between, for $h_{\text{tot}} \sim L_c$, one expects the cracks to be formed when the whole pancake is solid and we identified this latter behaviour with the regime II (Figure 3.22 (b)) where the frozen pancake fragments into a myriad of small pieces of typical size h_{tot} [162].

[176] Gauthier et al. (2010), *Europhysics Letters*, "Shrinkage star-shaped cracks: Explaining the transition from 90 degrees to 120 degrees".

[162] Bohn et al. (2005), *Phys. Rev. E*, "Hierarchical crack pattern as formed by successive domain divisions. I. Temporal and geometrical hierarchy".

The fragmentation regime

Let us start by estimating the appearance temperature of the first cracks at the frontier between regime I and II, $\Delta T_{\text{I-II}}$. Energy balance imposes that the total elastic energy in the frozen pancake is greater than the surface energy of all the fractures, namely:

$$\frac{3}{2} E \alpha^2 \Delta T^2 \pi R_{\text{max}}^2 h_{\text{tot}} \geq 4 \frac{\pi R_{\text{max}}^2}{h_{\text{tot}}^2} G_c h_{\text{tot}}^2,$$

where the ratio $\pi R_{\text{max}}^2 / h_{\text{tot}}^2$ is the number of pieces of typical size h_{tot} formed by the fragmentation (see Figure 3.24). It leads to the relation:

$$\Delta T^2 \geq \Delta T_{\text{I-II}}^2 = \frac{8 G_c}{3 E \alpha^2 h_{\text{tot}}}. \tag{3.21}$$

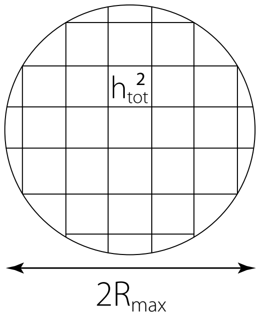

Figure 3.24: Scheme of the fractured frozen pancake in the fragmentation regime.

With, for $\Delta T > \Delta T_{\text{I-II}}$ cracks are energetically favorable while no cracks should be observed otherwise. At this transition temperature the pancake thickness is then found to be twice the Griffith length. In this experimental setup the maximum spreading radius is around 8 mm and the initial drop radius is 1.9 mm. By taking the pancake thickness $h_{\text{tot}} = V_{\text{tot}}/\pi R_{\text{max}}^2$ and the values of E and G_c given above, we end up with $\Delta T_{\text{I-II}} \sim 27°\text{C}$, which is in perfect excellent with the experimental transition temperature to fragmentation $\Delta T_{\text{I-II}}^{(\text{exp})} (\sim 25°\text{C})$ (Figure 3.22).

The hierarchical regime

When $h_{\text{tot}} \gg L_c$, fractures can form before the full solidification of the liquid pancake and we identify there the regime III, where the cracks appear step by step. In this case, the solid layer of thickness $h(t)$ grows with time as the pancake freezes, while the liquid temperature is considered constant and equal to T_m. We are in the configuration of Section 3.4. But here, in this regime that takes place at cold temperature, the Stefan number is smaller than one, typically around 0.3 (see note in the margin). We are in the configuration where the diffusion process is always faster than the solidification dynamics. Moreover, the substrate here has a high effusivity, the ratio of effusivity is therefore smaller than one, typically around 0.3. In other word, the temperature at the interface is close to the substrate temperature. Consequently, as $\text{St} \simeq 0.3 < 1$ and $\frac{e_i}{e_s} \simeq 0.3 < 1$, the asymptotic behaviours of Equation 3.8 applies, which gives the following time evolution for the ice layer:

$\text{St} = \frac{\text{C}_{pice}\Delta\text{T}}{\text{L}}$
$\text{L}=333.5 \cdot 10^3\ \text{J.kg}^{-1}$
$\text{C}_{pice}=2110\ \text{J.kg}^{-1}.\text{K}^{-1}$
$\text{e}_{\text{ice}} = 2000\ \text{J.K}^{-1}.\text{m}^2.\text{s}^{-1/2}$
$\text{e}_{\text{steel}} = 7000\ \text{J.K}^{-1}.\text{m}^2.\text{s}^{-1/2}$

$$h^2(t) \sim \text{St} D_i t,$$

with $h(0) = 0$. Considering that the formation of the first crack happens when $h(t_c) \propto L_c$ Equation 3.20, it gives the following temperature dependance for the time of cracks appearance in regime III:

$$t_c \propto \frac{1}{\Delta T^5}. \tag{3.22}$$

This first crack time t_c has been measured for all our experiments, varying both the impact velocity and the substrate temperature and is shown on figure 3.25. The closed triangles correspond to the appearance of the first crack in regime III, in reasonable agreement with the ΔT^{-5} variation predicted by the Equation 3.22, plotted with a dashed line. This confirms our model

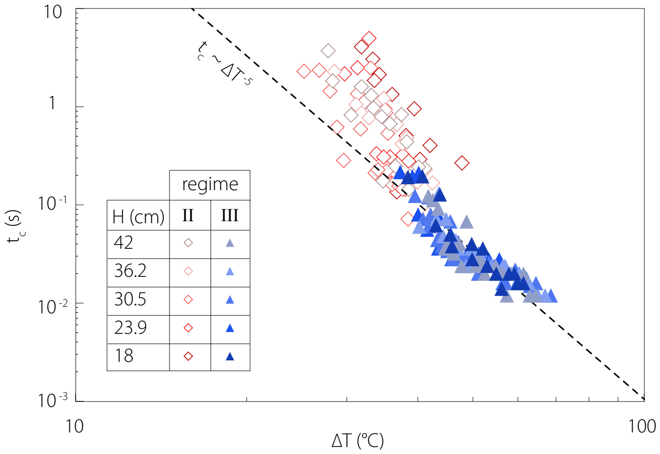

Figure 3.25: Appearance time of the first crack, t_c, plotted as function of $\Delta T = T_0 - T_s = -T_s$ with T_s the substrate temperature, for five different falling heights of the impacting drop. t_c is determined considering initial time when drop reached its maximum spreading diameter after impact. The open diamonds correspond to the fragmentation regime (II) while the closed triangles correspond to the hierarchical fracture regime (III). The dashed line, representing $t_c \propto \Delta T^{-5}$, follows reasonably well the points in the regime III.

where quasi stationary heat diffusion in the ice layer drives the solidification rate and the first crack appears when the thickness of the ice layer is close to the Griffith length. On the contrary, the open diamonds corresponding to the fragmentation time in regime II do not follow the same scaling since the solidification dynamics and temperature fields in the solid are different.

Finally, the transition between regimes II and III is expected when $h_{\text{tot}} \sim L_c$. Then, the elastic energy in the ice block has to be estimated at the time when the solidification ends, namely when $h(t) = h_{\text{tot}}$. In this aim, we need the temperature field. Because the Stefan number is smaller than one, we can consider that the temperature field in the ice layer is in a quasi-stationary regime, obeying to the stationary diffusion equation. Taking a simple horizontal ice layer of heigh $h(t)$ it reads $\partial_{zz} T = 0$, with the boundary conditions $T(0,t) = T_s$ and $T(h(t),t) = T_0$ since the temperature at the solidification front $z = h(t)$ is the freezing temperature. It leads to the linear temperature field:

$$T(z,t) = T_s + \Delta T \frac{z}{h(t)}. \tag{3.23}$$

Integrating the elastic energy density $\mathcal{E}$ on the pancake volume, with this temperature field yields:

$$\frac{3E\alpha^2}{2} \Delta T_{\text{II-III}}^2 \pi R^2 \int_0^{h_{\text{tot}}} (1 - \frac{z}{h_{\text{tot}}})^2 dz = \frac{E\alpha^2}{2} \Delta T_{\text{II-III}}^2 \pi R^2 h_{\text{tot}}.$$

Balancing this energy with the minimal elastic energy needed to fragment ($\frac{3}{2} E\alpha^2 \Delta T_{\text{I-II}}^2 \pi R^2 h_{\text{tot}}$), allows us to obtain the transition temperature $\Delta T_{\text{II-III}}$ separating the two fracture regimes:

$$\Delta T_{\text{II-III}} = \sqrt{3} \Delta T_{\text{I-II}}. \tag{3.24}$$

Taking $\Delta T_{\text{I-II}} \sim 27°$ computed above leads to $\Delta T_{\text{II-III}} \sim 47°$, which is in very good agreement with the experimental transition temperature $T_{\text{II-III}}^{(\text{exp})} = 42°$. Note that this gives a pancake thickness six times larger than the Griffith length at the transition.

With these classical fracture scaling arguments, only based on energy conservation, we can therefore have excellent insights on the cracks appearance and patterns in this system. However, here we merely touched upon the subject and would need to carry on a further studies to deeper understand this very interesting system.

3.9 Conclusions

When a water drop impacts a surface colder than its melting temperature, it freezes as it spreads and a very rich behavior coupling solidification and capillary dynamics builds unexpected small ice structures. As a preamble we developed and validated a unidimensional heat diffusion model that leads to the precise prediction of the solidification front dynamics. Then we have shown that the dynamics could be broken down into four phases:

(1) A rapid spreading of the drop that ends with a thin ice layer on top of which a liquid water layer is pinned. Compared to the isothermal case the solidification reduces the maximal extent of the drop in this spreading regime. Since the ice layer beneath the liquid film grows similarly to the viscous

boundary layer, we showed that this effect could be modeled using an effective viscosity including the freezing rate and the liquid viscosity.

(2) A stillness period during which the water layer is almost at rest and the ice layer grows while the contact angle of the liquid layer relaxes. Using our solidification model we can find precisely the thickness of this first ice layer (h_p).

(3) Then, when the contact angle reaches its depinning threshold, the water film retracts on the ice layer. Here the final shape of the frozen drop is determined by the competition between the dynamics of retraction and freezing. This study also provides an alternative set-up to characterize the equilibrium contact angle of water on ice. Further investigations into these wetting properties might shed more light on the nature of the ice surface [177].

(4) In the end, the frozen water structure shrunk by cooling and pinned on a non shrinking substrate can experience cracks. By increasing the thermal shock, the frozen drop undergoes two regimes: from fragmentation to hierarchical fracture. This original experiment constitutes a model system enabling to easily investigate a broad range of fracture mechanisms and to progress in the understanding of the multi-physic aspects of crack patterns due to thermal shocks.

Being able to predict precisely the ice structure profile has many practical interests since it provides an estimate of the splat thickness formed by the impact. Controlling this thickness is crucial for coating and 3D printing technology [178] and for predicting the further mechanical behaviour of the splat [33, 103]. Moreover it paves the way to progress in the understanding of airplane icing and undoubtedly in the control of anti- or de-icing.

Finally, this work provides a general framework to model and study more complex configuration where capillary hydrodynamics and solidification are coupled, such that the freezing of multiple drop impact, the growth of icicles, the freezing of rivulets, thin films, foams, water-soaked porous...

[177] Nagata et al. (2019), *Accounts of chemical research*, "The Surface of Ice under Equilibrium and Nonequilibrium Conditions".

[178] Lipson et al. (2013), , "Fabricated: The new world of 3D printing".

[33] Ghabache et al. (2016), *Physical Review Letters*, "Frozen impacted drop: From fragmentation to hierarchical crack patterns".
[103] Ruiter et al. (2018), *Nature Physics*, "Self-peeling of impacting droplets".

Bibliography

Here are the references in citation order.

[1] T. Séon, J.-P. Hulin, D. Salin, B. Perrin, and E. Hinch. "Buoyancy driven miscible front dynamics in tilted tubes". *Physics of fluids* **17**,3 (2005), 031702 (see p. 2).

[2] T. Seon, J. Znaien, B. Perrin, E. Hinch, D. Salin, and J. Hulin. "Front dynamics and macroscopic diffusion in buoyant mixing in a tilted tube". *Physics of Fluids* **19**,12 (2007), 125105 (see pp. 2, 3).

[3] T. Séon, J. Znaien, D. Salin, J. Hulin, E. Hinch, and B. Perrin. "Transient buoyancy-driven front dynamics in nearly horizontal tubes". *Physics of Fluids* **19**,12 (2007), 123603 (see p. 2).

[4] T. Séon, J. Hulin, D. Salin, B. Perrin, and E. Hinch. "From turbulent mixing to gravity currents in tilted tubes". *Physics of Fluids* **18**,9 (2006), 091103 (see p. 3).

[5] T. Seon, J.-P. Hulin, D. Salin, B. Perrin, and E. Hinch. "Laser-induced fluorescence measurements of buoyancy driven mixing in tilted tubes". *Physics of Fluids* **18**,4 (2006), 041701 (see p. 3).

[6] T. Seon, J.-P. Hulin, D. Salin, B. Perrin, and E. Hinch. "Buoyant mixing of miscible fluids in tilted tubes". *Physics of fluids* **16**,12 (2004), L103–L106 (see p. 3).

[7] S. Taghavi, T. Seon, D. Martinez, and I. Frigaard. "Buoyancy-dominated displacement flows in near-horizontal channels: the viscous limit". *Journal of fluid mechanics* **639**, (2009), 1–35 (see p. 3).

[8] S. Taghavi, T. Seon, D. Martinez, and I. Frigaard. "Influence of an imposed flow on the stability of a gravity current in a near horizontal duct". *Physics of Fluids* **22**,3 (2010), 031702 (see p. 3).

[9] S. Taghavi, T. Seon, K. Wielage-Burchard, D. Martinez, and I. Frigaard. "Stationary residual layers in buoyant Newtonian displacement flows". *Physics of Fluids* **23**,4 (2011), 044105 (see p. 3).

[10] S. M. Taghavi, K. Alba, T. Séon, K. Wielage-Burchard, D. Martinez, and I. Frigaard. "Miscible displacement flows in near-horizontal ducts at low Atwood number". *Journal of fluid mechanics* **696**, (2012), 175–214 (see p. 3).

[11] T. Séon and A. Antkowiak. "Jets in viscous bubbles". *Phys. Fluids* **23**,9 (2011), 091103 (see p. 4).

[12] T. Séon and A. Antkowiak. "Large bubble rupture sparks fast liquid jet". *Phys. Rev. Lett.* **109**,014501 (2012) (see p. 4).

[13] E. Ghabache, T. Séon, and A. Antkowiak. "Liquid jet eruption from hollow relaxation". *J. Fluid Mech.* **761**, (2014), 206–219 (see p. 4).

[14] F. Veron. "Ocean Spray". *Annual Review of Fluid Mechanics* **47**,1 (2015), 507–538 (see pp. 6, 21, 41).

[15] G. B. Deane and M. D. Stokes. "Scale dependence of bubble creation mechanisms in breaking waves". *Nature* **418**,6900 (2002), 839–844 (see pp. 6, 8, 21).

[16] L. Deike, W. K. Melville, and S. Popinet. "Air entrainment and bubble statistics in breaking waves". *Journal of Fluid Mechanics* **801**, (2016), 91–129 (see pp. 6, 8, 21).

[17] E. Ghabache, A. Antkowiak, C. Josserand, and T. Séon. "On the physics of fizziness: How bubble bursting controls droplets ejection". *Physics of Fluids* **26**,12 (2014), (see pp. 6, 22, 23, 29).

[18] L. Deike, E. Ghabache, G. Liger-Belair, A. K. Das, S. Zaleski, S. Popinet, and T. Séon. "Dynamics of jets produced by bursting bubbles". *Physical Review Fluids* **3**,1 (2018), 013603 (see pp. 7, 28–30).

[19] E. Ghabache and T. Séon. "Size of the top jet drop produced by bubble bursting". *Phys. Rev. Fluids* **1**,051901 (2016) (see pp. 8, 31, 36).

[20] A. Berny, L. Deike, T. Séon, and S. Popinet. "Role of all jet drops in mass transfer from bursting bubbles". *Physical Review Fluids* **5**,3 (2020), 033605 (see pp. 8, 9, 22, 29, 36, 38, 41).

[21] G. Liger-Belair. "How many bubbles in your glass of bubbly?" *The Journal of Physical Chemistry B* **118**,11 (2014), 3156–3163 (see p. 8).

[22] E. Ghabache, G. Liger-Belair, A. Antkowiak, and T. Séon. "Evaporation of droplets in a Champagne wine aerosol". *Scientific Reports* **6**, (2016), 25148 (see pp. 9, 38, 39).

[23] G. Liger-Belair, T. Séon, and A. Antkowiak. "Collection of collapsing bubble driven phenomena found in champagne glasses". *Bubble Science, Engineering & Technology* **4**,1 (2012), 21–34 (see p. 9).

[24] G. Liger-Belair, C. Cilindre, G. Polidori, H. Pron, T. Séon, E. Ghabache, A. Antkowiak, and F. H. Jamesse Philippe. "La dégustation du champagne : Quelques éléments de réflexion sur l'impact de la forme du verre et de la taille des bulles". *Revue des œnologues et des techniques vitivinicoles et œnologicques : magazine trimestriel d'information professionnelle* **40**,149 (2013), 43–46 (see p. 9).

[25] T. Séon and G. Liger-Belair. "Effervescence in champagne and sparkling wines: From bubble bursting to droplet evaporation". *The European Physical Journal Special Topics* **226**,1 (2017), 117–156 (see p. 9).

[26] C. Josserand and S. Thoroddsen. "Drop impact on a solid surface". *Annual Review of Fluid Mechanics* **48**, (2016), 365–391 (see pp. 10, 43, 44, 50).

[27] G.-J. Michon, C. Josserand, and T. Séon. "Jet dynamics post drop impact on a deep pool". *Physical Review Fluids* **2**,2 (2017), 023601 (see p. 10).

[28] F. Marcotte, G.-J. Michon, T. Séon, and C. Josserand. "Ejecta, corolla, and splashes from drop impacts on viscous fluids". *Physical review letters* **122**,1 (2019), 014501 (see pp. 10, 11).

[29] S. Beltaos. *River ice formation.* Committee on river ice processes and the environment, Canadian geophysical . . ., 2013 (see p. 11).

[30] V. Thiévenaz, T. Séon, and C. Josserand. "Solidification dynamics of an impacted drop". *J. Fluid Mech.* **874**, (2019), 756–773 (see pp. 12, 46, 51, 55, 61).

[31] V. Thiévenaz, T. Séon, and C. Josserand. "Freezing-damped impact of a water drop". *Subm. to Europhys. Lett.* (2020) (see pp. 13, 50, 53).

[32] V. Thiévenaz, C. Josserand, and T. Séon. "Retraction and freezing of a water film on ice". *Phys. Rev. Fluids* **5**, (2020), 041601 (see pp. 13, 44, 51, 58).

[33] E. Ghabache, C. Josserand, and T. Séon. "Frozen impacted drop: From fragmentation to hierarchical crack patterns". *Physical Review Letters* **117**,7 (2016), 074501 (see pp. 13, 43, 67).

[34] A. Monier, A. Huerre, C. Josserand, and T. Séon. "Freezing a rivulet". *Physical Review Fluids* **5**,6 (2020), 062301 (see p. 14).

[35] A. Huerre, A. Monier, T. Séon, and C. Josserand. "Solidification of a rivulet: shape and temperature fields". *Subm. to J. Fluid Mech.* (2020) (see p. 14).

[36] H. Lhuissier and E. Villermaux. "Bursting bubble aerosols". *Journal of Fluid Mechanics* **696**, (2012), 5–44 (see pp. 15, 21, 22).

[37] A. Persoiu and S.-E. Lauritzen. *Ice caves.* Elsevier, 2018 (see p. 18).

[38] E. R. Lewis and S. E. Schwartz. *Sea Salt Aerosol Production. Mechanisms, Methods, Measurements, and Models.* Geophysical Monograph 152. Washington, DC, American Geophysical Union, 2004 (see p. 21).

[39] G. de Leeuw, E. L. Andreas, M. D. Anguelova, C. W. Fairall, E. R. Lewis, C. O'Dowd, M. Schulz, and S. E. Schwartz. "Production flux of sea spray aerosol". *Rev. Geophys.* **49**,2 (May 2011) (see p. 21).

[40] E. L. Andreas, J. B. Edson, E. C. Monahan, M. P. Rouault, and S. D. Smith. "The spray contribution to net evaporation from the sea: A review of recent progress". *Boundary-Layer Meteorol.* **72**,3 (1995) (see pp. 21, 41).

[41] E. L. Andreas and K. A. Emanuel. "Effects of sea spray on tropical cyclone intensity". *Journal of the atmospheric sciences* **58**,24 (2001), 3741–3751 (see p. 21).

[42] A. Malloch. "Salt-spray deposition on the maritime cliffs of the Lizard Peninsula". *The Journal of Ecology* (1972), 103–112 (see p. 21).

[43] E. Schindelholz, B. Risteen, and R. Kelly. "Effect of relative humidity on corrosion of steel under sea salt aerosol proxies: I. NaCl". *Journal of The Electrochemical Society* **161**,10 (2014), C450 (see p. 21).

[44] F. Veron, C. Hopkins, E. Harrison, and J. Mueller. "Sea spray spume droplet production in high wind speeds". *Geophysical Research Letters* **39**,16 (2012) (see p. 21).

[45] D. C. Blanchard. "The electrification of the atmosphere by particles from bubbles in the sea". *Progress In Oceanography* **1**, (1963), 73–112, IN7, 113–202 (see pp. 21, 24, 25).

[46] D. E. Spiel. "On the births of jet drops from bubbles bursting on water surfaces". *J. Geophys. Res.* **100**,C3 (1995), 4995–5006 (see pp. 21, 24, 25).

[47] L. Deike, L. Lenain, and W. K. Melville. "Air entrainment by breaking waves". *Geophysical Research Letters* **44**,8 (2017), 3779–3787 (see pp. 21, 22).

[48] E. Ghabache. 'Surface libre hors équilibre : de l'effondrement de cavité aux jets étirés'. PhD thesis. UPMC, 2015 (see pp. 21, 22).

[49] F. J. Resch, J. S. Darrozes, and G. M. Afeti. "Marine Liquid Aerosol Production From Bursting of Air Bubbles". *J. Geophys. Res.* **91(C1)**, (1986), 1019–1029 (see p. 21).

[50] A. H. Woodcock, C. F. Kientzler, A. B. Arons, and D. C. Blanchard. "Giant Condensation Nuclei from Bursting Bubbles". *Nature* **172**,4390 (Dec. 1953), 1144–1145 (see p. 21).

[51] S. Hayami and Y. Toba. "Drop Production by Bursting of Air Bubbles on the Sea Surface (1) Experiments at Still Sea Water Surface". *Journal of the Oceanographical Society of Japan* **14**,4 (Dec. 1958), 145–150 (see p. 21).

[52] J. Wu. "Spray in the atmospheric surface layer: Laboratory study". *Journal of Geophysical Research* **78**,3 (1973), 511–519 (see p. 21).

[53] J. M. Boulton-Stone and J. R. Blake. "Gas bubbles bursting at a free surface". *Journal of Fluid Mechanics* **254**, (1993), 437–466 (see pp. 21, 24, 25).

[54] L. Duchemin, S. Popinet, C. Josserand, and S. Zaleski. "Jet formation in bubbles bursting at a free surface". *Phys. Fluids* **14**,9 (2002), 3000–3008 (see pp. 21, 23, 24, 26–28).

[55] Y. Toba. "Drop Production by Bursting of Air Bubbles on the Sea Surface (II) Theoretical Study on the Shape of Floating Bubbles". *Journal of the Oceanographical Society of Japan* **15**,3 (1959), 121–130 (see p. 22).

[56] F. MacIntyre. "Flow patterns in breaking bubbles". *Journal of Geophysical Research* **77**,27 (1972), 5211–5228 (see p. 23).

[57] B. W. Zeff, B. Kleber, J. Fineberg, and D. P. Lathrop. "Singularity dynamics in curvature collapse and jet eruption on a fluid surface". *Nature* **403**,6768 (Jan. 2000), 401–404 (see p. 26).

[58] D. Bartolo, C. Josserand, and D. Bonn. "Singular Jets and Bubbles in Drop Impact". *Phys. Rev. Lett.* **96**,12 (2006), 124501–4 (see p. 26).

[59] J. B. Keller and M. J. Miksis. "Surface Tension Driven Flows". *SIAM Journal on Applied Mathematics* **43**,2 (1983), 268–277 (see p. 26).

[60] A. M. Gañán-Calvo. "Revision of bubble bursting: universal scaling laws of top jet drop size and speed". *Physical review letters* **119**,20 (2017), 204502 (see pp. 29–31, 36, 37, 42).

[61] A. M. Gañán-Calvo. "Scaling laws of top jet drop size and speed from bubble bursting including gravity and inviscid limit". *Phys. Rev. Fluids* **3**, (Sept. 2018), 091601 (see pp. 30, 42).

[62] D. E. Spiel. "The number and size of jet drops produced by air bubbles bursting on a fresh water surface". *J. Geophys. Res.* **99**,C5 (1994), 10289–10296 (see pp. 31, 32).

[63] J. B. Keller, A. King, and L. Ting. "Blob formation". *Physics of Fluids* **7**,1 (1995), 226–228 (see p. 31).

[64] H. A. Stone and L. Leal. "Relaxation and breakup of an initially extended drop in an otherwise quiescent fluid". *Journal of Fluid Mechanics* **198**, (1989), 399–427 (see p. 31).

[65] A. A. Castrejón-Pita, J. Castrejon-Pita, and I. Hutchings. "Breakup of liquid filaments". *Physical review letters* **108**,7 (2012), 074506 (see p. 31).

[66] M. Singh, H. M. Haverinen, P. Dhagat, and G. E. Jabbour. "Inkjet printing—process and its applications". *Advanced materials* **22**,6 (2010), 673–685 (see p. 32).

[67] P. L. L. Walls, L. Henaux, and J. C. Bird. "Jet drops from bursting bubbles: How gravity and viscosity couple to inhibit droplet production". *Phys. Rev. E* **92**, (Aug. 2015), 021002 (see p. 32).

[68] J. M. Gordillo and S. Gekle. "Generation and breakup of Worthington jets after cavity collapse. Part 2. Tip breakup of stretched jets". *J. Fluid Mech.* **663**, (2010), 331–346 (see p. 32).

[69] S. R. Massel. *Ocean Waves Breaking and Marine Aerosol Fluxes.* Springer, 2007 (see p. 33).

[70] C. F. Brasz, C. T. Bartlett, P. L. Walls, E. G. Flynn, Y. E. Yu, and J. C. Bird. "Minimum size for the top jet drop from a bursting bubble". *Physical Review Fluids* **3**,7 (2018), 074001 (see pp. 36, 37).

[71] R. Clift, J. R. Grace, and M. E. Weber. *Bubbles, drops, and particles.* Ed. by D. Publications. Dover books on engineering, 2005 (see p. 38).

[72] L. Schiller and A. Naumann. "A drag coefficient correlation". *Vdi Zeitung* **77**,318 (1935), 51 (see p. 38).

[73] A. Frohn and N. Roth. *Dynamics of droplets.* Springer Science & Business Media, 2000 (see p. 38).

[74] W. A. Sirignano. *Fluid dynamics and transport of droplets and sprays.* Cambridge University Press, 1999 (see p. 38).

[75] A.-M. Cazabat and G. Guéna. "Evaporation of macroscopic sessile droplets". *Soft Matter* **6**,12 (2010), 2591–2612 (see p. 38).

[76] I. Langmuir. "The evaporation of small spheres". *Physical review* **12**,5 (1918), 368 (see p. 38).

[77] N. A. Fuchs. *Evaporation and droplet growth in gaseous media.* Ed. by P. Press. Elsevier, 1959 (see p. 38).

[78] W. Ranz and W. Marshall. "Evaporation from drops". *Chem. Eng. Prog* **48**,3 (1952), 141–146 (see p. 38).

[79] E. Pohlhausen. "Der Wärmeaustausch zwischen festen Körpern und Flüssigkeiten mit kleiner Reibung und kleiner Wärmeleitung". *ZAMM-Journal of Applied Mathematics and Mechanics/Zeitschrift für Angewandte Mathematik und Mechanik* **1**,2 (1921), 115–121 (see p. 39).

[80] J. Gordillo and J. Rodriguez-Rodriguez. "Capillary waves control the ejection of bubble bursting jets". *Journal of Fluid Mechanics* **867**, (2019), 556–571 (see p. 42).

[81] F. J. Blanco-Rodriguez and J. Gordillo. "On the sea spray aerosol originated from bubble bursting jets". *Journal of Fluid Mechanics* **886**, (2020) (see p. 42).

[82] A. S.-H. Chen and S. W. Morris. "Experiments on the morphology of icicles". *Physical Review E* **83**,2 (2011), 026307 (see p. 43).

[83] M. Moore, M. Mughal, and D. Papageorgiou. "Ice formation within a thin film flowing over a flat plate". *Journal of Fluid Mechanics* **817**, (2017), 455–489 (see p. 43).

[84] S. F. Ahmadi, S. Nath, C. M. Kingett, P. Yue, and J. B. Boreyko. "How soap bubbles freeze". *Nature communications* **10**,1 (2019), 1–10 (see p. 43).

[85] A. M. Worthington. "On the Forms Assumed by Drops of Liquids Falling Vertically on a Horizontal Plate". *Proceedings of the Royal Society of London* **25**, (1876 - 1877), 261–272 (see p. 43).

[86] G. Lamé and B. Clapeyron. 'Mémoire sur la solidification par refroidissement d'un globe liquide'. *Annales Chimie Physique.* Vol. 47. 1831, 250–256 (see pp. 43, 46).

[87] S. Wildeman, S. Sterl, C. Sun, and D. Lohse. "Fast Dynamics of Water Droplets Freezing from the Outside In". *Physical Review Letters* **118**,8 (2017), 084101 (see p. 43).

[88] S. D. Aziz and S. Chandra. "Impact, recoil and splashing of molten metal droplets". *Int. J. Heat Mass Transf.* **43**,16 (2000), 2841–2857 (see p. 43).

[89] I. V. Roisman. "Fast forced liquid film spreading on a substrate: flow, heat transfer and phase transition". *Journal of Fluid Mechanics* **656**, (2010), 189–204 (see p. 43).

[90] T. Cebeci and F. Kafyeke. "Aircraft icing". *Annual review of fluid mechanics* **35**,1 (2003), 11–21 (see p. 43).

[91] J. Laforte, M. Allaire, and J. Laflamme. "State-of-the-art on power line de-icing". *Atmospheric Research* **46**,1-2 (1998), 143–158 (see p. 43).

[92] Y. Liu, W. Chen, Y. Peng, and H. Hu. "An experimental study on the dynamic ice accretion processes on bridge cables with different surface modifications". *Journal of Wind Engineering and Industrial Aerodynamics* **190**, (2019), 218–229 (see p. 43).

[93] Z. Wang. "Recent progress on ultrasonic de-icing technique used for wind power generation, high-voltage transmission line and aircraft". *Energy and Buildings* **140**, (2017), 42–49 (see p. 43).

[94] K. F. Jones. *Ice accretion in freezing rain.* Tech. rep. COLD REGIONS RESEARCH and ENGINEERING LAB HANOVER NH, 1996 (see p. 43).

[95] M. J. Kreder, J. Alvarenga, P. Kim, and J. Aizenberg. "Design of anti-icing surfaces: smooth, textured or slippery?" *Nature Reviews Materials* **1**,1 (2016), 15003 (see p. 43).

[96] M. Schremb, I. V. Roisman, and C. Tropea. "Normal impact of supercooled water drops onto a smooth ice surface: experiments and modelling". *Journal of Fluid Mechanics* **835**, (2018), 1087–1107 (see p. 43).

[97] R. Dhiman, A. G. McDonald, and S. Chandra. "Predicting splat morphology in a thermal spray process". *Surface and Coatings Technology* **201**,18 (2007), 7789–7801 (see p. 43).

[98] S. Chandra and P. Fauchais. "Formation of solid splats during thermal spray deposition". *Journal of Thermal Spray Technology* **18**,2 (2009), 148–180 (see p. 43).

[99] J. Madejski. "Solidification of droplets on a cold surface". *Int. J. Heat Mass Transf.* **19**,9 (1976), 1009–1013 (see pp. 43, 50, 52).

[100] R. Bhola and S. Chandra. "Parameters controlling solidification of molten wax droplets falling on a solid surface". *Journal of materials science* **34**,19 (1999), 4883–4894 (see p. 43).

[101] M. Pasandideh-Fard, V. Pershin, S. Chandra, and J. Mostaghimi. "Splat shapes in a thermal spray coating process: simulations and experiments". *Journal of Thermal Spray Technology* **11**,2 (2002), 206–217 (see p. 43).

[102] P. Fauchais, A. Vardelle, M. Vardelle, and M. Fukumoto. "Knowledge concerning splat formation: an invited review". *Journal of Thermal Spray Technology* **13**,3 (2004), 337–360 (see p. 43).

[103] J. de Ruiter, D. Soto, and K. K. Varanasi. "Self-peeling of impacting droplets". *Nature Physics* **14**,1 (2018), 35 (see pp. 43, 44, 67).

[104] W. Schultz, M. Worster, and D. Anderson. 'Solidifying sessile water droplets'. *Interactive dynamics of convection and solidification.* Springer, 2001, 209–226 (see p. 43).

[105] A. G. Marin, O. R. Enriquez, P. Brunet, P. Colinet, and J. H. Snoeijer. "Universality of tip singularity formation in freezing water drops". *Physical review letters* **113**,5 (2014), 054301 (see p. 43).

[106] D. Anderson, M. G. Worster, and S. Davis. "The case for a dynamic contact angle in containerless solidification". *Journal of crystal growth* **163**,3 (1996), 329–338 (see pp. 43, 46).

[107] R. De Ruiter, P. Colinet, P. Brunet, J. H. Snoeijer, and H. Gelderblom. "Contact line arrest in solidifying spreading drops". *Phys. Rev. Fluids* **2**,4 (2017), 043602 (see pp. 43, 50).

[108] F. Tavakoli, S. H. Davis, and H. P. Kavehpour. "Spreading and arrest of a molten liquid on cold substrates". *Langmuir* **30**,34 (2014), 10151–10155 (see pp. 43, 50).

[109] S. Schiaffino and A. A. Sonin. "Motion and arrest of a molten contact line on a cold surface: an experimental study". *Phys. Fluids* **9**,8 (1997), 2217–2226 (see pp. 43, 46, 50).

[110] T. Bennett and D. Poulikakos. "Heat transfer aspects of splat-quench solidification: modelling and experiment". *Journal of Materials Science* **29**,8 (1994), 2025–2039 (see p. 44).

[111] D. R. Lide. *CRC handbook of chemistry and physics*. CRC Press, Boca Raton, FL, 2005 (see pp. 44, 55, 61).

[112] L. Rubinstein. *The Stefan Problem*. Vol. 27. Translations of Mathematical Monographs. American Mathematical Soc., 1971 (see pp. 45, 47).

[113] S. Schiaffino and A. Sonin. "Molten droplet deposition and solidification at low Weber numbers". *Phys. Fluids* **9**, (1997), 3172 (see p. 46).

[114] C. A. Knight. "The contact angle of water on ice". *Journal of Colloid and Interface Science* **25**,2 (1966), 280–284 (see pp. 46, 61).

[115] L. Makkonen. "Surface melting of ice". *The Journal of Physical Chemistry B* **101**,32 (1997), 6196–6200 (see pp. 46, 61).

[116] C. Van Oss, R. Giese, R. Wentzek, J. Norris, and E. Chuvilin. "Surface tension parameters of ice obtained from contact angle data and from positive and negative particle adhesion to advancing freezing fronts". *Journal of adhesion science and technology* **6**,4 (1992), 503–516 (see pp. 46, 61).

[117] J. Stefan. "Über die Theorie der Eisbildung, insbesondere über die Eisbildung im Polarmeere". *Ann. Physik Chemie* **42**, (1891), 269–286 (see p. 46).

[118] M. Brillouin. ‘Sur quelques problèmes non résolus de la Physique Mathématique classique Propagation de la fusion’. *Annales de l’institut Henri Poincaré*. Vol. 1. 3. 1930, 285–308 (see p. 46).

[119] J. S. Langer. "Instabilities and pattern formation in crystal growth". *Reviews of Modern Physics* **52**,1 (1980), 1 (see p. 46).

[120] M. G. Worster. "Solidifcation of Fluids". *Perspectives in fluid dynamics: a collective introduction to current research* (2000) (see p. 46).

[121] J. A. Neufeld, R. E. Goldstein, and M. G. Worster. "On the mechanisms of icicle evolution". *Journal of Fluid Mechanics* **647**, (2010), 287–308 (see p. 46).

[122] R. Griffiths. "The dynamics of lava flows". *Annual Review of Fluid Mechanics* **32**,1 (2000), 477–518 (see p. 47).

[123] H. E. Huppert. "Phase changes following the initiation of a hot turbulent flow over a cold solid surface". *Journal of Fluid Mechanics* **198**, (1989), 293–319 (see p. 47).

[124] H. E. Huppert. "The intrusion of fluid mechanics into geology". *Journal of Fluid Mechanics* **173**, (1986), 557–594 (see p. 47).

[125] R. Viskanta. "Heat transfer during melting and solidification of metals". *Journal of Heat Transfer* **110**,4b (1988), 1205–1219 (see p. 47).

[126] T. Nishinaga. *Handbook of crystal growth: fundamentals*. Elsevier, 2014 (see p. 47).

[127] M. v. Allmen and A. Blatter. *Laser-beam interactions with materials: physical principles and applications*. Vol. 2. Springer Science & Business Media, 2013 (see p. 47).

[128] F. Font, S. Afkhami, and L. Kondic. "Substrate melting during laser heating of nanoscale metal films". *Int. J. Heat Mass Transf.* **113**, (2017), 237–245 (see p. 47).

[129] S. Gupta. *The Classical Stefan Problem - Basic Concepts, Modelling and Analysis*. Elsevier Science B.V, Amsterdam, 2003 (see p. 47).

[130] C. Clanet, C. Béguin, D. Richard, and D. Quéré. "Maximal deformation of an impacting drop". *J. Fluid Mech* **517**, (2004), 199–208 (see pp. 50, 52).

[131] N. Laan, K. G. de Bruin, D. Bartolo, C. Josserand, and D. Bonn. "Maximum Diameter of Impacting Liquid Droplets". *Physical Review Applied* **2**,4 (2014), 044018 (see pp. 50, 52).

[132] M. V. Gielen, R. de Ruiter, R. B. Koldeweij, D. Lohse, J. H. Snoeijer, and H. Gelderblom. "Solidification of liquid metal drops during impact". *J. Fluid Mech.* **883**, (2020) (see p. 50).

[133] J. Madejski. "Droplets on impact with a solid surface". *International Journal of Heat and Mass Transfer* **26**,7 (1983), 1095–1098 (see p. 52).

[134] A. I. Fedorchenko, A.-B. Wang, and Y.-H. Wang. "Effect of capillary and viscous forces on spreading of a liquid drop impinging on a solid surface". *Physics of Fluids* **17**,9 (2005), 093104 (see p. 52).

[135] J. Eggers, M. A. Fontelos, C. Josserand, and S. Zaleski. "Drop dynamics after impact on a solid wall: theory and simulations". *Physics of Fluids* **22**,6 (2010), 062101 (see p. 52).

[136] J. Lee, N. Laan, K. De Bruin, G. Skantzaris, N. Shahidzadeh, D. Derome, J. Carmeliet, and D. Bonn. "Universal rescaling of drop impact on smooth and rough surfaces". *Journal of Fluid Mechanics* **786**, (2016) (see pp. 52, 53).

[137] G. Lagubeau, M. A. Fontelos, C. Josserand, A. Maurel, V. Pagneux, and P. Petitjeans. "Spreading dynamics of drop impacts". *Journal of Fluid Mechanics* **713**, (2012), 50 (see p. 52).

[138] J. Hallett. "The temperature dependence of the viscosity of supercooled water". *Proceedings of the Physical Society* **82**,6 (1963), 1046 (see p. 55).

[139] M. Rivetti, T. Salez, M. Benzaquen, E. Raphaël, and O. Bäumchen. "Universal contact-line dynamics at the nanoscale". *Soft Matter* **11**,48 (2015), 9247–9253 (see pp. 55, 56, 59).

[140] C. A. Knight. "Experiments on the contact angle of water on ice". *Philosophical magazine* **23**,181 (1971), 153–165 (see pp. 58, 61).

[141] V. F. Petrenko and R. W. Whitworth. *Physics of ice.* Clarendon Press, 1999 (see pp. 58, 61, 64).

[142] J. W. Frenken and J. Van der Veen. "Observation of surface melting". *Physical review letters* **54**,2 (1985), 134 (see p. 58).

[143] A. Lied, H. Dosch, and J. Bilgram. "Surface Melting of lce lh Single Crystals Revealed by Glancing Angle X-Ray Scattering". *Phys. Rev. Lett.* **72**,22 (1994), 3554 (see p. 58).

[144] Y. Li and G. A. Somorjai. "Surface premelting of ice". *The Journal of Physical Chemistry C* **111**,27 (2007), 9631–9637 (see p. 58).

[145] G. Sazaki, S. Zepeda, S. Nakatsubo, M. Yokomine, and Y. Furukawa. "Quasi-liquid layers on ice crystal surfaces are made up of two different phases". *Proceedings of the National Academy of Sciences* **109**,4 (2012), 1052–1055 (see p. 58).

[146] F.E.C. Culick. "Comments on a ruptured soap film". *J. Appl. Phys.* **31**, (1960), 1128 (see p. 58).

[147] A. M. Edwards, R. Ledesma-Aguilar, M. I. Newton, C. V. Brown, and G. McHale. "Not spreading in reverse: The dewetting of a liquid film into a single drop". *Science Advances* **2**,9 (2016), e1600183 (see p. 59).

[148] D. Bonn, J. Eggers, J. Indekeu, J. Meunier, and E. Rolley. "Wetting and spreading". *Rev. Mod. Phys.* **81**, (2009), 739 (see p. 61).

[149] W. Ketcham and P. Hobbs. "An experimental determination of the surface energies of ice". *Philosophical Magazine* **19**,162 (1969), 1161–1173 (see p. 61).

[150] J. Drelich, E. Chibowski, D. D. Meng, and K. Terpilowski. "Hydrophilic and superhydrophilic surfaces and materials". *Soft Matter* **7**,21 (2011), 9804–9828 (see p. 61).

[151] C. Merrett. *The Art of Glass.* London:Octavian Pulleyn, 1662 (see p. 61).

[152] S. Chandrasekar and M. Chaudhri. "The explosive disintegration of Prince Rupert's drops". *Philos. Mag. Part B* **70**, (1994), 1195–1218 (see p. 61).

[153] P. Marmottant and E. Villermaux. "Fragmentation of stretched liquid ligaments". *Phys. Fluids* **16**,8 (2004), 2732–2741 (see p. 62).

[154] E. Villermaux. "Fragmentation". *Annu. Rev. Fluid Mech.* **39**,1 (2007), 419–446 (see p. 62).

[155] B. Audoly and S. Neukirch. "Fragmentation of Rods by Cascading Cracks: Why Spaghetti Does Not Break in Half". *Phys. Rev. Lett.* **95**,9 (2005) (see p. 62).

[156] S. Moulinet and M. Adda-Bedia. "Popping Balloons: A Case Study of Dynamical Fragmentation". *Phys. Rev. Lett.* **115**, (Oct. 2015), 184301 (see p. 62).

[157] N. Vandenberghe and E. Villermaux. "Geometry and fragmentation of soft brittle impacted bodies". *Soft Matter* **9**,34 (2013), 8162–8176 (see p. 62).

[158] F. Wittel, F. Kun, H. Herrmann, and B. Kröplin. "Fragmentation of shells". *Phys. Rev. Lett.* **93**,3 (2004), 035504 (see p. 62).

[159] P. Kokelaar. "Magma-water interactions in subaqueous and emergent basaltic". *Bulletin of Volcanology* **48**,5 (1986), 275–289 (see p. 62).

[160] L. Goehring, L. Mahadevan, and S. W. Morris. "Nonequilibrium scale selection mechanism for columnar jointing". *Proc. Natl. Acad. Sci.* **106**,2 (2009), 387–392 (see p. 62).

[161] A. Sagy, J. Fineberg, and Z. Reches. "Shatter cones: Branched, rapid fractures formed by shock impact". *J. Geophys. Res.: Solid Earth* **109**,B10 (2004) (see p. 62).

[162] S. Bohn, L. Pauchard, and Y. Couder. "Hierarchical crack pattern as formed by successive domain divisions. I. Temporal and geometrical hierarchy". *Phys. Rev. E* **71**,4 (2005), 046214 (see pp. 62, 64).

[163] K. A. Shorlin, J. R. de Bruyn, M. Graham, and S. W. Morris. "Development and geometry of isotropic and directional shrinkage-crack patterns". *Phys. Rev. E* **61**,6 (2000), 6950 (see p. 62).

[164] E. Kindle. "Some factors affecting the development of mud-cracks". *The Journal of Geology* **25**,2 (1917), 135–144 (see p. 62).

[165] G. Korvin. "Fractured but not fractal: Fragmentation of the gulf of suez basement". *Pure Appl. Geophys.* **131**,1-2 (1989), 289–305 (see p. 62).

[166] A. Groisman and E. Kaplan. "An experimental study of cracking induced by desiccation". *Europhys. Lett.* **25**,6 (1994), 415 (see p. 62).

[167] L. Pauchard, F. Parisse, and C. Allain. "Influence of salt content on crack patterns formed through colloidal suspension desiccation". *Phys. Rev. E* **59**,3 (1999), 3737 (see p. 62).

[168] P. Xu, A. Mujumdar, and B. Yu. "Drying-induced cracks in thin film fabricated from colloidal dispersions". *Drying Technology* **27**,5 (2009), 636–652 (see p. 62).

[169] L. Pauchard, V. Lazarus, B. Abou, K. Sekimoto, G. Aitken, and C. Lahanier. "Craquelures dans les couches picturales des peintures d'art". *Reflets de la Physique* 3 (2007), 5–9 (see p. 62).

[170] W. Korneta, S. Mendiratta, and J. Menteiro. "Topological and geometrical properties of crack patterns produced by the thermal shock in ceramics". *Physical Review E* **57**,3 (1998), 3142 (see p. 63).

[171] S. Lahlil, W. Li, and J. M. Xu. "Crack patterns morphology of ancient Chinese wares". *The Old Potter's Almanack* **18**,1 (2013), 1–9 (see p. 63).

[172] L. Freund. *Dynamic Fracture Mechanics.* Cambridge University Press, 1990 (see p. 63).

[173] M. Adda-Bedia, M. B. Amar, and Y. Pomeau. "Morphological instabilities of dynamic fractures in brittle solids". *Physical Review E* **54**,5 (1996), 5774 (see p. 64).

[174] B. Bourdin, J.-J. Marigo, C. Maurini, and P. Sicsic. "Morphogenesis and propagation of complex cracks induced by thermal shocks". *Physical review letters* **112**,1 (2014), 014301 (see p. 64).

[175] E. M. Schulson and P. Duval. *Creep and fracture of ice.* Vol. 432. Cambridge University Press Cambridge, 2009 (see p. 64).

[176] G. Gauthier, V. Lazarus, and L. Pauchard. "Shrinkage star-shaped cracks: Explaining the transition from 90 degrees to 120 degrees". *Europhysics Letters* **89**,2 (2010), 26002 (see p. 64).

[177] Y. Nagata, T. Hama, E. H. Backus, M. Mezger, D. Bonn, M. Bonn, and G. Sazaki. "The Surface of Ice under Equilibrium and Nonequilibrium Conditions". *Accounts of chemical research* (2019) (see p. 67).

[178] H. Lipson and M. Kurman. *Fabricated: The new world of 3D printing*. John Wiley & Sons, 2013 (see p. 67).